



Design Tools Applied to a Trochoidal Gear Pump

Mercedes García Vílchez

A thesis submitted to the Universitat Politècnica de Catalunya
for the degree of Doctor of Philosophy in the
Escola Tècnica Superior d'Enginyeries Industrial i Aeronàutica de Terrassa
Fluid Mechanics Department

June 2014

Universitat Politècnica de Catalunya (UPC)
Laboratorio de Sistemas Oleohidráulicos y Neumáticos (LABSON)

Design Tools Applied to a Trochoidal Gear Pump

Author

Mercedes García Vílchez

Mechanical Engineer

Director

Esteban Codina Macià

Doctor Mechanical Engineer

Codirector

Pedro Javier Gámez Montero

Doctor Mechanical Engineer

Thanks & Acknowledgements

I take this opportunity to express my profound gratitude and deep regards to my thesis supervisors, Dr. Esteban Codina Macià and Dr. Pedro Javier Gámez Montero for their exemplary direction and constant encouragement throughout the course of this thesis. Their guidance has helped me during the research and writing of this thesis.

I would like to gratefully thank:

Lecturer Antón Vernet from the Escola Tècnica d'Enginyeria Química of the Rovira I Virgili University, and Dr. Nihal Erturk Duzgun, for providing the particles used in the PIV experimental tests and for all their help.

The technicians of the laboratory of the ETSEIAT Fluid Mechanics Department Jaume Bonastre and Justo Zoyo for their help in the design and assembly of the experimental test bench.

The lab technician Carlos Río Cano and the professor Dr. Munir Khamashta Shahin, from the Department of Mechanical Engineering, for their help in the making of the experimental pump.

Lecturers Dr. Robert Castilla López and Dr. Gustavo Raush Alviach from the ETSEIAT Fluid Mechanics Department for their support and help during all these years.

The companies Aleaciones de Metales Sinterizados, S.A. (AMES) and Pedro Roquet, S.A, without which the experimental work would not have been possible.

Lecturer Gerber van der Graaf, the author of the GPIV software, which has allowed the processing of the experimental PIV images.

All the members of LABSON for their support and help. I would also like to thank all the members of the Fluid Mechanics Department of the Terrassa Campus.

On the personal side, I want to give very special thanks to my parents, for the constant devotion they have always put into my education. To my sisters and brother, I want to recognize their valuable advices, not only for this thesis but also in the rest of aspects of my life. Without all of them this work would not have been possible.

I also place on record, my sense of gratitude to one and all who, directly or indirectly, have lent their helping hand in this venture.

Abstract

Trochoidal gear pumps, as currently designed, produce significant flow pulsations that result in pressure pulsations. These pulsations interact with the system where they are connected, shortening the life of both the pump and circuit components. A set of design tools applied to trochoideal gear pumps is presented, involving the analytical, simulation and experimental point of study.

From the analytical side, two new modules of GeroLAB Package are created, *Minimum Clearance Module* and *Effective Port Areas*. Also, a dynamical simulation through BondGraph is conducted, studying the influence of the port areas geometry.

Regarding the numerical simulation, a three-dimensional with deforming mesh Computational Fluid Dynamics model is presented. The model includes the effects of the manufacturing tolerance and the leakage inside the pump. Also, the influence of simulating the contact points is studied. A new boundary condition is created for the simulation of the solid contact in the interteeth radial clearance.

The experimental study of the pump is carried out by means of Time-Resolved Particle Image Velocimetry. This technique is developed in order to adapt it to the gerotor pump, and measurements are captures in the outlet pipe and in the chambers between trochoidal profiles. The experimental results are qualitatively evaluated thanks to the analytical and simulation tools.

Contents

List of Figures	v
List of Tables	ix
Nomenclature	xi
1 Introduction	1
1.1 Preamble	1
1.2 Gerotor pump	1
1.3 Thesis objectives and scope.....	3
1.4 Organization of the Thesis.....	5
1.5 State of the Art.....	5
2 Analytical Approach	15
2.1 Introduction to the Analytical Approach	15
2.2 GeroLAB Package	15
2.3 Minimum Clearance Module	16
2.4 Effective Port Areas Module	18
2.4.1 Specific Zones and Fluid Circulation Boundaries	18
2.4.2 Analytical Expressions	20
2.4.3 Studied port area geometries.....	23
2.5 Dynamical Simulation	27
2.6 Results of the Dynamical Simulation	30
2.7 Conclusions of the Analytical Approach.....	34
3 Numerical Simulation	37
3.1 Introduction to the Numerical Simulation	37
3.2 Numerical schemes	38

3.3	Turbulence modelling	40
3.4	Convergence criteria	42
3.5	Simulation of the tooth contact in the interteeth clearance.....	43
3.6	Mesh properties.....	47
3.6.1	Mesh zones	47
3.6.2	Mesh deformation algorithm	49
3.6.3	Mesh quality analysis and grid independence study.....	52
3.7	Influence of simulating the contact points.....	53
3.8	Numerical Simulation conditions	56
3.9	Numerical Simulation Results and Conclusions.....	58
4	Experimental Study of a Gerotor Pump by Time-Resolved Particle Image Velocimetry	65
4.1	Introduction to the Experimental Study.....	65
4.2	Principles of TRPIV.....	66
4.3	Tracer particles	66
4.3.1	Fluid mechanical properties.....	67
4.3.2	Light scattering behaviour	68
4.3.3	Selected tracer particles	70
4.4	Camera	71
4.5	Laser.....	71
4.6	Synchronization between camera and laser	72
4.7	Mathematical background of statistical PIV Evaluation	73
4.8	Software	76
4.9	Experimental arrangement.....	76
4.9.1	Test bench	76
4.9.2	Operating conditions.....	78
4.10	Experimental Results	80
4.11	Evaluation of Experimental Results	87
5	Final Conclusions and Future Work	91
5.1	Introduction to final conclusions	91
5.2	Limitations of the present work	92

5.3	Progress achieved	92
5.4	Final Conclusions	93
5.5	Future Work.....	98
	References	99

List of Figures

Figure 1.1: Gerotor pump of the lubrication system of a combustion engine	2
Figure 1.2: Gear wheels in the position of maximum volume chamber in the pump body	2
Figure 1.3: Diagram of the State of the Art	10
Figure 2.1: Structure of the GeroLAB Package	16
Figure 2.2: Minimum clearance parameters. a) In reference position. b) Example of input parameters to minimum clearance module.	17
Figure 2.3: Graphic window of minimum clearance history for PZ9e285 gear set by using constant delayed contact angle (con- stant d.c.a) and variable delayed contact angle (variable d.c.a)	17
Figure 2.4: Specific zones and fluid circulation boundaries.	19
Figure 2.5: Geometrical variables for the port areas calculation.....	22
Figure 2.6: Groove angles for the original gerotor pump.....	23
Figure 2.7: Variables used for the generation of a new port areas geometry	24
Figure 2.8: Examples of geometry of the port areas. a) Case 0 (original geometry). b) Case 1. c) Case 7. d) Case 8.	26
Figure 2.9: Input parameters windows in Effective Port Areas module	26
Figure 2.10: Graphic windows of calculated effective port areas	25
Figure 2.11: Position of reference for the study of volume and its variation	27
Figure 2.12: Submodel for the BondGraph simulation of a chamber	28
Figure 2.14: Discharge and suction effective port areas for a whole rotation.....	30
Figure 2.15: Effective port areas for cases 1, 2, 3 and 4.	31
Figure 2.16: BondGraph flow ripple for cases 1, 2, 3 and 4.	31
Figure 2.17: Effective port areas for cases 2 and 13.	32
Figure 2.18: Detail of the effective port areas for cases 2 and 13.....	32
Figure 2.19: BondGraph flow ripple for cases 2 and 13.	33
Figure 3.1: Example of an unstructured staggered grid.	40
Figure 3.2: Teeth contact simulation by using the viscous wall-cell strategy: (a) Z interteeth clearances and no contact points; (b) 3D Z contact points and no interteeth clearances.	44
Figure 3.3: Calculation time of the two contact point strategies	45
Figure 3.4: Pseudo-code of the viscous wall-cell strategy (left) and gearing contact point strategy (right)	46
Figure 3.5: Computational domain zones: a) Isometric, b) Back, c) Front and d) Left.	47
Figure 3.6: Port areas zone: a) General view and b) Detailed mesh including discharge tube and port area.	48
Figure 3.7: Gearing zone: a) General view and b) Detailed mesh of a chamber.	48
Figure 3.8: Base zone: a) General view of the lower area, b) Detailed mesh of the lower area, c) General	

view of the upper area and d) Detailed mesh of the upper area	49
Figure 3.9: Spring-based smoothing on interior nodes. a) Start. b) End. Adapted from ANSYS FLUENT's Theory Guide.....	50
Figure 3.10: Mesh deformation and local remeshing for gearing mesh zone, between 2 time steps.....	52
Figure 3.11: GeroLAB analytical and laminar CFD results of the instantaneous flow at the outlet port (0 MPa and 7.5 rpm)	54
Figure 3.12: Instantaneous flow at the outlet port, 472 and 2016 rpm inner gear. Laminar CFD results by simulating no contact points and Z contact points with a pressure of 0, 0.5, 1 and 2 MPa	54
Figure 3.13: Detail of instantaneous flow at the outlet port, 472 and 2016 rpm inner gear. Laminar CFD results by simulating no contact points and Z contact points with a pressure of 0, 0.5, 1 and 2 MPa	55
Figure 3.14: BondGraph ideal and with leakage (Qf,pt), and laminar CFD results of the instantaneous flow at the outlet port (0.5 MPa and 2016 rpm)	56
Figure 3.15: Comparative between results obtained through laminar and turbulent models	57
Figure 3.16: Detail of the comparative between laminar and turbulent models	57
Figure 3.17: Instantaneous flow rate in the outlet pipe.	59
Figure 3.18: Flow pulsation in maximum area chamber	59
Figure 3.19: Volume streamtraces.....	60
Figure 3.20: Volume streamtraces in suction (left) and discharge (right) pipes	60
Figure 3.21: Volume streamtraces, XY view	61
Figure 3.22: Surface streamtraces and contours of velocity between trochoidal profiles	61
Figure 3.23: Minimum radial clearance for a complete rotation of the gearing (tooth 1).....	62
Figure 3.24: Minimum radial clearance for a complete rotation of the gearing (all teeth)	62
Figure 4.1: Typical experimental assembly for a PIV study in a Gerotor pump.....	67
Figure 4.2: Light scattering by a glass particle of diameter D_p in water with a) $D_p=1 \mu\text{m}$, b) $D_p=10 \mu\text{m}$ and c) $D_p=30 \mu\text{m}$. <i>Adapted from Raffel et al.[66].</i>	70
Figure 4.3: Image intensity field in an interrogation area, at two consecutive recorded frames.....	74
Figure 4.4: Example of the formation of a cross-correlation plane by direct cross-correlation.....	75
Figure 4.5: Image pre-processing. a) Original image. b) Subtract background treatment	75
Figure 4.6: Installation of the pump in the test bench	76
Figure 4.7: Detailed view of the Gerotor pump in the test bench	77
Figure 4.8: Methacrylate chasing. a) 3d CAD. b) Image of the assembly.	77
Figure 4.9: Experimental hydraulic circuit.....	78
Figure 4.10: Experimental instantaneous flow in the outlet pipe.....	80
Figure 4.11: Experimental flow pulsation in the maximum area chamber	81
Figure 4.12: Experimental velocity vector field in the outlet pipe	81
Figure 4.13: Experimental velocity contours and vector field in the outlet pipe.....	82
Figure 4.14: Example of experimental velocity vectors in the outlet pipe.....	82
Figure 4.15: Location of the interrogation area: a) Outlet tube and b) Maximum area chamber ($\omega_e=270^\circ$)	83
Figure 4.16: PIV experimental results for $\omega_e=90^\circ$	84

Figure 4.17: PIV experimental results for $\omega_e=180^\circ$	85
Figure 4.18: PIV experimental results for $\omega_e=270^\circ$	86
Figure 4.19: Comparative of the flow in the maximum area chamber.....	88
Figure 4.20: Comparative of the flow in the discharge tube.....	89

List of Tables

Table 2.1: List of variables used for the calculation of the port areas.....	22
Table 2.2: Variables used for the generation of a new port areas geometry	24
Table 2.3: Main parameters od the studied geometries. Case 0 corresponds with the original gerotor geometry.....	25
Table 2.4: Irregularity flow indices for the simulated geometries	33
Table 3.1: Results of the grid independence study.....	53
Table 3.2: Geometry, operation conditions and fluid properties of the CFD simulations	58
Table 4.1: Specifications of the high velocity digital camera	71
Table 4.2: Specifications of Monocrom LU80250-FSAC	72
Table 4.3: Specifications of TG2000 20MHz DDS function generator (square waveform).....	72
Table 4.4: Software used in the experimental study.....	76
Table 4.5: Characteristics of the experimental testing	79

Notation

Roman Symbols

a_P/a_{nb}	Coefficients of the unscaled residuals
\vec{a}	Fluid acceleration
\vec{A}_j	Face area vector of the j face in a control volume
A_{za}	Variation of the suction zone area
A_{zi}	Variation of the discharge zone area
b	Coefficient of the scaled residuals
c_v	Theoretical volumetric capacity
$C_{1\epsilon}, C_{2\epsilon}, C_{3\epsilon}$	k - ϵ turbulence model constants
C_μ	k - ϵ turbulence model constant
d	Distance between a marked cell's centroid and the theoretical contact point
\mathbf{d}	Displacements of particles located in the vicinity of the optical axis
d_{max}	Radius of the zone containing the <i>contact wall cells</i>
d_o	Diameter of the outlet port pipe
d_p	Particle diameter
D_{ei}	External diameter through the tips of the teeth of the inner gear
\mathbf{D}	Particles displacements
\vec{F}_d	Stokes' drag force
\vec{F}_l	Force on a mesh node
g	Gravitational acceleration
G_b	Generation of turbulence kinetic energy due to buoyancy
G_k	Generation of turbulence kinetic energy due to the mean velocity gradients
IA	Size of the interrogation area
I_g	Image intensity field
k	Turbulent kinetic energy

k_{ij}	Spring constant between node i and its neighbour j
n_i	Number of neighbouring nodes connected to the node i
n_f	Number of faces of the control volume
O_1	Center of the internal gear wheel
O_2	Center of the external gear wheel
P_1/P_2	Contact points that seal chamber at its maximum area position, where P_1 seals the chamber from the suction zone and P_2 seals it from the discharge zone.
q	Normalized particle diameter
Q	Volumetric flow rate
Q_g	Theoretical volumetric flow rate
R_{II}	Cross-correlation function
R^ϕ	Scaled residual for the scalar variable ϕ
Re	Reynolds number
S	Modulus of the mean rate-of-strain tensor
S_ϕ	Source term of ϕ .
S_{ij}	Strain rate tensor
S_ε / S_k	User-defined source terms of the turbulence model
S_c	Cell surface
S_e	Surface of an equilateral triangle with the same circumradius of a cell with surface S_c
Sk	Cell equivolume skewness
SC	PIV spatial scale
t	Time
T	Time
T_g	Gearing period
TS	PIV time scale
\vec{u}	Flow velocity vector
\vec{u}_g	Velocity of the moving mesh
\vec{u}_p	Particle velocity
\vec{u}_S	Velocity lag of a particle

v_g	Gravitationally induced velocity of a particle
V	Arbitrary control volume
V_0	Interrogation volume
$X-Y$	Absolute reference coordinate system centered in O_2
$\mathbf{X}_i/\mathbf{X}'_i$	Particles location at time t/t'
y_{fi}	Groove distance formed by the perpendicular distance between parallel lines of fluid circulation boundary ‘fi’ centered on O_1 and the X -axis of the absolute reference coordinate system $X-Y$ centered on O_2
y_{ia}	Groove distance formed by the perpendicular distance between parallel lines of fluid circulation boundary ‘ia’ centered on O_1 and the X -axis of the absolute reference coordinate system $X-Y$ centered on O_2
Y_M	Contribution of the fluctuating dilatation in compressible turbulence to the overall dissipation rate
Z	Number of teeth of the inner gear wheel

Greek Symbols

$\alpha_{pc1}/\alpha_{pc2}$	Angles of the singular points that are centers of circular arcs to evaluate the contact points P_1 and P_2 relative to the x-axis of X-Y absolute reference system centered on O_2
β	Boundary node relaxation
δ_{rfa}	Groove angle defined between the fluid circulation boundary ‘fa’ centered on O_1 and the end of the groove geometry
δ_{rii}	Groove angle defined between the fluid circulation boundary ‘ii’ centered on O_1 and the end of the groove geometry
δ_{fa}	Groove angle defined between the fluid circulation boundary ‘fa’ centered on O_1 and the X -axis of the absolute reference coordinate system $X-Y$ centered on O_2
δ_{ii}	Groove angle defined between the fluid circulation boundary ‘ii’ centered on O_1 and the X -axis of the absolute reference coordinate system $X-Y$ centered on O_2
$\Delta\vec{x}_i/\Delta\vec{x}_j$	Displacement of node i and its neighbour j
$\Delta\vec{x}_{rms}$	Interior and deforming nodes RMS
ε	Dissipation rate of the turbulent kinetic energy
λ	Light wavelength

μ_t	Turbulent viscosity
μ_c	Dynamic viscosity in a <i>contact wall cell</i> in the numerical simulation
μ_{max}	High value of dynamic viscosity to simulate solid-solid boundary condition in the numerical simulation
μ_{oil}	Normal dynamic viscosity of the fluid in the numerical simulation
ρ	Fluid density
ρ_e/ρ_i	Radius vector that sweeps the area between the contact points P_1 and P_2 depending on the angle χ in the profile of external/internal gear wheel.
ρ_f	Fluid density
ρ_p	Particle density
$\sigma_k/\sigma_\varepsilon$	Turbulent Prandtl numbers for k/ε
τ	Point spread function of imaging lens
τ_s	Relaxation time
Γ	Diffusion coefficient.
ϕ	Arbitrary scalar variable.
ϕ_P/ϕ_{nb}	Value of ϕ in the center/neighbouring node
χ_e/χ_i	Angle for the contact points of the profile of the external/internal gear wheel, for a generic rotation angle of the internal gear wheel
χ_{fa}/χ_{fi}	Zone angle formed between the contact point P_{fa}/P_{fi} and the X axis of X-Y absolute reference system centered on O_2
χ_{ii}/χ_{ia}	Zone angle formed between the contact point P_{ii}/P_{ia} and the X axis of X-Y absolute reference system centered on O_2
χ_1/χ_2	Contact angle of the point P_1/ P_2 on the x-axis of X-Y absolute reference system centered on O_2
ω_i	Inner rotary velocity
$\omega_{i,max}$	Maximum inner rotary velocity

1 Introduction

1.1 Preamble

Positive displacements pumps, as currently designed, produce significant flow pulsations that result in pressure pulsations. These pulsations contribute to the global noise generated by the installation. Moreover, they interact with the system where the pump is connected shortening the life of both the pump and circuit components.

Rotary trochoidal gear pump, a type of rotary positive displacement machine, has characteristics that make it suitable for many applications fields. Nowadays, in cases like additivation and dosage, these applications have not been completely developed, and present a growing potential in the industrial world, such as in new diesel engines generation or in medical applications. Some uses of rotary trochoidal machines are:

- Lubrication systems of internal combustion engines.
- Fuel pumps of internal combustion engines.
- Car power steering units.
- High speed gas compressors.

In recent years the LABSON research team members have focused much of their efforts in research and development of volumetric positive displacement pumps, especially in external gear pumps and trochoidal gear pumps. The present thesis uses this *know-how* to continue increasing knowledge about trochoidal gear pumps, by adding new more realistic approaches to the analytical and simulation models developed up to the present, and creating an experimental procedure to its study.

1.2 Gerotor pump

Gear pumps using trochoidal profiles are often called gerotor pumps, an acronym in English of the words 'Generated ROTOR'. The pump consists of four main parts: inner gear wheel, outer gear wheel, the housing or pump's body and a cover to produce the closure of the assembly. The gear consists of a pinion

meshing with a toothed ring or crown. Gear teeth are generated by trochoidal profiles. In order to get the gear mesh, the inner gear wheel (pinion) has a tooth less than the outer gear wheel (crown).



Figure 1.1: Gerotor pump of the lubrication system of a combustion engine.

About its operation, the inner gear wheel receives torque from the motor shaft and it is responsible for transmitting the rotation torque to the outer gear wheel, so that each lobe of the internal gear slips in permanent contact with the surface of the outer gear wheel. These contact points between both wheels form a number of watertight chambers equal to the number of teeth of the outer gear, keeping the fluid contained in them.

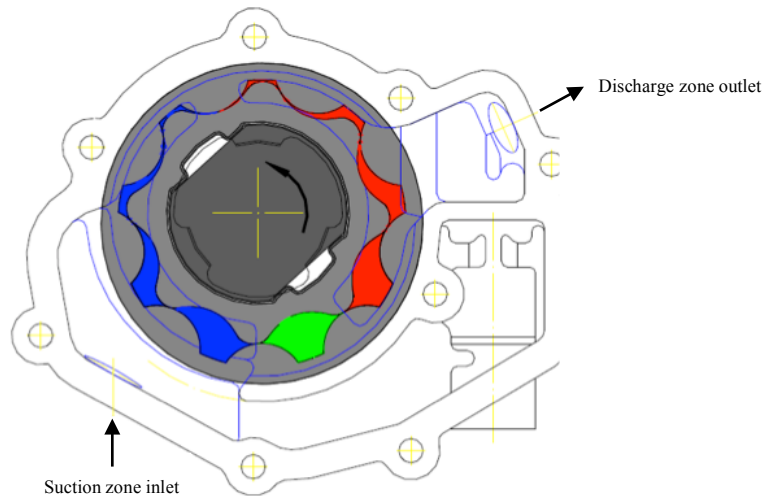


Figure 1.2: Gear wheels in the position of maximum volume chamber in the pump body

During pumping action, chambers are always connected sequentially to the suction port/area and the discharge port/area, except when chambers get their maximum and minimum volume. In both cases, the chamber is isolated from the two areas (Figure 1.2). The pumping action is produced by varying the

volume of the watertight chambers with full rotation of the gear. Chambers connected and open to the suction area increases their volume, and consequently, there takes place a depression that allows the entry of fluid filling the chambers. On the other hand, chambers connected and open to the discharge area reduce their volume, displacing the fluid to the discharge area. The fluid dynamics of this interaction trochoidal gear - suction/discharge ports are the basis of the virtues of its characteristics due to the flow passage geometry.

1.3 Thesis objectives and scope

The main objective of this thesis is to develop a set of design tools applied to trochoidal gear pumps, from the viewpoint of the fluid dynamical performance of the pump. These design tools are aimed to help improving two of the main performance indices of the pump: the volumetric capacity and the flow irregularity¹, leading the designer to more efficient new designs of gerotor pump. On the one hand, the volumetric capacity is related with the pump's efficiency, and increases in this particular index result in a higher efficiency of the pump. On the other hand, flow irregularity measures de flow ripple² generated by the pump, and by reducing this index, the life of both the pump and the installation can be extended, as phenomena like fatigue are attenuated.

The present work does not focus on mechanical characteristics of the pump, and phenomena like wear or aspects like deformation of materials. Consequently, all considerations are made from the viewpoint of fluid dynamic behaviour.

This has been achieved through the use of analytical, simulation and experimental procedures. For a better understanding of the main contributions made in these areas, the tools developed in this thesis are divided according to the performance variable to which they are related: the volumetric capacity and the irregularity index.

The main contributions made in this thesis from the point of view of characterising the volumetric capacity and efficiency are the following:

- Analytical calculation through the *Volumetric Characteristics Module* contained in GeroLAB Package.

¹ The *flow irregularity* quantifies difference between the maximum and minimum values of the instantaneous flow, related to its average value.

² The *flow ripple* is the parameter that characterizes the performance of Gerotor pumps that can be seen as fluctuations in the instantaneous flow generated by the pump. It is inherent to this type of pumps, and it cannot be directly measured. Although it cannot be eliminated, efforts are focused towards reducing it as maximum as possible.

- Dynamical simulation using a BondGraph model, which gives the variation of the chamber³ volume for a complete rotation of the pump, allowing the volumetric capacity determination.
- Numerical simulation of the flow field in the chamber, by means of Computational Fluid Dynamics: the volumetric capacity is determined through a 3D model of the pump including leakage phenomena, by integrating the simulated flow in the chamber for a complete rotation of the inner gear wheel.
- Experimental characterization of the volumetric capacity by means of Particle Image Velocimetry: the gear performance is evaluated by properly studying the variation or the instantaneous flow in the chamber.

Regarding to the flow irregularity characterization, the main contributions made in this thesis are:

- Analytical calculation through the *Effective Port Areas Module* created for the existing GeroLAB Package. The effective port areas are the restricted area that a chamber exposes to the inlet or outlet port, depending on its location. The instantaneous flow rate is influenced by the change in volume of the chambers, which in turn depends on the geometry of the port areas. The calculation of the effective port areas allows the determination of the flow irregularity of the pump.
- Dynamical simulation using a BondGraph model, which gives the instantaneous flow ripple generated by the pump. This model uses data given by the *Effective Port Areas Module* and *Minimum Clearance Module*, both created for the existing GeroLAB Package.
- Numerical simulation of the flow field in the outlet pipe, by means of Computational Fluid Dynamics: the flow irregularity is determined through a 3D model of the pump containing leakage phenomena, by integrating the simulated flow in the outlet pipe, for a complete rotation of the inner gear wheel. Besides, a new strategy to simulate the solid contact between trochoidal gears named *Gearing Contact Point* has been created. In addition, the influence of simulating the contact points between the gear wheels is studied.
- Experimental characterization of the flow irregularity by means of Particle Image Velocimetry: it allows the evaluation of the pump performance through the study of the instantaneous flow in the outlet pipe of the pump.

³ A *chamber* is defined as each of the fluid volumes comprised between two consecutive contact points (in the zone of fluid between inner and outer gears).

1.4 Organization of the Thesis

This thesis is divided into five chapters and the references section.

The present chapter is an introduction to the thesis.

Chapter 2 presents the analytical models used in the present work. It contains the new modules created for the GeroLAB Package Software, *Minimum Clearance Module* and *Effective Port Areas Module*. It also shows the results of the BondGraph simulations, one of whose inputs are the effective port areas obtained through GeroLAB.

Chapter 3 contains the theory and considerations related to the numerical simulations. It presents the selected numerical schemes and turbulence model. The mesh zones are described, including the details of the mesh deformation algorithm and its quality, and the grid independence study. Special attention is paid to the *Gearing Contact Point* strategy, which reduces significantly the computational cost of the simulations.

Chapter 4 presents the main aspects of the acquisition and treatment of data by means of the Time-Resolved Particle Velocimetry (TRPIV). Next, the experimental procedure of the present project is presented: selected devices and tracer particles, mathematical considerations, chosen software and experimental arrangement. It includes the main results of the experimental study and its evaluation.

Finally in Chapter 5 simulation, analytical and experimental results are discussed, and final conclusions are given. Besides, suggestions about the possible future research are also presented in this chapter.

1.5 State of the Art

This section presents a summary of the technical documentation which access has been possible that is related to the main aspects of the gerotor pump. For a better understanding, this information is presented in its main issues (Figure 1.3): theoretical basis, simulation and experimental studies.

Regarding the basic theory, Ansdale (Ansdale and Lockley, 1968) derives closed-form equations of the geometry for two types of conjugate envelope. Those authors demonstrated the value of the existing closed-form equations in the design of a Wankel rotary engine. Colbourne (Colbourne, 1974) is one of the first researchers in describing, defining and classifying trochoidal curves and their envelopes. The same author (Coulborne, 1976) describes a method for calculating the tooth contact stresses in internal gear pumps, and it has been shown that a considerable reduction can be achieved in the maximum contact stress by altering the proportions commonly used in existing pumps. Robinson and Lyon (Robinson and

Lyon, 1976) are able to modify the equations by introducing a constant, which accounts for the space that is required in the sealing design.

Maiti and Sinha (Maiti and Sinha, 1988) develop a kinematic analysis that has been carried out to investigate the pattern of rolling and sliding in the load transmitting contact regions. The authors present a generalized method developed to find out and analyse the flow rate, ripple, and speed variation in different kinematic models (Maiti and Sinha, 1990). Maiti (Maiti, 1992) presents the theoretical guidelines for selecting the inlet-outlet port sizes, their position and sequences of the flow distributor valves used in epitrochoid generated rotary piston machine type of hydrostatic units, which have been established in the presented analysis.

Beard (Beard, Yannitell and Pennock, 1992) derives relationships that show the influence of the trochoid ratio, the pin size ratio, and the radius of the generating pin on the curvature of the epitrochoidal gerotor.

Shung and Pennock (Shung and Pennock, 1994) present in a unified and compact way the equations of trochoid curves. Stryczek (1990 and 1996) devises a very complete basic theory, and shows a new study of properties of trochoidal profiles for the use of complete trochoidal curves in gears working as pump and oleo-hydraulic engine.

Mimmi and Pennacchi (Mimmi and Pennacchi, 2000), with a general method, show the analytical condition for avoiding undercutting by using the concept of the limit curve. Mancò (Mancò et al, 2000) presents a general procedure for the computerized design of gerotor lubricating pumps for internal combustion engines.

Ye (Ye, 2005) presents a new simple method to derive the formulae for the tooth profile of the small rotor in a cycloid rotor pump. This simplified method yields explicit formulae for calculating limit dimensions of the large rotor to avoid undercutting on the tooth profile of the small rotor. Hsieh (Hsieh, 2009) and Yan (Yan et al., 2009) perform the study of geometries with higher efficiency from the point of view of calculating the volume variation.

Vecchiato (Vecchiato et al., 2001) develops the geometry of rotor conjugated profiles applying the theory of envelopes to a family of parametric curves and analysis of profile meshing. He discusses the determination of singularities and computerized design of pumps with rotor profiles free of singularities. Paffoni (Paffoni, 2003) uses a vector analysis and derived equations for defining the precise geometry of a gear pump using non-conventional profile. From this analysis speed, normal force and pressure are deduced in analytical closed form. Kim (Kim et al., 2006) defines the geometry of the rotors starting from the design parameters and shows the process of choosing the solution which is subject to some limitations in order to limit the pressure angle between the rotors. These authors consider the design optimization.

In connection with *mechanical properties*, Colbourne (Colbourne, 1976) notes that one of the drawbacks in the design of volumetric positive displacement machines using trochoidal profiles is that there are no elements that can be adjusted to compensate for wear of tooth surfaces. Paffoni (Paffoni et al., 2004) carries out an exhaustive analysis of the effects of clearance between teeth on contact stresses in gear pumps of trochoidal profiles.

Ivanovic (Ivanovic et al., 2013) defines a relation between the single geometrical parameters and the values of pressure variation in the pump chambers. He defines certain relations between the operating characteristics of the trochoidal gear pairs, through the theoretical consideration such as the flow rate, pressure variation in the pump chambers and the values of the considered geometrical parameters. He states that, for a fixed gerotor pump with the same number of chambers and the same radius of the root circle, the choice of the smaller values of the trochoid coefficient changes the form of the gearing profile, but it does not significantly change the pump flow.

Mancò (Mancò et al., 2002) controls the flow rate being sucked or delivered in a Gerotor pump, through a rotating sector that alters the effective geometry of kidney ports. He states that it is possible to change the actual displacement of a gerotor pump, introducing one degree of freedom, by one of two methods: rigid rotation of the gearing set against the port plate (requires an additional outer gearing) or, vice versa, simply rotating the port plate. Its basic advantage consists in the possibility of changing the location of maximum and minimum crossover volumes independently. In fact, besides rotation of the whole port plate (which gives the same functionality in the first method) only part of it can be rotated, the other remaining fixed. The preferred method is the partial port plate rotation. He concludes that the variable displacement pump allows attainment of a torque saving more than double with respect to the variable flow pump in the whole working range.

Bonandrini (Bonandrini et al., 2012) show that considering the gears rotating with fixed transmission ratio, for many rotation angles the contact has inadequate pressure angle or it does not exist at all. He establishes the transmission error due to the meshing of the profiles and to modify the design of the machine so that the contact is always assured in the right place, avoiding interference.

Hwang and Hsieh (Hwang and Hsieh, 2006) deeply analyse the epitrochoidal and hypotrochoidal profiles, in particular for cycloidal gearings application, only considering the lower part of the nonundercutting curve. The work outlines a mathematical model to improve pump efficiency and derives a dimensionless equation of nonundercutting. This procedure greatly facilitates the design of parameter within the feasible region to avoid undercutting on the tooth profile or interference between the adjacent pins.

More recently, Yan and Yang (Yan and Yang, 2009) develop a deviation function-based theory and algorithm for designing noncircular pitch-based gerotors and their conjugate rotors. Their method,

however, is general enough that it can also be used to design conventional gerotors with circular pitches. Their subsequent work (Yang et al., 2010) proposes deviation function-based flow rate formulas that can be used whether pitch and generating curves are circular or noncircular. This latter introduces two dimensionless parameters, lobe noncircularity and pitch noncircularity, which allow systematic analysis of gerotor performance.

From the viewpoint of *dynamics*, it is known that flow pulsations inherent to the actual operation of a volumetric positive displacement pump directly contribute to the overall noise emitted by the installation and in the long term, reducing life constituent components (fatigue). Dasgupta (Dasgupta et al., 1996) conducts an interesting study of modelling a hydraulic motor of trochoidal profiles through BondGraph. However, the most complete studies are carried out by Professor Nervegna and his team. In (Fabiani, 1999) they began working on the study of dynamic behaviour of a trochoidal profiles gear pump by AMESim software in its first version. With regard to dynamical simulation, they state that the volume of a generic camera in a generic position can be obtained using two types of analysis: integral-derivative and derivative-integral. They develop several 1D simulation models of positive displacement pumps in the LMS AMESim environment. In particular, very detailed studies have been carried out on gerotor pumps. All significant geometric quantities are calculated analytically as function of the shaft angular position and the current pump displacement. They include, among others, gears profiles and their line of contacts, chamber volume and its derivative, chamber inflow and outflow flow areas, kinematic (ideal) flow ripple.

Mucchi (Mucchi et al., 2010) presents a non-linear lumped kineto-elastodynamic model for the prediction of the dynamic behaviour of external gear pumps. The model can be used in order to analyse the pump dynamic behaviour and to identify the effects of modifications in design and operation parameters, in terms of vibration and dynamic forces. They consider the pressure distribution on gears as time-varying and they state that it depends on the gear eccentricity. The gear eccentricity is calculated in the steady-state condition as a result of the balancing between mean pressure loads, mean meshing force and bearing reactions.

Kim (Kim, Nam and Park, 2006) publishes a paper in which the port plate with the relief grooves is designed by referring to as notch of vane pump and relief groove of piston pump, in order to reduce the pressure pulsation in the gerotor pump.

Vacca and his team, from the Maha Fluid Power Research Center (Purdue University) created the simulation tool HYGESim. It is presented, with verification and design purposes, to perform the entire simulation of external gear machines considering main physical phenomena. It is a multi-domain simulation methodology, including the numerical evaluation of leakage flow in the lubricating gap at gears' lateral sides and the calculation of thrust forces.

Karamooz (Karamooz et al., 2010) develops the optimization cost functions and constraints, according to volumetric, dynamic and geometric properties for an epitrochoidal gear pump. He optimizes two commercial pumps and compare the value of the cost functions with those of the original pump. These comparisons show the improvement of both flow irregularity and wear rate proportional factor in both pumps. In subsequent work, Karamooz (2011) derives mathematical equations for elliptical lobe shape rotors profile and curvature of them, and formulates specific flow and wear rate proportional factor. To reach the minimum wear in rotors teeth, the ellipse shape factor is changed for each value of number of outer rotor teeth in a feasible range and wear rate proportional factor has been resulted. He states that the obtained results compared with the circular pumps with similar parameters and show significant improvement in the wear of the rotors teeth with negligible changes in the specific flow. The paper concludes that it is possible to reduce wear of the rotors of a gerotor pump by using suitable elliptical lobes.

Another aspect taken into consideration by some researchers in recent years is the *CFD simulation* of flow and the many studies being conducted today. CFD is the acronym of Computational Fluid Dynamics, and it is the fluid dynamic analysis using finite-volume computation. In literature, there are plenty of works based on CFD but very few are aimed at positive volumetric displacement machines (Iudicello and Mitchell, 2002), and in general there is a gap in the implementation of these studies and knowledge into trochoidal gear pumps. However, we must highlight the work done by Kumar (Kumar and Manonmani, 2010) that optimizes the design of the intake channel in a gerotor pump, not considering the effects of cavitation in the suction line.

CFD models of normal gerotor pumps have been used to improve gerotor designs in many engineering applications for the last decades. In 1997, Jiang and Perng (Jiang and Perng, 1997) created the first full 3D transient CFD model for a gerotor pump and included a cavitation model. Their model successfully predicted gerotor pump volumetric efficiency loses due to cavitation. Kini (Kini et al., 2005) couples CFD simulation with a structural solver to determine deflection of the cover plate in the pump assembly due to variation in internal pressure profiles during operation. Zhang (Zhang et al., 2006) studies the effects of the inlet pressure, tip clearance, porting and the metering groove geometry on pump flow performances and pressure ripples using CFD model. Natchimuthu (Natchimuthu et al., 2010) and Ruvalcaba (Ruvalcaba et al. 2011) also uses CFD to analyze gerotor oil pump flow patterns. Jiang (Jiang et al., 2008) creates a 3D CFD model for crescent pumps, a variation of gerotor pumps with a crescent shaped island between the inner and outer gears.

Biernacki (Biernacki, 2009) analyses the mechanism of induction of stresses and deformations in plastic cycloidal gears used in gerotor pumps using de finite element method and the commercial program ABAQUS.

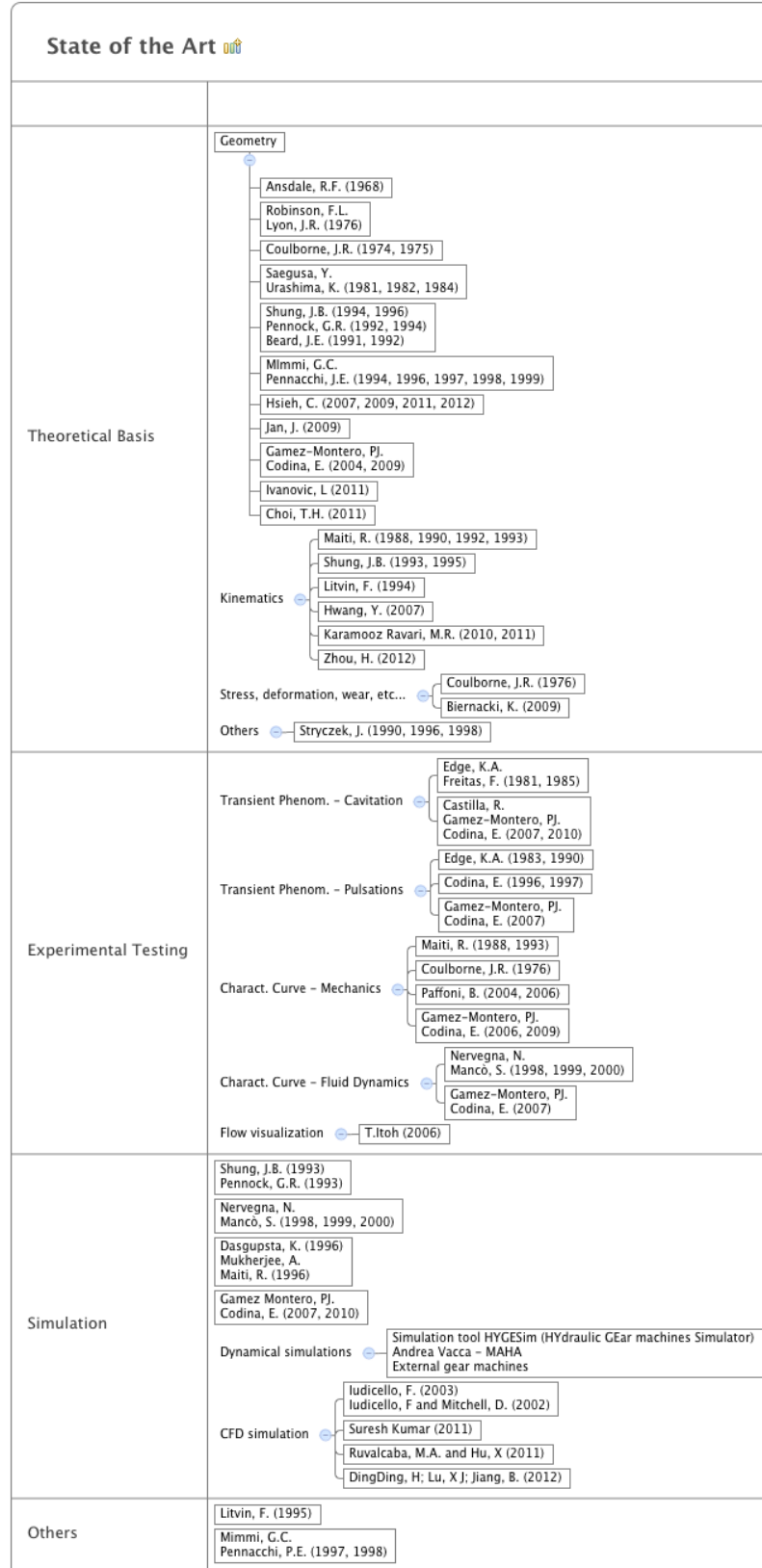


Figure 1.3: Diagram of the State of the Art

There it is observed that there are two parts in the mesh: the active part, where interteeth forces are induced between the teeth of the internal and the external gear, and the passive part, where interteeth forces do not occur. It is found that from the viewpoint of hydraulics, the condition of deformation is more important than the condition of stresses. This is so because, by keeping the stresses lower than the acceptable, it is at the same time possible to achieve deformations and clearances greater than the extreme, which causes flaws in the pumping process, as well as lowering of the working pressure and pump efficiency. In general, the gear deformations can be reduced in two ways: by applying a higher-strength plastic or by modifying the cycloidal gear set design.

Hsieh (Hsieh, 2011) conducts fluid and dynamics analyses using dynamic models that allow continuous simulation of the fluid and stress variation during gerotor operation. Specifically, these models examine how the motion of a gerotor pump whose outer tooth profile is formed by an epicycloid and hypocycloid is affected by varying the tooth profile's span angle; that is, the angle between the two inflections points of a concave curve on the outer rotor. The method of curvature difference is also used to show that when the outer rotors have the same volume, the sealing performance of the rotor profile remains the same across various span angle designs. The fluid dynamics analysis, particularly, by simulating fluid dynamics inside the pump using a commercial CFD package (PumpLinx) and illustrating the effect of three distinct span angle designs on gerotor performance and motion, should provide valuable guidance for improving pump performance. This analysis, however, neglects the leakage path between the high and low pressure pumping chambers.

Ruvalcaba (Ruvalcaba et al., 2011) develops a three-dimensional CFD methodology to predict the flow performance and pump flow deficiency exhibited in gerotor pumps at different operations conditions. It is shown that cavitation has not a significant influence in the pump flow deficiency, and that tip-to-tip clearance has a critical impact on flow deficiency: imperative attention must be displayed towards the manufacturing tolerances of the gerotor pump.

Choi (Choi et al., 2012) develops an automated program for designing a gerotor and suggested that the tip width of the inner rotor be controlled by inserting a circular-arc curve between the hypocycloid and epicycloid curves. Such insertion eliminates any upper limit on the eccentricity. Choi and colleagues also use a commercial computational fluid dynamics model to calculate flow rate and flow rate irregularity.

Ding (Ding et al., 2012) describes a full 3D transient CFD model for an orbital gerotor motor. A moving/deforming mesh algorithm was introduced and implemented in the commercial CFD software package PumpLinx. It does not account the mechanical and friction loses.

Vacca and his team (Devendran and Vacca, 2013) use a CFD model as a part of the simulation tool HYGESim for the evaluation of leakage flow in the lubricating gap at gears' lateral sides and calculation of thrust forces.

To address the contact problem in a gerotor pump, Gamez-Montero (Gamez-Montero et al., 2003 and 2006) uses a finite element model to calculate the normal maximum contact stress and then compared this method to an experimental prototype model that uses photoelasticity measurement techniques. In other work (Gamez-Montero et al., 2009), they also develop the GeroLAB package to calculate a trochoidal gear pump, contact stresses, and volumetric characteristics. Later, they add minimum clearance and relief groove effective port area modules to the GeroLAB structured methodology, which helps designers enhance the efficiency of a gerotor pump (Gamez-Montero et al., 2012).

In relation to the experimental part, since it is virtually impossible to measure accurately and directly the flow ripple generated by a pump, it should be used indirect measurements. That is measurements of pressure pulses, and estimate the flow ripple with the help of an algorithm. Edge (Edge and Johnston, 1990) proposes a methodology for the calculation algorithm of flow ripple. Nevertheless, these pressure pulses generated by the pump have an interaction also with its own installation. As a consequence, the study of the same pump in different installation could lead to very different pressure pulsations. Named *Secondary Source Method*, this test method for measuring the source flow ripple and source impedance is based on the analysis of the wave propagation characteristics in a circuit which includes the pump under test and an additional source of fluid-borne noise.

Regarding the flow visualization techniques applied in gerotor pumps, only one reference has been found (in Japanese). Itoh (Itoh, 2005) carries out a study of the flow structure and the volumetric efficiency using light-reflecting tracer particles in a transparent model of the pump of external dimensions of 76.8mm and a maximum rotating velocity of 31 rpm. And particularly about Particle Image Velocimetry, developed in the present project, there is not documented work of this procedure applied to trochoidal gear pumps.

Analysing the aforementioned documentation, and according to the author's knowledge, there is a lack of documented work on modelling and simulation tools to improve the design parameters that maximize the specific flow rate and minimize the flow rate irregularity in a gerotor pump.

Dynamical simulation models are very useful to study the response of the pump under different operation conditions, at low computational cost and without the requirement of a large amount of information to be configured by the designer. Its main disadvantage is that they include simplifications that distance them of the real behaviour of the pump. The intricate aspects of the pumping process of a gerotor pump make computational fluid dynamics the appropriate tool for modelling and simulation to provide insights into its flow characteristics. This information could be used in order to complement the

dynamical modelization, trying to approximate them to a more realistic description of the pump's response.

One aspect that is not already resolved is the complete leakage model that properly describes the real behaviour of the pump. Motivated by this fact, this thesis presents a CFD three-dimensional planned to accomplish this objective of clarifying how leakage flow affects the response of the pump. As a consequence, the model includes tolerances between the different pieces that integrate the gerotor pump, and studies the influence of the contact points in the response of the pump.

From the point of view of the experimental study of the gerotor pump, it is virtually impossible to measure accurately and directly the flow ripple generated by the pump, and indirect measures are used in order to characterize its instantaneous flow. That is measurements of pressure pulses, and estimate the flow ripple with the help of an algorithm. The only actual method to validate a new design of trochoidal gear pump is to perform a test in normal operating conditions of the real pump. According to the documented work, there is not an existing procedure to obtain the flow ripple generated by the pump in a directly and accurate measure. Regarding the flow visualization techniques applied to gerotor pumps, only one reference has been found (Itoh, 2005), at low operating rotary velocity, and it does not report values of the flow generated by the pump. And, particularly about Particle Image Velocimetry (PIV), there is not documented work of this procedure applied to trochoidal gear pumps.

According to the author's knowledge, PIV constitutes a suitable tool for the study of the fluid-dynamic behaviour of a real gerotor pump. For instance, it can give information about the flow ripple of the pump, or even the three-dimensional velocity field could be analysed in the suction and discharge port areas. The experimental study by means of PIV could give further and accurate information of the fluid-dynamic real behaviour of the fluid inside the pump.

2 Analytical Approach

2.1 Introduction to the Analytical Approach

As seen in previous chapter, the existing software and methodologies do not address the design of gerotor pumps considering both the minimization of flow irregularity and the maximization of the volumetric efficiency. GeroLAB Package system is a tool that integrates these two approaches and in the present thesis it is complemented by the addition of two new modules that improve its performance.

Dynamical simulation models are very useful to study the response of the pump under different operation conditions, at low computational cost and without require a large amount of information to be configured by the designer. In the present thesis, the dynamical simulation of the mechanism is conducted by means of a BondGraph model, and its equations are integrated in the 20-sim software.

BondGraph is an explicit graphical technique for representing physical systems, first presented by H.M.Paynter in 1959, and since then many researchers have further developed it. The BondGraph technique considers the energy flow, being ideal for simulating the pump as it evaluates instantaneously the temporal evolution of the product pressure-flow. This type of modelization allows adding complexity to the system progressively, by the incorporation of new elements and it eases the physical interpretation of each element. It is possible to start with a very simple modelization of the reality, and gradually complete it until the model is as accurate as desired.

2.2 GeroLAB Package

GeroLAB Package System was created in 2008, by the LABSON research group, at Department of Fluid Mechanics of the Technical University of Catalonia. It was published in the “Journal of Mechanical Design” in 2009, presenting an example of the creation of a real gerotor pump (Gamez-Montero, P.J., 2009).

It is an integrated package system, which is composed of three basic modules: design, volumetric characteristics and contact stress module. As a result, by consecutively following each module, this new tool allows to find the better gear set for the concrete initial required design parameters. This software aims to lead the designer to a better design by improving performance indexes of a new gerotor pump project.

In the present work two new modules of the GeroLAB Package are added: *Minimum Clearance Module* and *Effective Port Areas Module*. The first one is the teeth clearance related to leakage phenomenon and the second one models sharp edges with relief groove effective port area plate, which are related to flow performance.

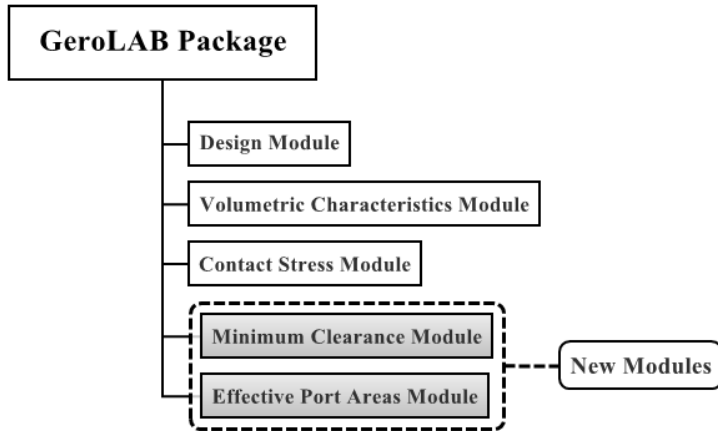


Figure 2.1: Structure of the GeroLAB Package

This new modules, like the previous ones, are programmed in *Scilab* (Scilab, 2012). It is an open software that uses a numerically oriented programming language, largely based on the MATLAB language.

The study of the effective port areas is a very important point to study in gerotor pump design, as these areas have a direct influence on the overall performance of the pump. The instantaneous flow rate is influenced by the change in volume of the chambers, which in turn depends on the geometry of the port areas. Modifying the geometry of the area that connects each chamber with the suction or discharge zone, it is possible to reduce the flow rate irregularity, improving thereby the performance of the gerotor pump.

2.3 Minimum Clearance Module

Minimum clearance module is the first module that takes into account real effects of manufacturing tolerance. The geometrical parameters in reference position for the analysis of this effect that a designer knows of the pump application are shown in Figure 2.2.

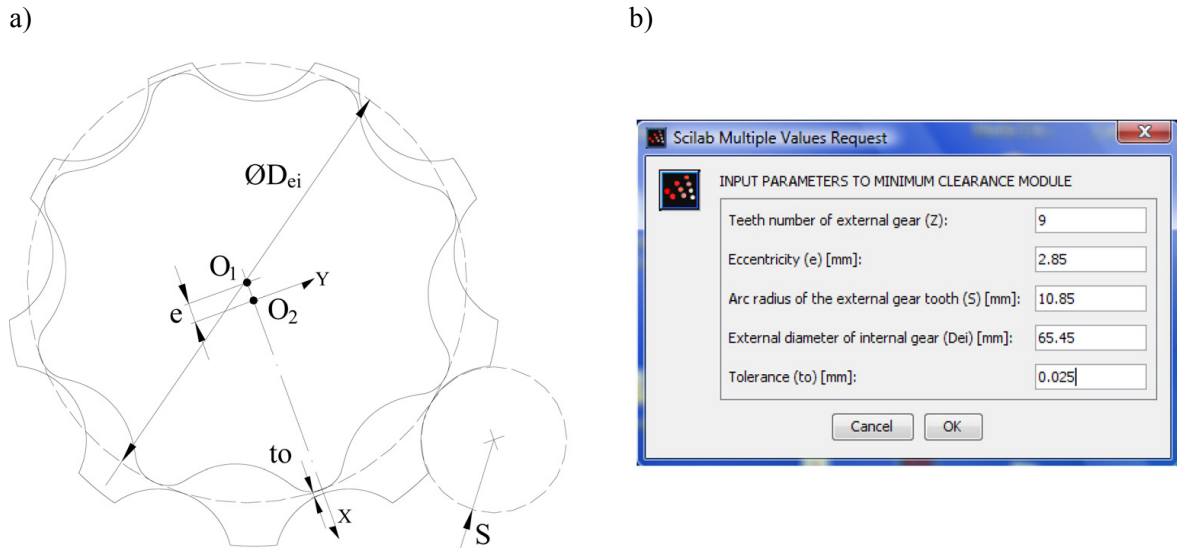


Figure 2.2: Minimum clearance parameters. a) In reference position. b) Example of input parameters to minimum clearance module.

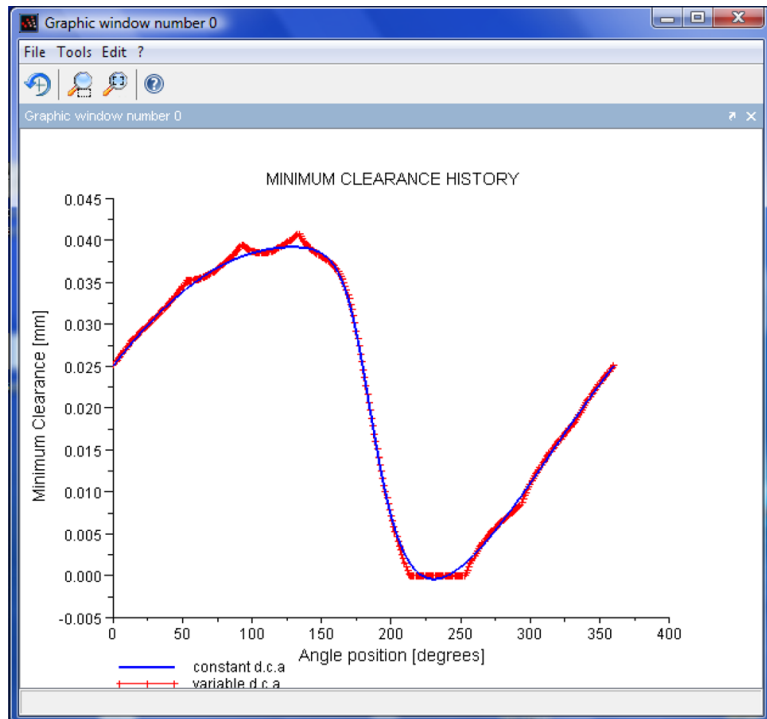


Figure 2.3: Graphic window of minimum clearance history for PZ9e285 gear set by using constant delayed contact angle (constant d.c.a) and variable delayed contact angle (variable d.c.a)

The module follows the methodology of the teeth clearance approach and plots the minimum clearance history (the progression of the minimum distance between the outer and the inner teeth from the reference position of the gear) for a complete rotation of the outer gear. Furthermore, all items of data of interest are saved in a text file. By observing the minimum clearance history in Figure 2.3, when the

delayed contact angle history is taken as variable, the contact is found in an angle of $2\pi/Z$, where Z is the number of teeth of the outer gear wheel. The minimum clearance sets a value of zero (contact) between angles 213 deg and 253 deg. However, when it is taken as constant, the contact is found at an angle of π/Z : the minimum clearance sets a value of zero between angles 222 deg and 242 deg. Consequently, no contact would establish in half of the complete rotation of the gear set and virtual dynamic effects would appear. In conclusion, the delayed contact angle becomes very important in order to evaluate the minimum clearance history.

The module also calculates and plots the radius of curvature of the inner gear which is necessary to evaluate the section history of the teeth clearance passageway that leads to define the leakage flow through the trochoidal profiles.

2.4 Effective Port Areas Module

2.4.1 Specific Zones and Fluid Circulation Boundaries

At a certain angle of the complete rotation of the gear assembly, the variation in the volume of chambers creates a suction area while in another certain angle it creates a discharge area. The change in volume of the sealed chambers can be studied in four areas in a complete rotation of the gear, called *specific areas of fluid* (Figure 2.4).

Suction zone. In this zone, sealed chambers increase its area as the position of contact points varies due to rotation of the gear assembly. This increase in its area, and hence its volume, creates a depression that produces the input of the working fluid into the chamber, filling chambers.

Discharge zone. In this zone, sealed chambers decrease its area as the position of contact points varies due to rotation of the gear assembly. This decrease in its area, and hence its volume, results in a volumetric displacement of fluid, emptying chambers.

Maximum area zone. In this area, chambers reach their maximum surface generated by the position of the contact points in the rotation of the gear assembly. When the position of maximum area is reached, and because of the position of the ports, there is no suction or discharge of the working fluid, and the chamber remains completely isolated.

Minimum area zone. In this area, chambers reach their minimum surface generated by the position of the contact points in the rotation of the gear assembly. When the position of minimum area is reached, and because of the position of the ports, there is no suction or discharge or working fluid remaining the chamber completely isolated.

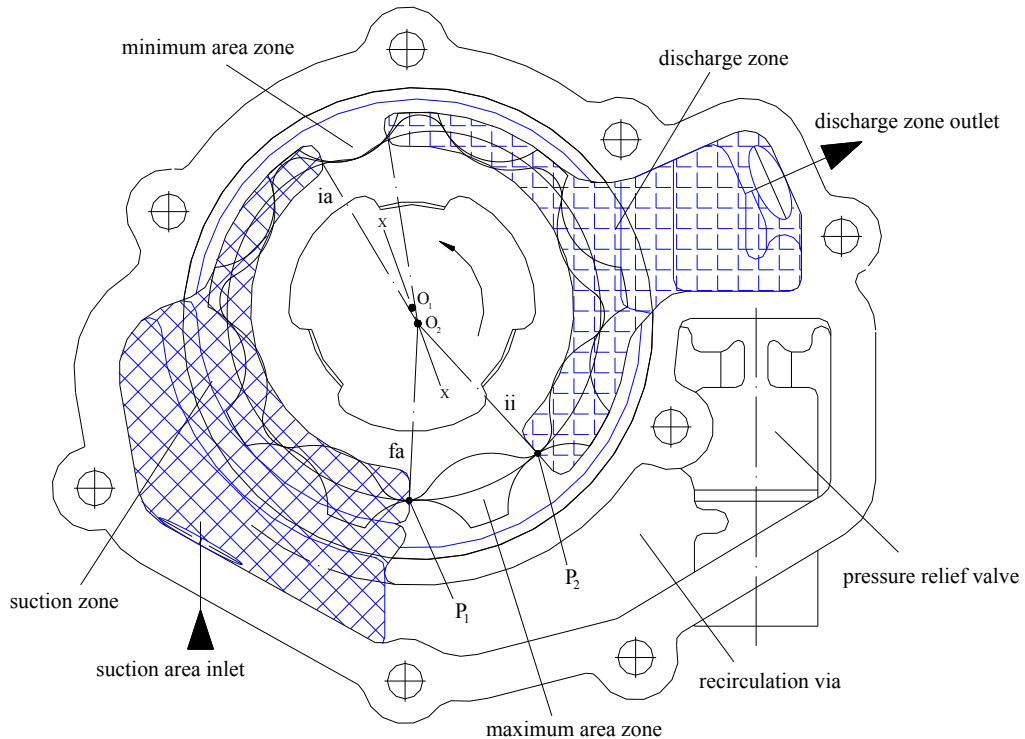


Figure 2.4: Specific zones and fluid circulation boundaries.

The four specific areas of fluid are theoretically defined by the geometry and kinematics of the gear assembly. Constructively, the four areas are affected by the grooves and cavities mechanized in the pump housing. These grooves and cavities are part of the collectors of the suction and discharge areas.

On the one hand, the suction area is formed by a groove mechanized on the housing, having such a geometry that connects all cameras that at this particular time are among the areas of minimum and maximum area. On the other hand, the discharge side is formed by a groove machined on the housing, having such a geometry that connects all cameras that at this particular time are among the areas of maximum and minimum area. The filling and emptying of the chambers is carried out through the grooves mechanized into the case.

The geometric definition of the four zones is determined by four boundaries, called *fluid circulation boundaries*, marked by the two contact points of maximum area and the two contact points of minimum area in a full rotation of gear assembly. For the better understanding of its operation it will be based on the maximum area chamber, which is isolated between the suction and discharge areas (Figure 2.4). The contact points that make the chamber watertight at its maximum area called P₁ for the one that isolates the chamber of the suction zone and P₂ for which isolates the chamber from the discharge side. Fluid circulation boundaries are defined as following:

Discharge Start Boundary, ii. At this point, the chamber starts to be exposed to the discharge side so that its area is located between the discharge side and the maximum area zone. It creates a restricted flow section for the emptying of the chamber due to the discharge start boundary.

Discharge End Boundary, fi. When the contact point P_2 crosses this boundary, the chamber starts being exposed between the discharge and minimum area zones. It creates a restricted flow section for the emptying of the chamber due to the discharge end boundary.

Suction Start Boundary, ia. When the contact point P_2 crosses this boundary, the chamber starts being exposed between the suction and discharge zones. It creates a restricted flow section for the filling of the chamber due to the suction start boundary.

Suction End Boundary, fa. At this point, the chamber starts being exposed between the suction and maximum area zones. It creates a restricted flow section for the filling of the chamber due to the suction end boundary.

2.4.2 Analytical Expressions

The present section shows only the final expressions for the calculation of the effective port areas, and deductions are omitted up to this point. Table 2.1 shows all variables used in the expressions of this section, some of them represented in (2.2) and (2.1).

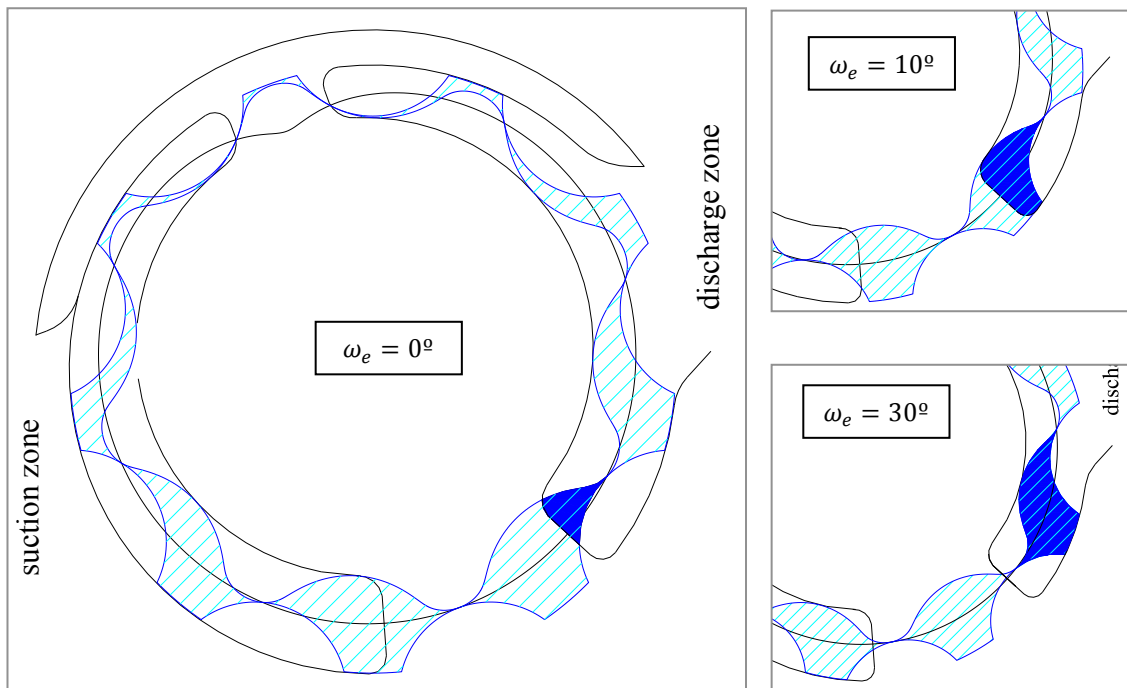


Figure 2.5: Example of discharge port area and its evolution for a chamber

The calculated area corresponds to the area to which a chamber is exposed, to the suction or discharge zone, as it stands. That is, the evolution of the area that is calculated is not the total of each chamber, but that corresponds to the portion that is exposed to each of the discharge or suction zones. This corresponds to the passage through which fluid will pass to enter or exit each chamber and it is represented in Figure 2.5

The following expressions describe the variation of the area in the suction and discharge zones, respectively.

$$A_{zi}(\alpha_{pc1}) = \begin{cases} \frac{1}{2} \int_{\chi_{ii}(\alpha_{pc} = P_{ii})}^{\chi_2(\alpha_{pc1})} [\rho_e(\chi_e)]^2 d\chi - \frac{1}{2} \int_{\chi_{ii}(\alpha_{pc} = P_{ii})}^{\chi_2(\alpha_{pc1})} [\rho_i(\chi_i)]^2 d\chi & \text{if } \alpha_{pc1} \leq \alpha_{pc1=P_{ii}} \\ \frac{1}{2} \int_{\chi_1(\alpha_{pc1})}^{\chi_2(\alpha_{pc1})} [\rho_e(\chi_e)]^2 d\chi - \frac{1}{2} \int_{\chi_1(\alpha_{pc1})}^{\chi_2(\alpha_{pc1})} [\rho_i(\chi_i)]^2 d\chi & \text{if } \alpha_{pc1=P_{ii}} < \alpha_{pc1} < \alpha_{pc2=P_{fi}} \\ \frac{1}{2} \int_{\chi_1(\alpha_{pc1})}^{\chi_{fi}(\alpha_{pc} = P_{fi})} [\rho_e(\chi_e)]^2 d\chi - \frac{1}{2} \int_{\chi_1(\alpha_{pc1})}^{\chi_{fi}(\alpha_{pc} = P_{fi})} [\rho_i(\chi_i)]^2 d\chi & \text{if } \alpha_{pc1} \geq \alpha_{pc2=P_{fi}} \\ 0 & \text{if } \alpha_{pc1=P_{fi}} < \alpha_{pc1} < \alpha_{pc2=P_{ii}} \end{cases} \quad (2.1)$$

$$A_{za}(\alpha_{pc1}) = \begin{cases} \frac{1}{2} \int_{\chi_{ia}(\alpha_{pc} = P_{ia})}^{\chi_2(\alpha_{pc1})} [\rho_e(\chi_e)]^2 d\chi - \frac{1}{2} \int_{\chi_{ia}(\alpha_{pc} = P_{ia})}^{\chi_2(\alpha_{pc1})} [\rho_i(\chi_i)]^2 d\chi & \text{if } \alpha_{pc1} \leq \alpha_{pc1=P_{ia}} \\ \frac{1}{2} \int_{\chi_1(\alpha_{pc1})}^{\chi_2(\alpha_{pc1})} [\rho_e(\chi_e)]^2 d\chi - \frac{1}{2} \int_{\chi_1(\alpha_{pc1})}^{\chi_2(\alpha_{pc1})} [\rho_i(\chi_i)]^2 d\chi & \text{if } \alpha_{pc1=P_{ia}} < \alpha_{pc1} < \alpha_{pc2=P_{fa}} \\ \frac{1}{2} \int_{\chi_1(\alpha_{pc1})}^{\chi_{fa}(\alpha_{pc} = P_{fa})} [\rho_e(\chi_e)]^2 d\chi - \frac{1}{2} \int_{\chi_1(\alpha_{pc1})}^{\chi_{fa}(\alpha_{pc} = P_{fa})} [\rho_i(\chi_i)]^2 d\chi & \text{if } \alpha_{pc1} \geq \alpha_{pc2=P_{fa}} \\ 0 & \text{if } \alpha_{pc1=P_{fa}} < \alpha_{pc1} < \alpha_{pc2=P_{ia}} \end{cases} \quad (2.2)$$

$A_{za}(\alpha_{pc1})$	Variation of the suction zone area.
$A_{zi}(\alpha_{pc1})$	Variation of the discharge zone area.
$\chi_1(\alpha_{pc1})$	Contact angle of the point P_1 on the x-axis of X-Y absolute reference system centered on O_2 .
$\chi_2(\alpha_{pc1})$	Contact angle of the point P_2 on the x-axis of X-Y absolute reference system centered on O_2 .
$\chi_{ii}(\alpha_{pc} = P_{ii})$	Zone angle formed between the contact point P_{ii} and the X axis of X-Y absolute reference system centered on O_2 .
$\chi_{ia}(\alpha_{pc} = P_{ia})$	Zone angle formed between the contact point P_{ia} and the X axis of X-Y absolute reference system centered on O_2 .
$\chi_{fa}(\alpha_{pc} = P_{fa})$	Zone angle formed between the contact point P_{fa} and the X axis of X-Y absolute reference system centered on O_2 .
$\chi_{fi}(\alpha_{pc} = P_{fi})$	Zone angle formed between the contact point P_{fi} and the X axis of X-Y absolute reference system centered on O_2 .

χ_e	Angle for the contact points of the profile of the external gear wheel, for a generic rotation angle of the internal gear wheel
χ_i	Angle for the contact points of the profile of the internal gear wheel, for a generic rotation angle of the internal gear wheel.
ρ_e	Radius vector that sweeps the area between the contact points P_1 and P_2 depending on the angle χ in the profile of external gear wheel.
ρ_i	Radius vector that sweeps the area between the contact points P_1 and P_2 depending on the angle χ in the profile of internal gear wheel.
P_1 and P_2	Contact points that seal chamber at its maximum area position, where P_1 seals the chamber from the suction zone and P_2 seals it from the discharge zone.
α_{pc1} and α_{pc2}	Angles of the singular points that are centers of circular arcs to evaluate the contact points P_1 and P_2 relative to the x-axis of X-Y absolute reference system centered on O_2 , where $\alpha_{pc2} = \alpha_{pc1} + \frac{2\pi}{z}$
$\alpha_{pc1} = P_{ii}$ / $\alpha_{pc2} = P_{ii}$	Angle for the calculation of the zone contact point P_{ii} for the contact points P_1 and P_2 respectively, where $\alpha_{pc2=P_{ii}} = \alpha_{pc1=P_{ii}} - \Delta\alpha_{pc} = \alpha_{pc1=P_{ii}} - \frac{2\pi}{z}$
$\alpha_{pc1} = P_{fi}$ / $\alpha_{pc2} = P_{fi}$	Angle for the calculation of the zone contact point P_{fi} for the contact points P_1 and P_2 respectively, where $\alpha_{pc2=P_{fi}} = \alpha_{pc1=P_{fi}} - \Delta\alpha_{pc} = \alpha_{pc1=P_{fi}} - \frac{2\pi}{z}$
$\alpha_{pc1} = P_{ia}$ / $\alpha_{pc2} = P_{ia}$	Angle for the calculation of the zone contact point P_{ia} for the contact points P_1 and P_2 respectively, where $\alpha_{pc2=P_{ia}} = \alpha_{pc1=P_{ia}} - \Delta\alpha_{pc} = \alpha_{pc1=P_{ia}} - \frac{2\pi}{z}$
$\alpha_{pc1} = P_{fa}$ / $\alpha_{pc2} = P_{fa}$	Angle for the calculation of the zone contact point P_{fa} for the contact points P_1 and P_2 respectively, where $\alpha_{pc2=P_{fa}} = \alpha_{pc1=P_{fa}} - \Delta\alpha_{pc} = \alpha_{pc1=P_{fa}} - \frac{2\pi}{z}$

Table 2.1: List of variables used for the calculation of the port areas.

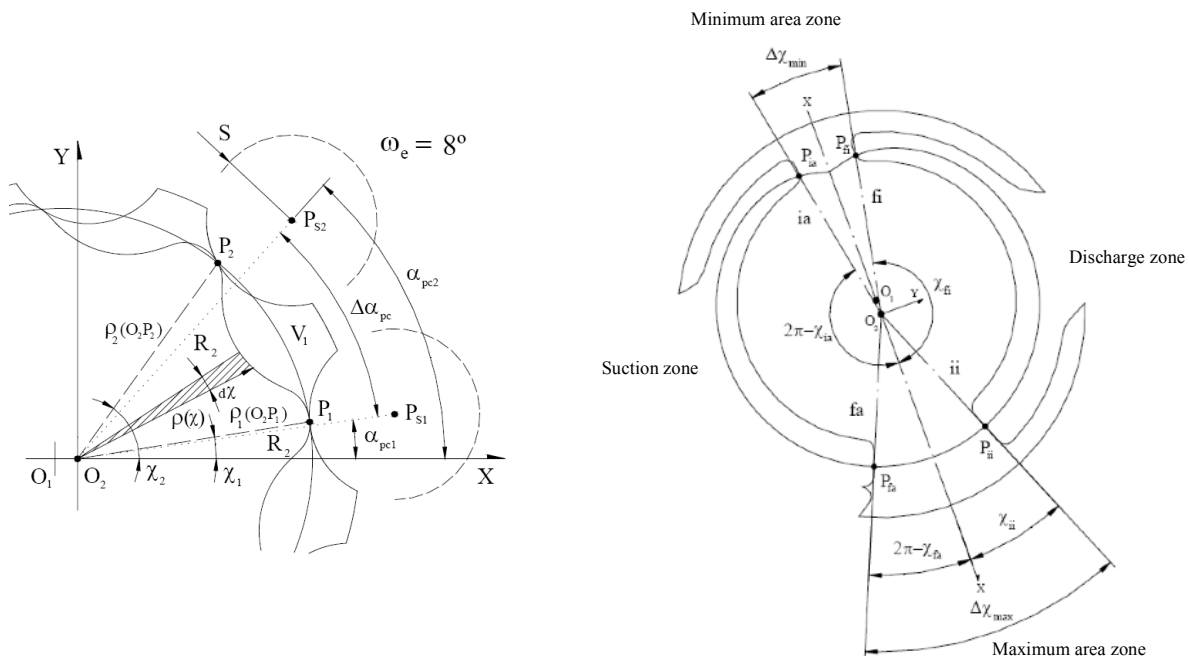


Figure 2.6: Geometrical variables for the port areas calculation.

2.4.3 Studied port area geometries

The original geometry of the gerotor pump is shown in Figure 2.7, where y_{ia} and y_{fi} are 5.9 mm. Different geometries have been simulated, varying some of the parameters related with suction and discharge zones. Groove distances (situated by the minimum area zone) remain constant in this study. Some extra parameters are added, in order to vary the geometry in the fluid circulation boundaries fa and ii . They can be seen in Figure 2.8: the shape of port area grooves changes from the original to the new one, marked in blue. By modifying the groove angles and the variables the different new geometries are obtained.

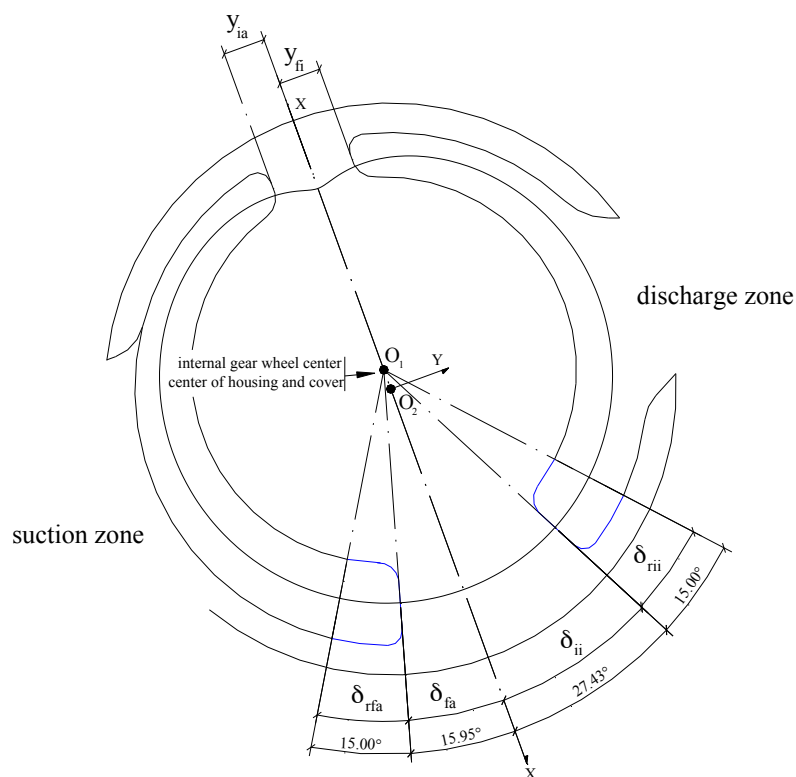


Figure 2.7: Groove angles for the original gerotor pump.

O_1	Center of the internal gear wheel.
O_2	Center of the external gear wheel.
$X-Y$	Absolute reference coordinate system centered in O_2 .
y_{ia}	Groove distance formed by the perpendicular distance between parallel lines of fluid circulation boundary 'ia' centered on O_1 and the X-axis of the absolute reference coordinate system $X-Y$ centered on O_2 .

y_{fi}	Groove distance formed by the perpendicular distance between parallel lines of fluid circulation boundary 'fi' centered on O_1 and the X-axis of the absolute reference coordinate system X-Y centered on O_2 .
δ_{rfa}	Groove angle defined between the fluid circulation boundary 'fa' centered on O_1 and the end of the new groove geometry.
δ_{rii}	Groove angle defined between the fluid circulation boundary 'ii' centered on O_1 and the end of the new groove geometry.
δ_{fa}	Groove angle defined between the fluid circulation boundary 'fa' centered on O_1 and the X-axis of the absolute reference coordinate system X-Y centered on O_2 .
δ_{ii}	Groove angle defined between the fluid circulation boundary 'ii' centered on O_1 and the X-axis of the absolute reference coordinate system X-Y centered on O_2 .

Table 2.2: Variables used for the generation of a new port areas geometry

Table 2.3 shows the characteristics of the 13 different cases that have been studied, and the one that is taken as a reference (case 0). Some of these geometries are represented in Figure 2.10. Note that the groove angles δ_{ii} and δ_{fa} remain constant from case 1 to case 10, while they change in cases 12,13 and 14.

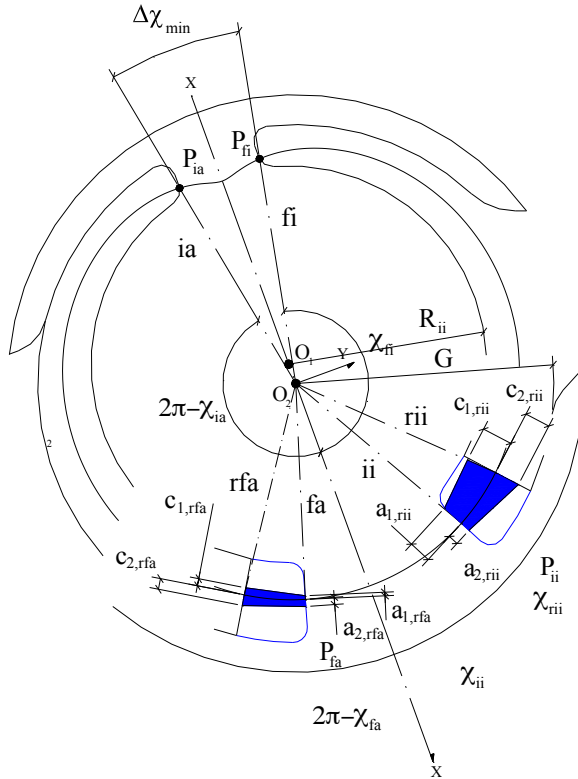


Figure 2.8: Variables used for the generation of a new port areas geometry

	δ_{ii} [deg]	δ_{fa} [deg]	$\delta_{r_{ii}}$ [deg]	$\delta_{r_{fa}}$ [deg]	a1_ii [mm]	a2_ii [mm]	c1_rii [mm]	c2_rii [mm]	a1_fa [mm]	a2_fa [mm]	c1_rfa [mm]	c2_rfa [mm]
Case 0	27.43	15.95	0	0	0	0	0	0	0	0	0	0
Case 1	27.43	15.95	20	20	0	0	2.5	2.5	0	0	2.5	2.5
Case 2	27.43	15.95	15	15	0	0	2.5	2.5	0	0	2.5	2.5
Case 3	27.43	15.95	10	10	0	0	2.5	2.5	0	0	2.5	2.5
Case 4	27.43	15.95	5	5	0	0	2.5	2.5	0	0	2.5	2.5
Case 5	27.43	15.95	15	15	0.6	5.5	0.6	5.5	0.6	5.5	0.6	5.5
Case 6	27.43	15.95	15	15	5.5	0.6	5.5	0.6	5.5	0.6	5.5	0.6
Case 7	27.43	15.95	15	15	1	1	1	1	1	1	1	1
Case 8	27.43	15.95	15	15	0	0	2.5	2.5	0.6	0.6	0.6	0.6
Case 9	27.43	15.95	15	15	0.5	1	1	1.5	0.5	1	1	1.5
Case 10	27.43	15.95	15	15	5.5	5.5	5.5	5.5	5.5	5.5	5.5	5.5
Case 11	22.50	15.95	19.93	15	0	0	2.5	2.5	0	0	2.5	2.5
Case 12	15.00	15.95	27.43	15	0	0	2.5	2.5	0	0	2.5	2.5
Case 13	27.43	10.95	15	20	0	0	2.5	2.5	0	0	2.5	2.5

Table 2.3: Main parameters od the studied geometries. Case 0 corresponds with the original gerotor geometry.

This new *Effective Port Areas Module*, requires some initial geometric parameters that can be seen in Figure 2.11. Some of these parameters, required on the first windows, are also needed in the previous modules of GeroLAB. The effective port area for suction and discharge zones is plotted, as shown in Figure 2.9. The module provides the values of the effective port areas in mm², depending on the angle of rotation of the outer gear in degrees.

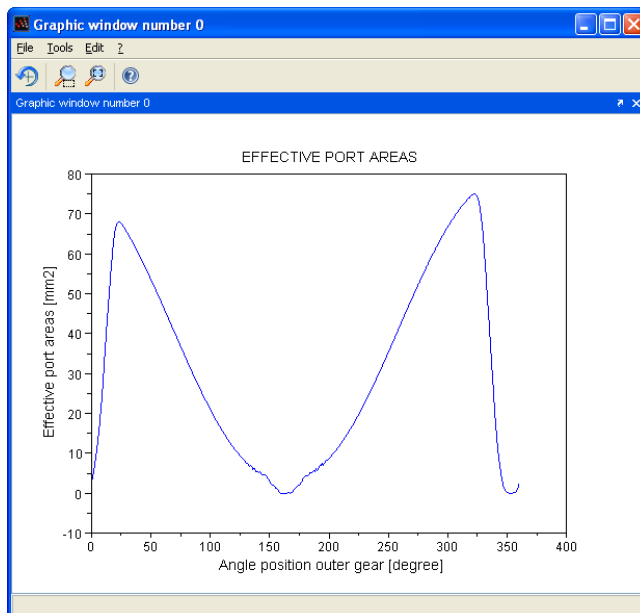


Figure 2.9: Graphic windows of calculated effective port areas

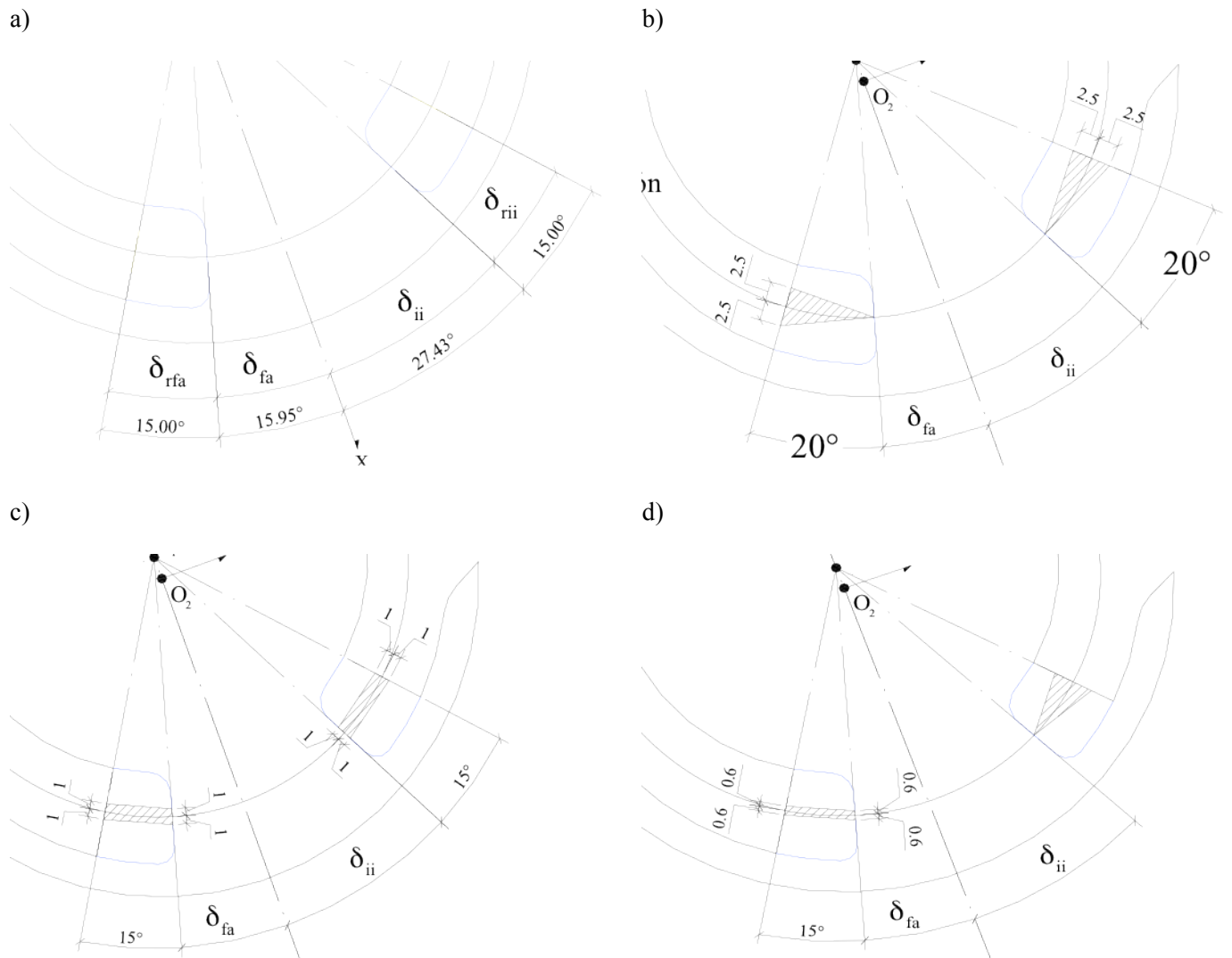


Figure 2.10: Examples of geometry of the port areas. a) Case 0 (original geometry). b) Case 1. c) Case 7. d) Case 8.

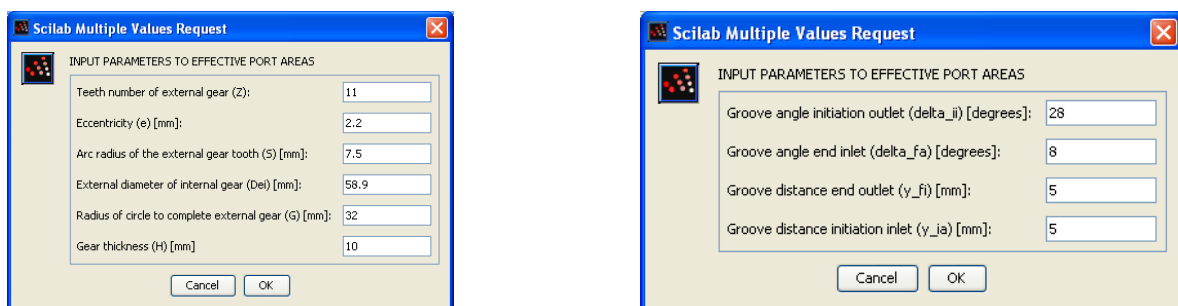


Figure 2.11: Input parameters windows in Effective Port Areas module

2.5 Dynamical Simulation

The present section shows only the final model for the simulation of dynamic performance of the trochoidal gear pump, and describes briefly the main parts of the BondGraph model. A detailed description of the complete model can be found in Gamez-Montero (Gamez-Montero et al., 2007).

The BondGraph simulation model consists of submodels for each of the chambers, interconnected. For each of these chambers, the volume variation is modeled for a full rotation of the outer wheel from the reference position (Figure 2.12). Next step is modeling the interactions of the volume variation of each chamber with the specific fluid zones and de fluid circulation boundaries. To complete the simulation model, the assembly and connection of the submodels of each chamber with each other are created.

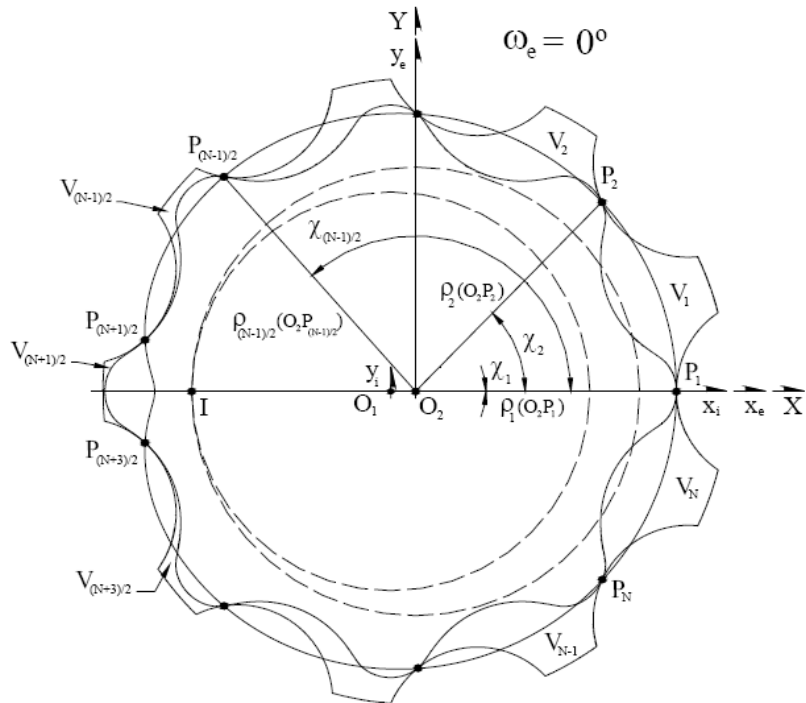


Figure 2.12: Position of reference for the study of volume and its variation

Figure 2.14 shows the complete BondGraph simulation model including the submodels of all chambers of the trochoidal gear pump, while Figure 2.13 describes the simulation submodel of a chamber. As indicated in Figure 2.13, in the different cases that have been studied vary the two functions related with the port areas. Once that the two functions have been calculated using the area GeroLAB module, these results are entered into the BondGraph to simulate the behaviour of the pump and get the flow rate.

To introduce the results of the port area profiles generated by GeroLAB, they have to be approximated by two piecewise functions: one for the discharge area and the other for the suction area. This step should be done in order to reduce the calculation time in BondGraph: if this data is directly introduced in the simulation (using a ‘.txt’ file) it takes much more time to calculate the flow rate.

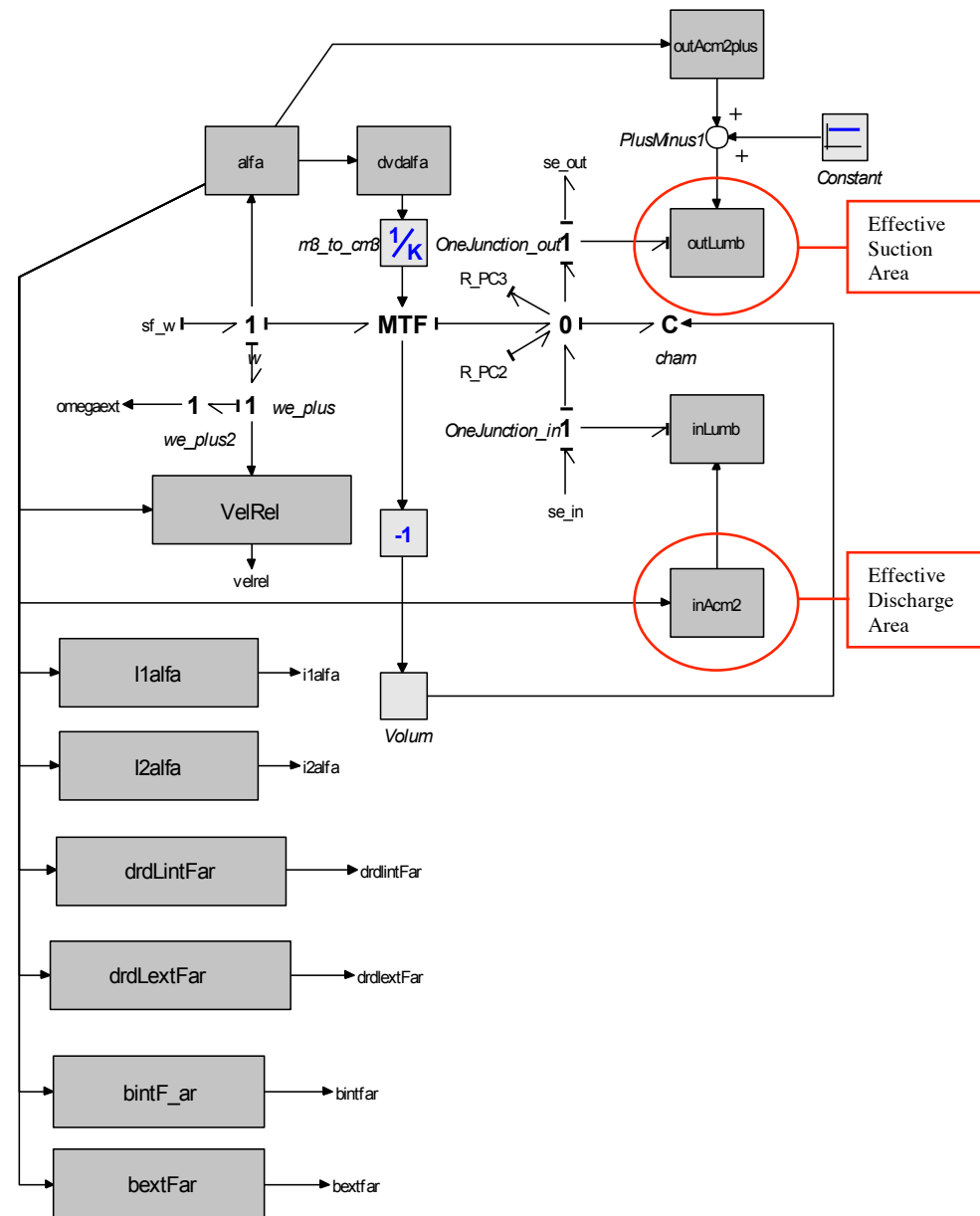


Figure 2.13: Submodel for the BondGraph simulation of a chamber

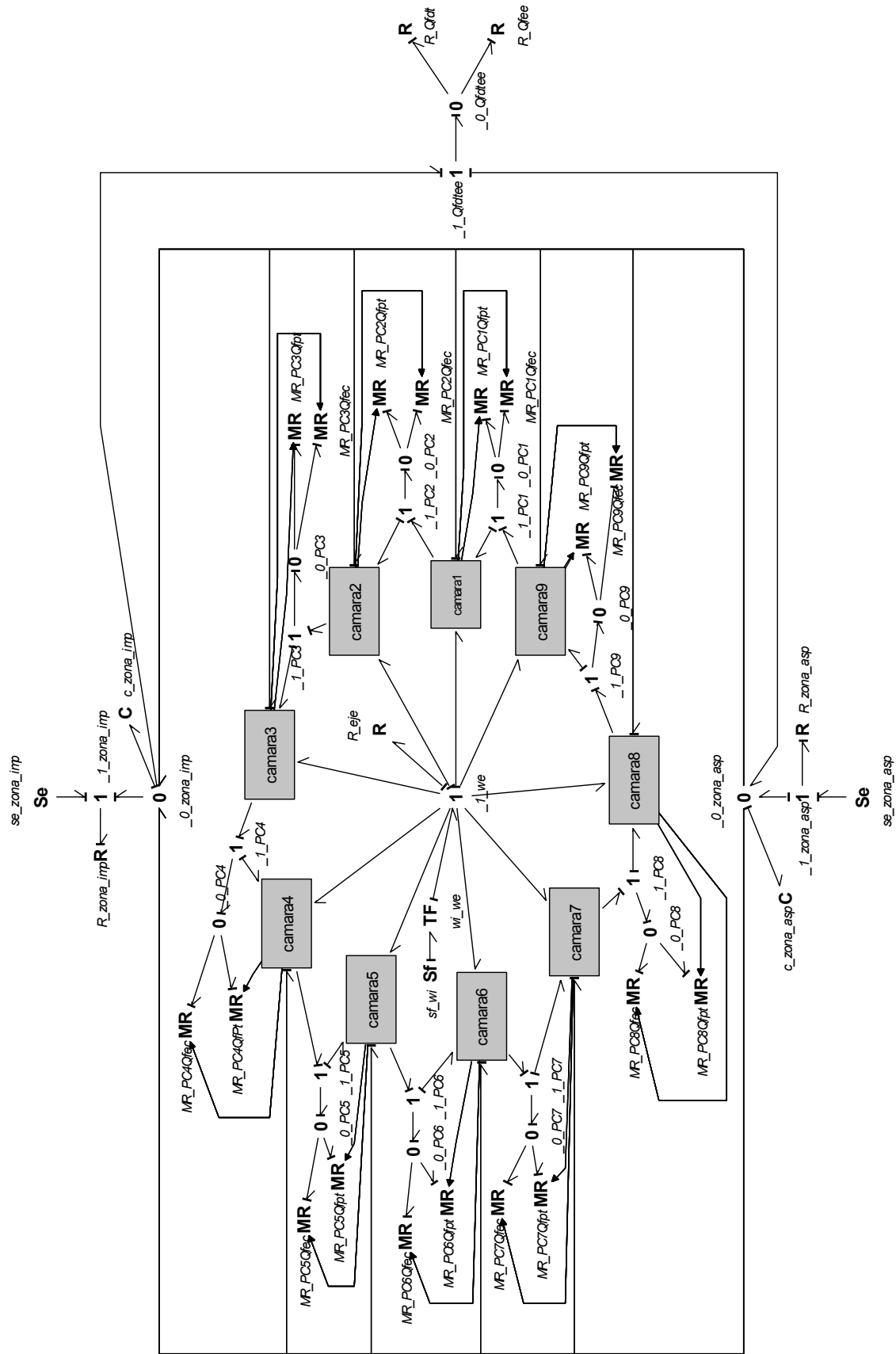


Figure 2.14: Complete BondGraph simulation model for the trochoidal gear pump

2.6 Results of the Dynamical Simulation

This section summarizes the most relevant results that have been achieved through BondGraph simulations and thanks to the created module for GeroLAB, *Effective Port Areas*.

The effective port areas are calculated by the GeroLAB new module for each one of the simulated geometries. Figure 2.15 shows how discharge and suction areas are distributed for a complete rotation of the gearing, where the rotation angle of the external gear is plotted in the horizontal axis. This graph shows the evolution of the areas for each chamber between two teeth. When used in the BondGraph simulation, this profile is entered in each chamber's submodel.

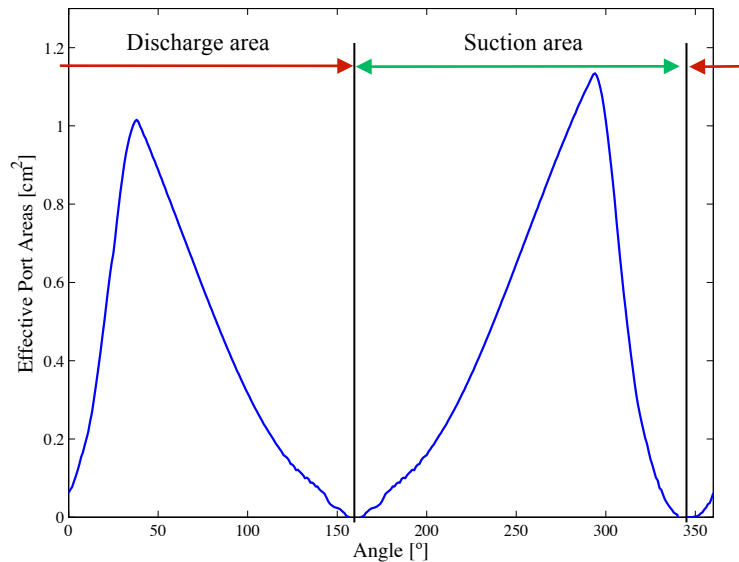


Figure 2.15: Discharge and suction effective port areas for a whole rotation.

Figure 2.16 shows the effective port area calculated for geometries from 1 to 4. Note that the only differences between geometry from cases 1 to 4 are the angles δ_{rfa} and δ_{rii} , as these variables decrease its value in 5° from case to case. As can be seen, this reduction of angle produces a displacement of the maximum value in the effective port areas and also an increase in the maximum values of discharge and suction areas. As shown in Figure 2.17 this change in the port areas makes no significant difference between the flow ripple of these four cases.

Although at first sight it may seem that there is no significant difference between the effective port areas of case 2 and 13 due to the change of δ_{rfa} , Figure 2.19 shows the detail of the zone where areas are different. This slight change in the area produces a deviation in the first local minimum value of the flow ripple, as shown in Figure 2.20.

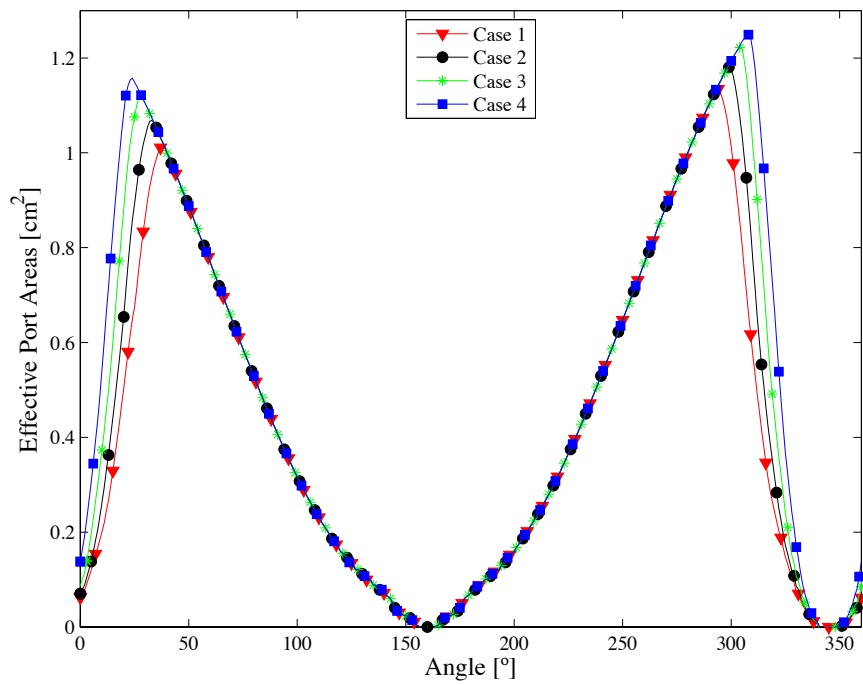


Figure 2.16: Effective port areas for cases 1, 2, 3 and 4.

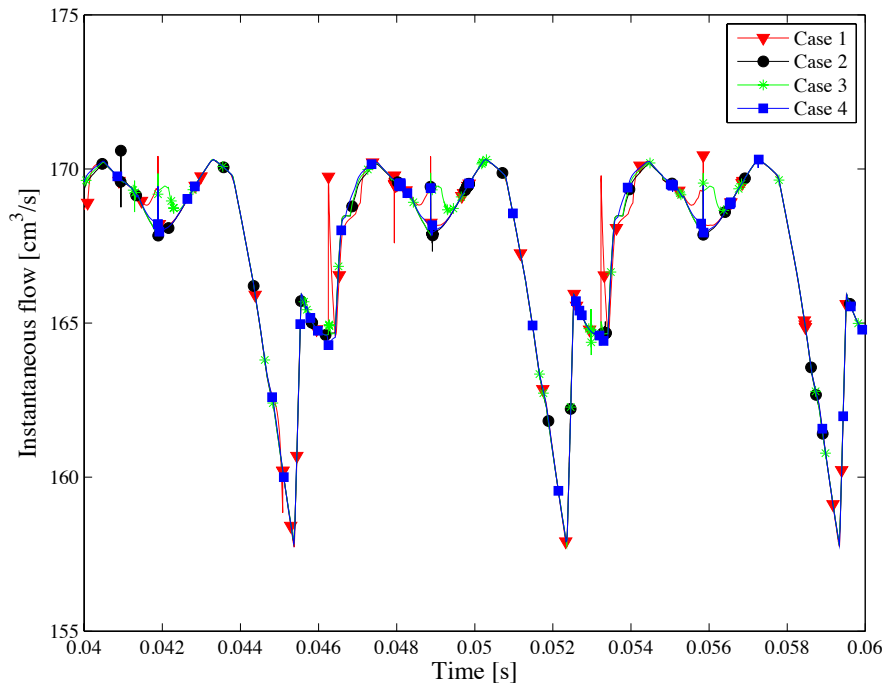


Figure 2.17: BondGraph flow ripple for cases 1, 2, 3 and 4.

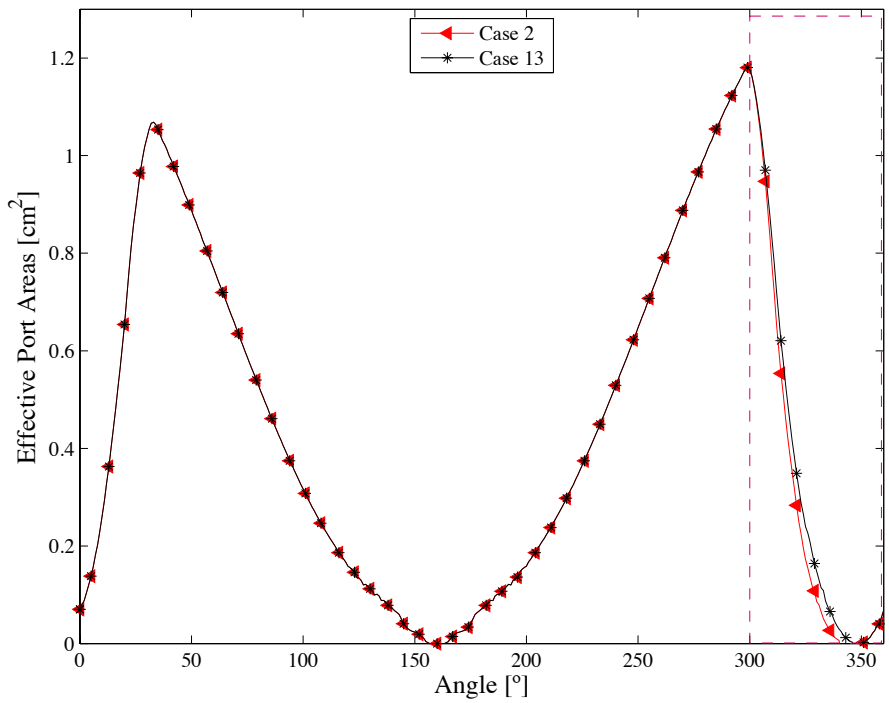


Figure 2.18: Effective port areas for cases 2 and 13.

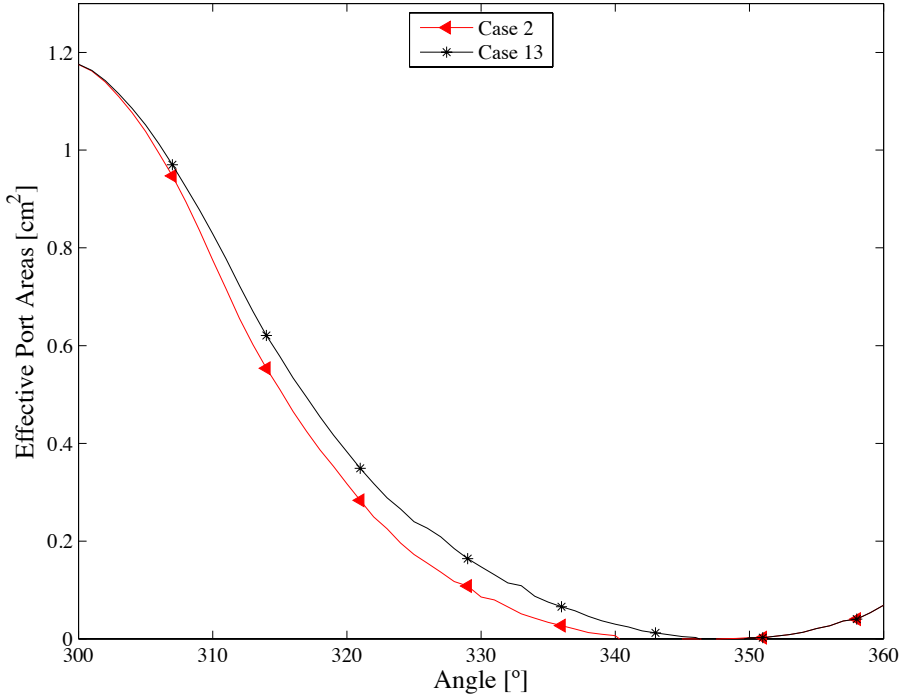


Figure 2.19: Detail of the effective port areas for cases 2 and 13.

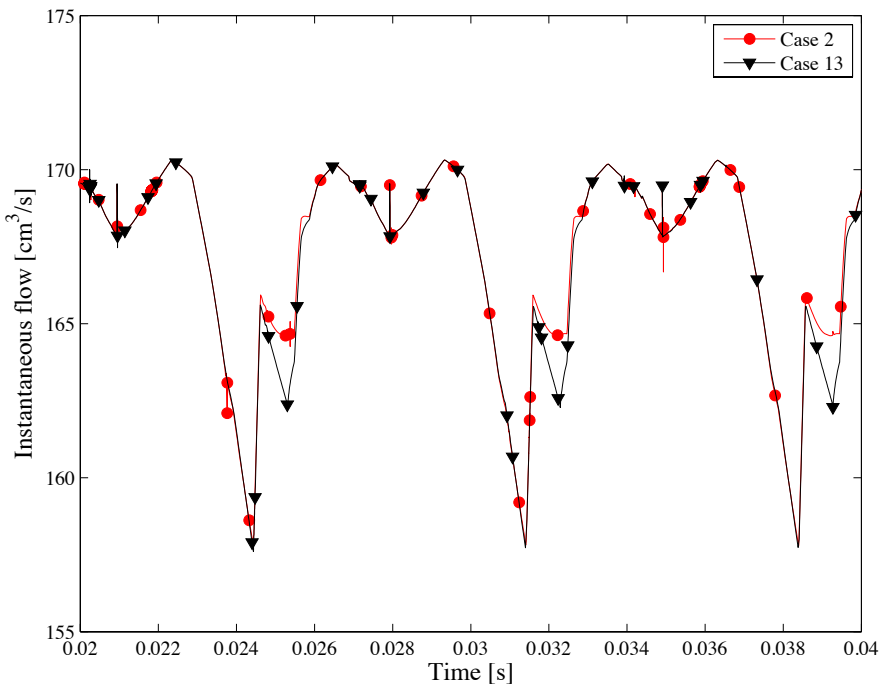


Figure 2.20: BondGraph flow ripple for cases 2 and 13.

	Irregularity flow index [%]	Relative irregularity flow index [%]
Case 0	8.5	0.0
Case 1	7.6	-10.6
Case 2	7.6	-10.6
Case 3	7.5	-11.8
Case 4	7.5	-11.8
Case 5	9.5	11.8
Case 6	9.9	16.5
Case 7	7.9	-7.1
Case 8	7.6	-10.6
Case 9	9.5	11.8
Case 10	8.4	-1.2
Case 11	8.5	0.0
Case 12	10.3	21.2
Case 13	7.6	-10.6

Table 2.4: Irregularity flow indices for the simulated geometries

In order to characterize the behaviour of the simulated cases, referring to the instant flow, some relations between local maximums and minimums are used. On the one hand, the irregularity flow index

is defined, as the difference between the maximum and minimum values of the flow ripple, related to its average value. On the other hand, this irregularity index is expressed relative to its value at the reference pump (case 0). The results are shown in Table 2.4. As can be seen, some of the studied modifications in the port areas produce a significant quantitative reduction of the irregularity flow index that can be almost about 12%.

2.7 Conclusions of the Analytical Approach

The present chapter presents two new modules for GeroLAB Package that have been programmed, thus providing a new tool for the calculation of the minimum clearance history between trochoidal profiles and the effective port areas in the gerotor pump.

Following, the dynamical response of the pump is studied, for a set of 13 different geometries, and results of the instantaneous flow in the outlet pipe are presented. On the one hand, the variation of the effective port areas is calculated for each geometry thanks to the *Effective Port Areas Module* of GeroLAB package. On the other hand, the dynamical simulation of the flow ripple has been carried out for all the studied cases through a BondGraph model including the aforementioned calculated areas, making it more realistic.

Despite the fact that at first sight it may seem that there are no significant differences between the different studied cases, we must highlight the importance of studying the port areas influence: it has been observed that little variations in the port areas produce important differences in the flow ripple of the pump. And that leads us to focus the future study on the parameters which produce reductions in the irregularity of the flow, in order to achieve the optimum geometry for the port areas. Thanks to these results, it is possible to establish constructive relations between the differences in design and the response provided by the pump flow. Moreover, for the studied geometries in the present work, it has been seen that some of them produce a significant quantitative reduction of the irregularity flow index that can be almost about 12% (see Table 2.4).

As a final remark, the limitations of the BondGraph dynamical model have to be considered. Some constants representing fluid-dynamic parameters are estimated, or are experimentally adjusted. One example of these constants would be the discharge coefficient that is used to characterize the leakage flow between trochoidal profiles, which is estimated as an average value of this coefficient for a similar geometry.

According to the preceding limitations, it seems to be necessary to implement a methodology complementary to the BondGraph technique, in order to calculate the fluid-dynamic parameters that are used in the dynamical simulation. The aforesaid complementary methodology proposed in this thesis is

Computational Fluid Dynamics (CFD). Nowadays, CFD is a very useful tool to provide details of the fluid-dynamic behaviour on the insights of hydraulics machinery. It is a fact that CFD is present in most mechanical designs of hydraulic machines, as it can provide details of the flow and pressure fields in the inside of the hydraulic machines. Next chapter presents the numerical simulation models that would accomplish the function of complementing the dynamical simulation, thus making it more accurate.

3 Numerical Simulation

3.1 Introduction to the Numerical Simulation

As seen in previous chapter, the BondGraph dynamical model has to be complemented with fluid-dynamic parameters, in order to make the model more accurate. And it is a fact that nowadays Computational Fluid Dynamics (CFD) is present in most mechanical designs of hydraulic machines.

As seen in Chapter 1, one aspect that is not already resolved is the leakage model that properly describes the real behaviour of the pump. Motivated by this fact, the CFD three-dimensional model is planned to accomplish this objective of clarifying how leakage flow affects the response of the pump. As a consequence, the model includes tolerances between the different pieces that integrate the gerotor pump, so the fluid-dynamic characteristics of its behaviour can be properly analysed.

For all the aforementioned reasons and according to the author's knowledge, numerical simulation by means of CFD is the suitable tool that can give details about the fluid-dynamic behaviour of the gerotor pump, thus complementing the dynamical simulation model through BondGraph and allowing the analysis of the leakage effects in the overall behaviour of the pump.

The present chapter introduces the proposed CFD model for the gerotor pump. Because the instantaneous flow is rather dependent on the teeth contact, a new boundary condition of a virtual wall has been developed, which allows simulation of the teeth contact in the interteeth radial clearances. This new boundary condition is utilized in a three-dimensional model of the gerotor pump with mesh deformation and remeshing at every time step by means of a home-made ad-hoc code named *gearing contact point*.

The CFD simulations have been performed with the commercial code ANSYS FLUENT™ 12.0.16, which is based on the finite-volume method. The 3D modelling of the pump and its meshing have been done with the GAMBIT software package, that is a meshing software of FLUENT.

In the following the theory and considerations related to the numerical simulations are described, in addition to the selected numerical schemes and turbulence model. The mesh zones are described,

including the details of the mesh deformation algorithm and its quality, and the grid independence study. Special attention is paid to the *Gearing Contact Point* strategy, which reduces significantly the computational cost of the simulations.

3.2 Numerical schemes

With the Finite-Volume Method (FVM), the balance equation of each physical magnitude is solved in each discrete volume using an integral formulation. With respect to dynamic meshes, the integral form of the conservation equation for a general scalar ϕ , on an arbitrary control volume V , whose boundary is moving, can be written as

$$\frac{d}{dt} \int_V \rho \phi dV + \int_{\partial V} \rho \phi (\vec{u} - \vec{u}_g) \cdot d\vec{A} = \int_{\partial V} \Gamma \nabla \phi \cdot d\vec{A} + \int_V S_\phi dV \quad (3.1)$$

where ρ is the fluid density

\vec{u} is the flow velocity vector

\vec{u}_g is the mesh velocity of the moving mesh

Γ is the diffusion coefficient

S_ϕ is the source term of ϕ

∂V is used to represent the boundary control of the control volume V

The time derivative term in equation (3.1) is calculated with a first-order implicit scheme, since this is the only method that our software allows with dynamic mesh. It can be written as

$$\frac{d}{dt} \int_V \rho \phi dV = \frac{(\rho \phi V)^{n+1} - (\rho \phi V)^n}{\Delta t} \quad (3.2)$$

where n and $n + 1$ denote the respective quantity at the current and next time level. The $(n + 1)^{th}$ time level volume V^{n+1} is computed from

$$V^{n+1} = V^n + \frac{dV}{dt} \Delta t \quad (3.3)$$

where dV/dt is the volume time derivate of the control volume. In order to satisfy the mesh conservation law, the volume time derivation of the control volume is computed from

$$\frac{dV}{dt} = \int_{\partial V} \vec{u}_g \cdot d\vec{A} = \sum_j^{n_f} \vec{u}_{gj} \cdot \vec{A}_j \quad (3.4)$$

where n_f is the number of faces on the control volume ($n_f = 6$ in hexahedral structured meshes and $n_f = 5$ in triangular prism unstructured meshes) and \vec{A}_j is the j face area vector. The dot product $\vec{u}_{gj} \cdot \vec{A}_j$ on each control volume is calculated from

$$\vec{u}_{gj} \cdot \vec{A}_j = \frac{\delta V_j}{\Delta t} \quad (3.5)$$

where δV_j is the volume swept out by the control volume face j over the time step Δt .

In the continuity equation, with $\phi = 1$ (and both diffusive and source terms are null), a second order upwind scheme has been chosen in order to discretize the convective term. For triangular and hexahedral grids (used in the present study), since the flow is never aligned with the grid, the second order discretization generally gives more accurate results than lower order schemes.

To solve the equations, a pressure-based coupled scheme is needed. From the available algorithms, the Pressure-Implicit with Splitting of Operators (PISO) pressure-velocity coupling scheme is chosen, as it is highly recommended in the software documentation for transient calculations on skewed meshes. PISO is a variation of the semi-implicit method for pressure-linked equations (SIMPLE) algorithm, in which the calculations are moved inside the solution stage of the pressure correction equation and then the pressure correction gradients are recalculated and used to correct the mass flux.

The default coupling between neighbor and skewness corrections has been disabled, as it is more expensive in computational terms, and it is recommended for meshes with a high degree of skewness (not in the present case, more details are given in *Mesh properties* in the present chapter).

When using PISO neighbor correction, under-relaxation factors of 1.0 or near 1.0 are recommended for all equations, as indicated in the software's user manual. For most problems, it is not necessary to disable the default coupling between neighbor and skewness corrections.

The momentum equations for each velocity component can be derived from the general transport equation (3.1) by replacing the variable ϕ by u , v and w respectively. Every velocity component appears in each momentum equation, and the velocity field must also satisfy the continuity equation.

Regarding to the spatial discretization, from the available methods to compute the gradients in ANSYS FLUENT the Least Squares Cell-Based method has been chosen as on irregular (skewed and distorted) unstructured meshes, the accuracy of the least squares gradient method is comparable to that of the node-based gradient (and both are much more superior compared to the cell-based gradient). However, it is less expensive to compute the least-squares gradient than the node-based gradient.

The spatial discretization of the momentum equations ($\phi = u$, $\phi = v$ and $\phi = w$) follows a high order QUICK scheme, which is based on a weighted average of second-order-upwind and central

interpolations of the variable. This scheme allows the calculation for a higher precision in the regions with structured mesh and becomes identical to the second order upwind scheme in the rest of the computational domain.

Furthermore, to discretize momentum equation, pressure values are needed on the control volume faces. Standard pressure discretization interpolates the pressure on the faces using the cell center values. On the other hand the pressure-staggered option PRESTO discretization for pressure actually calculates pressure on the face. This is possible using staggered grids where velocity and pressure variables are not "co-located". Figure 3.1 presents an example of unstructured staggered grid: pressure is defined in the center of faces of cells (represented as points) and velocities are assigned in faces and perpendicular to the them (for the coloured cell, see the lines representing velocities).

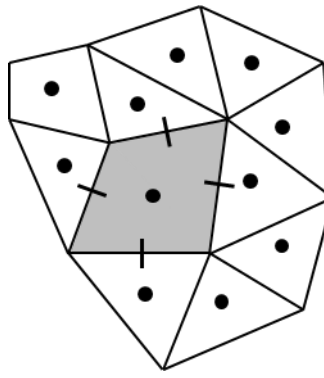


Figure 3.1: Example of an unstructured staggered grid.

PRESTO discretization gives more accurate results since interpolation errors and pressure gradient assumptions on boundaries are avoided. Although PRESTO is more computationally costly, the pressure-staggered option was chosen since it has been reported to give better results for high pressure and velocity gradients.

3.3 Turbulence modelling

Turbulent flows are characterized by fluctuating velocity fields, causing a fluctuation also in the transport equations. Since these fluctuations are too computationally expensive to simulate directly in most engineering calculations, the instantaneous governing equations can be time-averaged, ensemble-averaged, or otherwise manipulated to remove the resolution of small scales. Thus, the resulting set of equations is computationally less expensive to solve. However, the modified equations contain additional unknown variables, and turbulence models are needed to determine these variables in terms of known quantities.

In turbulence models for Reynolds-averaged Navier–Stokes (RANS) the attention is focused on the mean flow and the effects of turbulence on mean flow properties. Prior to the application of numerical methods the Navier–Stokes equations are time averaged (or ensemble averaged in flows with time-dependent boundary conditions). Extra terms appear in the time-averaged (or Reynolds- averaged) flow equations due to the interactions between various turbulent fluctuations. These extra terms are modelled with classical turbulence models: among the best known ones are the $k-\varepsilon$ model and the Reynolds stress model. The computing resources required for reasonably accurate flow computations are modest, so this approach has been the mainstay of engineering flow calculations over the last three decades (Versteeg et al., 2007).

The choice of turbulent model depends on considerations such as the physics comprised in the type of flow, the level of accuracy required and the available computational resources, and the amount of time available for the simulation. The simplest complete models of turbulence are the two-equation models in which the solution of two separate transport equation allows the turbulent velocity and length scales to be independently determined. From the available two-equation models in ANSYS FLUENT, the standard $k-\varepsilon$ has been chosen. Its main advantages are that it's the simplest turbulence model for which only initial and boundary conditions need to be supplied, it has an excellent performance for many industrially relevant flows and it's the most widely validated turbulence model.

The standard $k-\varepsilon$ is a semi-empirical model based on model transport equations for the turbulent kinetic energy (k) and its dissipation rate (ε), that are obtained from the following transport equations (3.6) and (3.7):

$$\frac{\partial}{\partial t}(\rho k) + \frac{\partial}{\partial x_i}(\rho k u_i) = \frac{\partial}{\partial x_j} \left[\left(\mu + \frac{\mu_t}{\sigma_k} \right) \frac{\partial k}{\partial x_j} \right] + G_k + G_b - \rho \varepsilon - Y_M + S_k \quad (3.6)$$

$$\frac{\partial}{\partial t}(\rho \varepsilon) + \frac{\partial}{\partial x_i}(\rho \varepsilon u_i) = \frac{\partial}{\partial x_j} \left[\left(\mu + \frac{\mu_t}{\sigma_\varepsilon} \right) \frac{\partial \varepsilon}{\partial x_j} \right] + C_{1\varepsilon} \frac{\varepsilon}{k} (G_k + C_{3\varepsilon} G_b) - C_{2\varepsilon} \rho \frac{\varepsilon^2}{k} + S_\varepsilon \quad (3.7)$$

where G_k represents the generation of turbulence kinetic energy due to the mean velocity gradients, and G_b is the generation of turbulent kinetic energy due to buoyancy (insignificant in the present study), Y_M represents the contribution of the fluctuating dilatation in compressible turbulence to the overall dissipation rate. $C_{1\varepsilon}$, $C_{2\varepsilon}$ and $C_{3\varepsilon}$ are constants, and σ_k and σ_ε are the turbulent Prandtl numbers for k and ε , respectively. S_k and S_ε are user-defined source terms (not considered in the present simulations).

G_k can be evaluated in a manner consistent with the Boussinesq hypothesis as in (3.9), as follows:

$$G_k = -\rho \overline{u'_i u'_j} \frac{\partial u_j}{\partial x_i} \quad (3.8)$$

$$G_k = \mu_t S^2 \quad (3.9)$$

where S is the modulus of the mean rate-of-strain tensor, and it is defined in (3.10), being the strain rate tensor S_{ij} defined in (3.11):

$$S \equiv \sqrt{2S_{ij}S_{ij}} \quad (3.10)$$

$$S_{ij} = \frac{1}{2} \left(\frac{\partial u_i}{\partial x_j} + \frac{\partial u_j}{\partial x_i} \right) \quad (3.11)$$

The turbulent viscosity μ_t is computed as follows:

$$\mu_t = \rho C_\mu \frac{k^2}{\varepsilon} \quad (3.12)$$

where C_μ is a constant, with a value of 0.09 for the standard k - ε model.

The model constants and the turbulent Prandtl numbers have been used as its default values. These default values have been determined from experiments with air and water for fundamental shear flows including homogeneous shear flows and decaying isotropic grid turbulence. They have been found to work fairly well for a wide range of wall-bounded and free shear flows, as indicated by Versteeg (Versteeg, 2007) and in the software's manual. These default values are:

$$C_{1\varepsilon} = 1.44, C_{2\varepsilon} = 1.92, \sigma_k = 1.0, \sigma_\varepsilon = 1.$$

3.4 Convergence criteria

The numerical solution of a flow problem requires an iterative process. The final solution exactly satisfies the discretized flow equations in the interior of the domain and the specified conditions on its boundaries. If the iteration sequence is convergent the difference between the final solution of the coupled set of discretized flow equations and the current solution after k iterations reduces as the number of iterations increases. In practice, the available resources of computing power and time dictate that the iteration sequence is truncated when the solution is sufficiently close to the final solution.

The convergence test in the iterative sequences involves specification of tolerances for the normalized global residuals for mass, momentum and energy. An iteration sequence is automatically truncated when all these residuals are smaller than their pre-set maximum value.

There are several different ways of constructing practically useful truncation criteria in CFD, but by far the most common one is based on so-called residuals. After discretization, the conservation equation for a general variable ϕ at a cell P can be written as

$$a_P \phi_P = \sum_{nb} a_{nb} \phi_{nb} + b \quad (3.13)$$

where a_P is the center coefficient, a_{nb} are the influence coefficients for the neighboring cells, and b is the contribution of the constant part of the source term in $S = S_C + S_{P\phi}$ and of the boundary conditions. The residual R^ϕ computed by ANSYS FLUENT's pressure-based solver is the imbalance in equation (3.13) summed over all the computational cells P . This is referred to as the scaled residual, and it can be written as

$$R^\phi = \sum_{cells P} \left| \sum_{nb} a_{nb} \phi_{nb} + b - a_P \phi_P \right| \quad (3.14)$$

In general, it is difficult to judge convergence by examining the residuals defined by equation (3.14) since no scaling is employed. ANSYS FLUENT scales the residual using a scaling factor representative of the flow rate of ϕ through the domain. This scaled residual is defined as

$$R^\phi = \frac{\sum_{cells P} |\sum_{nb} a_{nb} \phi_{nb} + b - a_P \phi_P|}{\sum_{cells P} |a_P \phi_P|} \quad (3.15)$$

The scaled residuals described above are useful indicators of solution convergence, as indicated by the software documentation. In our case, the simulation will be considered converged when the scaled residuals of each equation drop below 10^{-3} in all time steps of the gearing cycle.

3.5 Simulation of the tooth contact in the interteeth clearance

In order to model the manufacturing tolerance between the inner and outer gears, the internal diameter of the outer gear is increased and, as a consequence, the two trochoidal profiles do not share any contact point.

The solid contact point between trochoidal gears has been simulated using a leakage model based on the strategy developed in Gamez-Montero (Gamez-Montero et al., 2011), named *viscous wall cell*. The strategy involves, first, finding the Z interteeth radial clearances with the minimum size. For every time step, the wall cell that corresponds to the minimum distance between each pair of inner-outer gear teeth is searched through the mesh located at each interteeth radial clearance. Once it is located, it is labelled the *contact wall cell*. Finally, the model enforces a high viscosity to each contact wall cell and, as a result, a

virtual wall is created as a solid-solid boundary condition. To avoid numerical problems related to strong gradients, the cells within a small area around this position (within a radius d_{max}) are also identified and a linear distribution of the viscosity is imposed in these cells, with the objective of gradually return the viscosity to its normal value, μ_{oil} . This linear distribution is as follows

$$\mu_c = \mu_{max} - \frac{\mu_{max} - \mu_{oil}}{d_{max}} d \quad (3.16)$$

where μ_c is the viscosity in a cell marked as *contact wall cell*, μ_{max} is the high value of viscosity used to simulate the solid-solid boundary condition, μ_{oil} is the normal viscosity of the fluid, d_{max} is the radius of the zones containing the marked cells and d is the distance between a marked cell's centroid and the theoretical contact point.

This boundary condition is applied at every time step by means of a home-made ad-hoc code programmed in C++. The algorithm of the code is integrated in the CFD solver as a user-defined function (UDF) which is not included in the ANSYS FLUENT standard version. The viscous wall-cell strategy is shown in Figure 3.2.

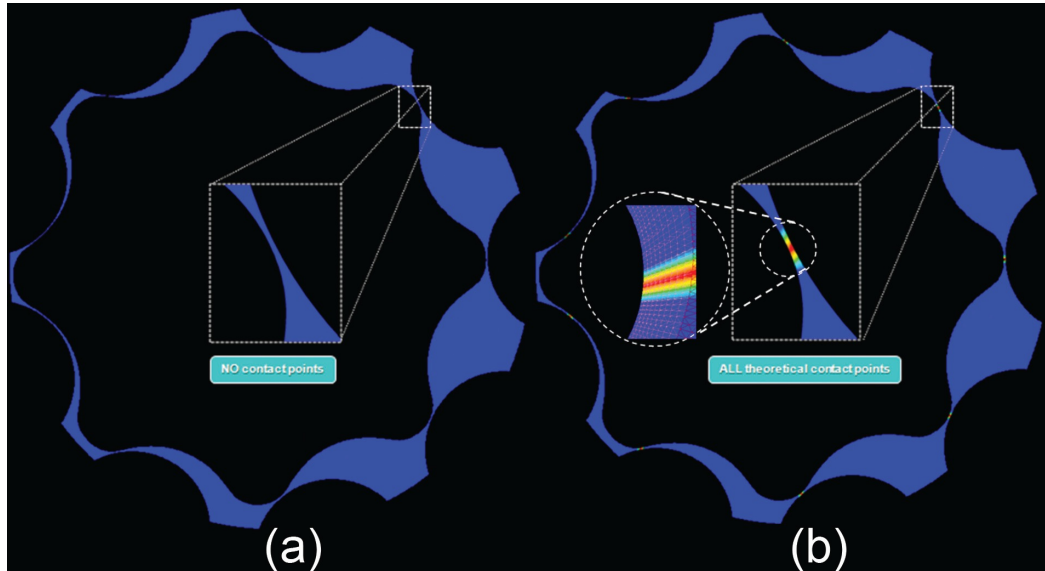


Figure 3.2: Teeth contact simulation by using the viscous wall-cell strategy: (a) Z interteeth clearances and no contact points; (b) 3D Z contact points and no interteeth clearances.

In the present work, this UDF used to calculate the contact points has been improved, in terms of calculation efficiency. A new strategy has been created, named *gearing contact point*. The main contribution has been the inclusion of the theoretical calculation of the contact points before searching in the domain of the fluid. The analytical coordinates of the contact points are calculated, for each angle of rotation of the gearing, which allow the calculation of the analytical contact angle, at each time step. By

including this modification, the UDF reduces the number of cells in which it searches for the contact points, as it has been introduced a restriction in the domain that forces the simulation to search only in the nearby cells corresponding to the coordinates of the contact point.

This means that the function is only searching in the faces around the theoretical contact point. It can search as close to the theoretical contact point as we define in the code, by means of an angular tolerance ($\pm\delta\alpha$) included in the algorithm. The only condition that has to be considered to define $\delta\alpha$ is that it has to be able to contain the minimum number of cells where we want to impose the linear distribution of viscosity.

Another improvement introduced thanks to the *gearing contact point* strategy is that it is no necessary searching in all the faces of outer and inner profiles, so reducing strongly the calculation time of the simulations. Once that a cell of the outer profile is located inside the neighbouring of the theoretical contact point it is labelled as *contact wall cell*. Finally, of all these marked cells, the model enforces a high viscosity to each contact wall cell and, as a result, a virtual wall is created as a solid-solid boundary condition.

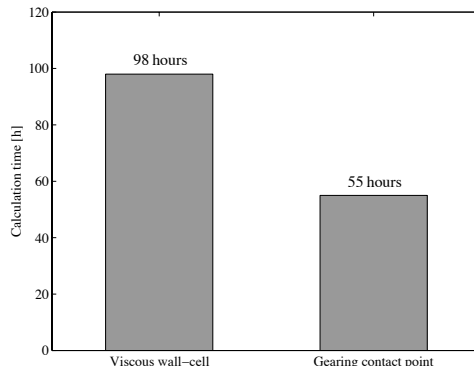


Figure 3.3: Calculation time of the two contact point strategies

The pseudo-code of the original algorithm and the modified one are presented in Figure 3.4. The comparative between the time of calculation of the original strategy *viscous wall cell*, and the improved methodology *gearing contact point* can be seen in Figure 3.3. The represented time (expressed in hours) corresponds to a calculation of a laminar case, with a time step of $3 \cdot 10^{-5}s$, performed with an Intel® Pentium® Dual CPU E2200 @ 2.20GHz x 2 with a RAM memory of 1.9 GiB. As it can be seen, the reduction of calculation time is about the 40% comparing *gearing contact point* and *viscous wall-cell* strategies.

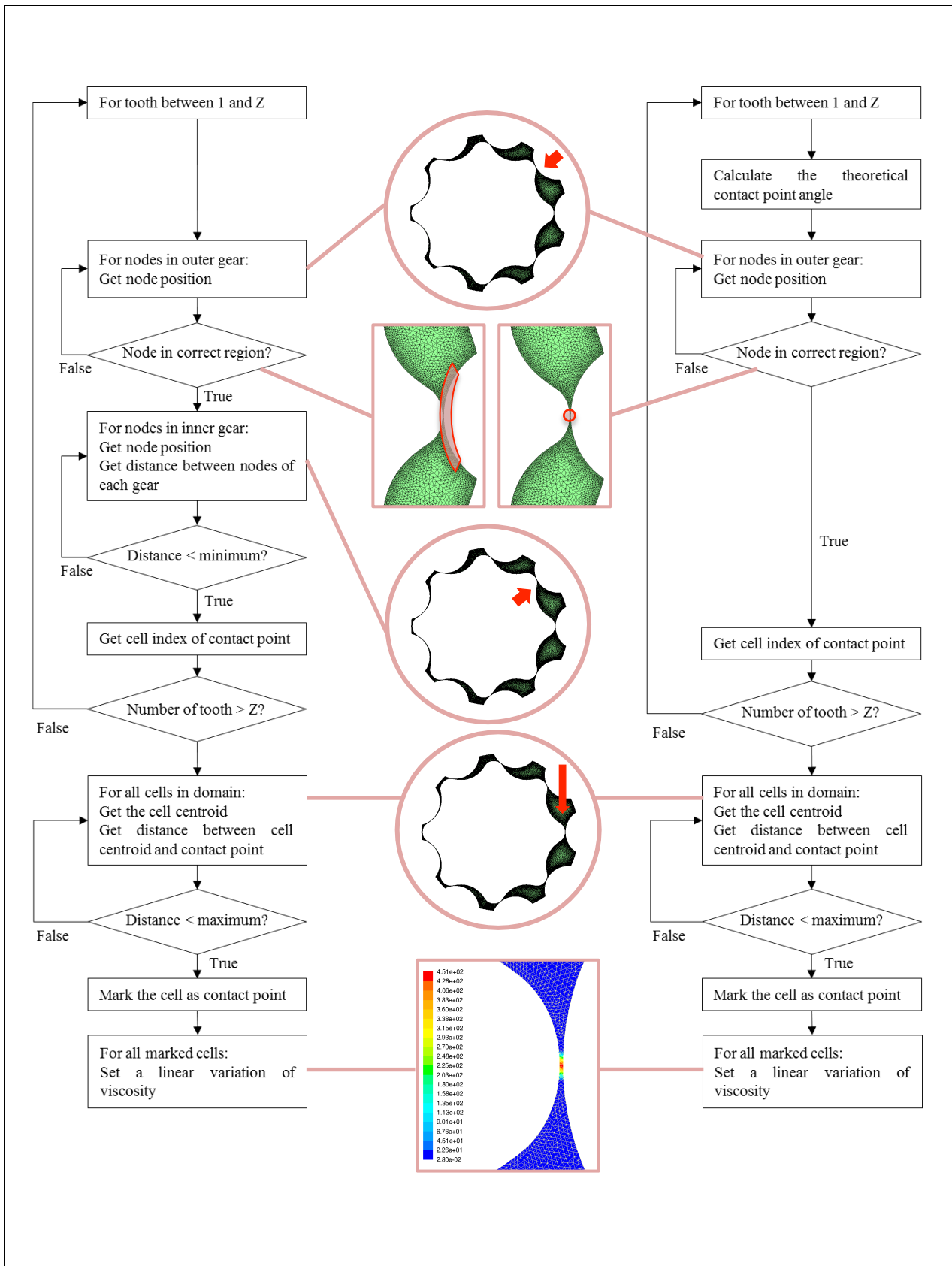


Figure 3.4: Pseudo-code of the viscous wall-cell strategy (left) and gearing contact point strategy (right)

3.6 Mesh properties

3.6.1 Mesh zones

The computational domain of the fluid is divided into three main zones: port areas zone, gearing zone and base zone. A general view the domain can be seen in Figure 3.5: for a more clear visualization of the whole domain, only the outlines have been drawn, and the cells of these zones are not shown. As all of this zones are extrudable geometries, the 2.5D meshing technique is used, which is essentially an extrusion of a 2D mesh along the normal axis of the dynamic zone. This technique requires less time than regular volumetric meshing for the equivalent volume.

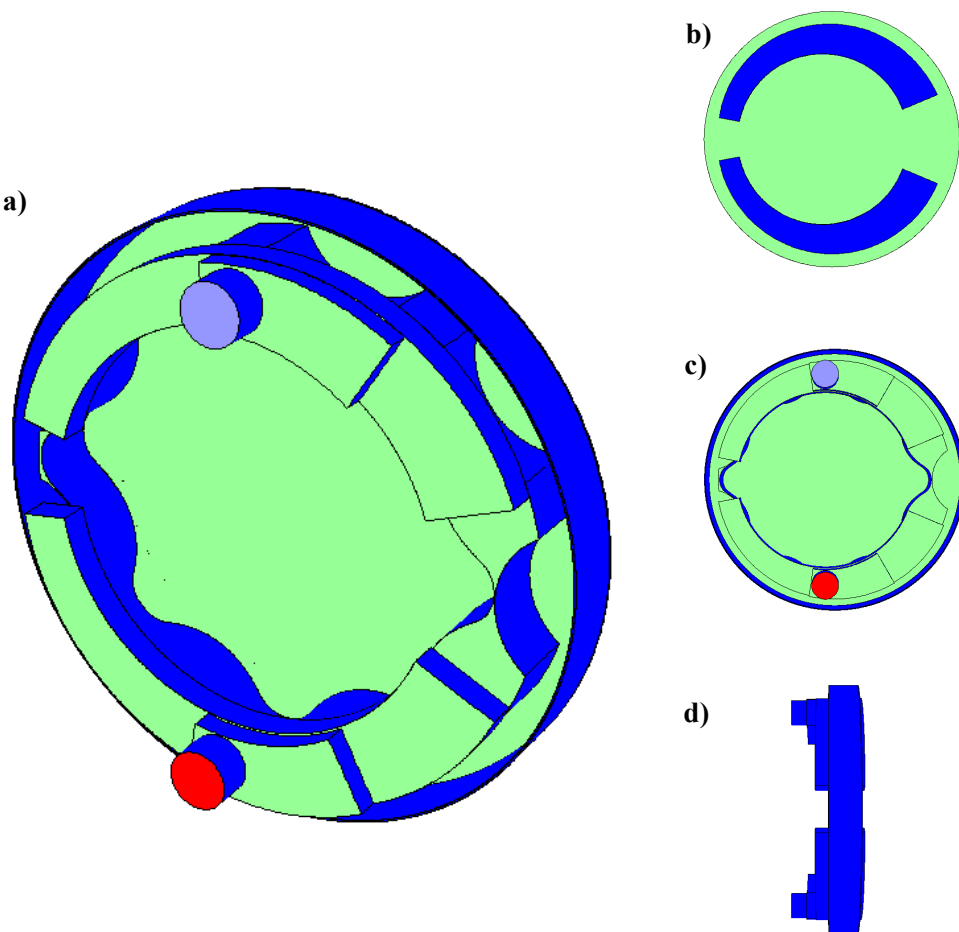


Figure 3.5: Computational domain zones: a) Isometric, b) Back, c) Front and d) Left.

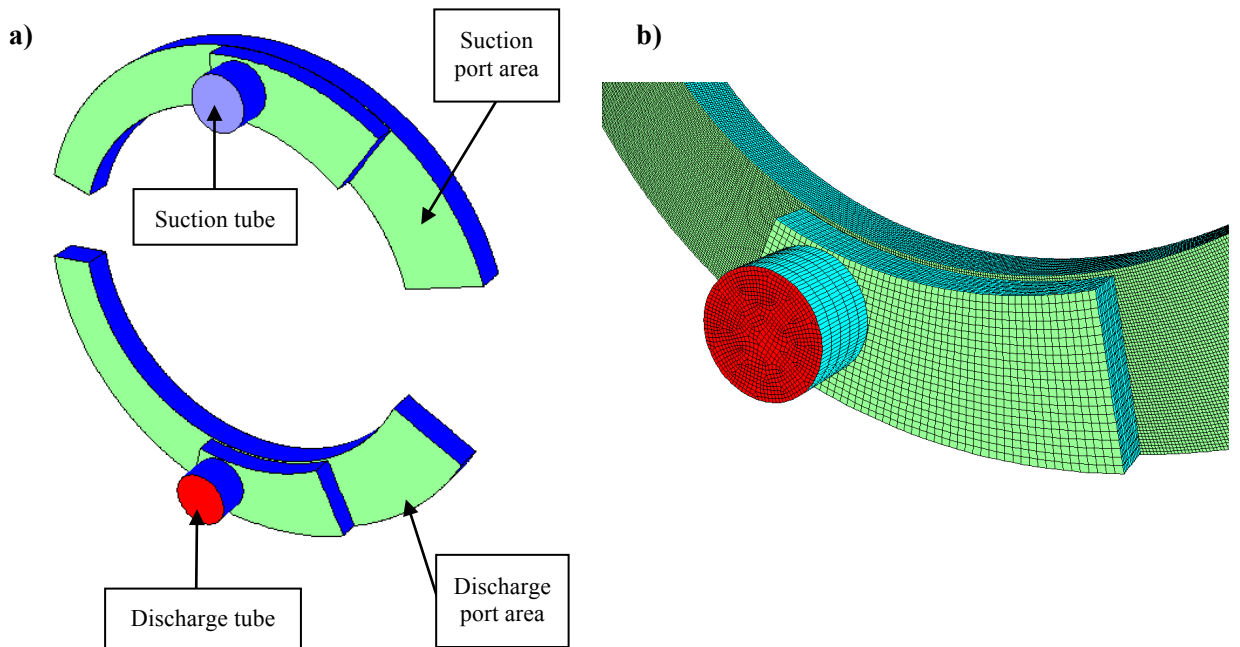


Figure 3.6: Port areas zone: a) General view and b) Detailed mesh including discharge tube and port area.

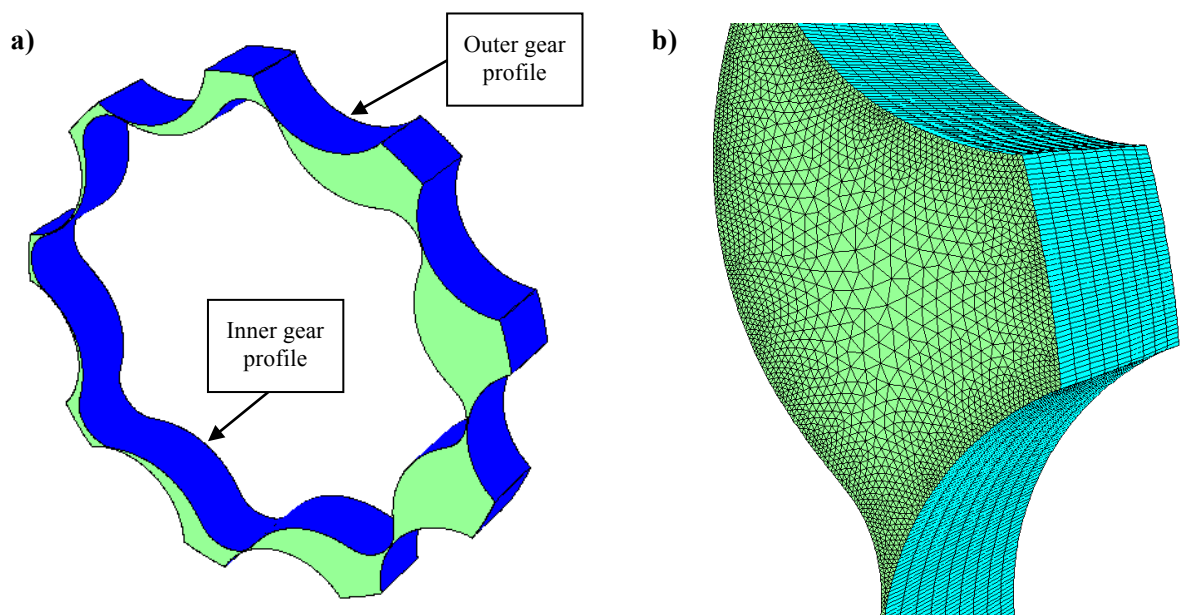


Figure 3.7: Gearing zone: a) General view and b) Detailed mesh of a chamber.

The geometry of the port area zone has been meshed through hexahedral structured stationary mesh. It includes the suction and discharge port area zones, and the suction and discharge tubes. It is shown in Figure 3.6.

The gearing zone is located between the inner gear and the outer gear profiles. In order to mesh this region, the outer gear has to be scaled and, as a consequence, no contact between the inner gear and the outer gear profiles is established and the mesh can be created. This zone is a triangular prism unstructured deforming mesh, and the complete zone and the detailed mesh of a chamber can be seen in Figure 3.7.

The base zone geometry includes de radial clearance between the outer gear and the housing of the pump. It has been meshed through hexahedral structured stationary mesh (see Figure 3.8).

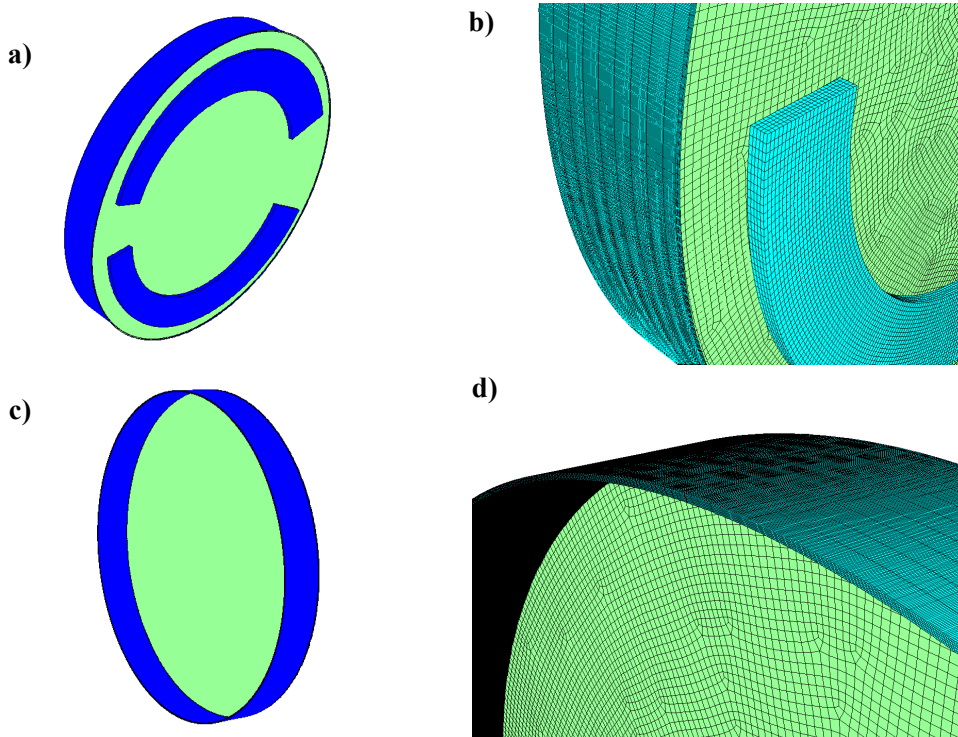


Figure 3.8: Base zone: a) General view of the lower area, b) Detailed mesh of the lower area, c) General view of the upper area and d) Detailed mesh of the upper area.

3.6.2 Mesh deformation algorithm

The simulations have been carried out through a dynamic mesh, which is deformed and locally reconstructed, allowing considerable mesh quality to the computation time. The inner gear is rotated counterclockwise and, consequently, the outer gear rotates counterclockwise, albeit slightly more slowly with the angular velocity ratio $(Z-1)/Z$, being Z the number of teeth of the outer gear. In order to update the volume mesh in the deforming regions subject to the motion defined at the boundaries, the Spring-

Based Smoothing Method has been used, as employed in a similar geometry of gerotor pump in Gamez-Montero et al., 2011.

In the spring-based smoothing method, the edges between any two mesh nodes are idealized as a network of interconnected springs. The initial spacings of the edges before any boundary motion constitute the equilibrium state of the mesh. A displacement at a given boundary node will generate a force proportional to the displacement along all the springs connected to the node. Using Hook's Law, the force on a mesh node can be written as

$$\vec{F}_i = \sum_j^{n_i} k_{ij} (\Delta\vec{x}_j - \Delta\vec{x}_i) \quad (3.17)$$

Where $\Delta\vec{x}_j$ and $\Delta\vec{x}_i$ are the displacements of node i and its neighbour j , n_i is the number of neighboring nodes connected to node i , and k_{ij} is the spring constant (or stiffness) between node i and its neighbour j . The spring constant for the edge connecting nodes i and j is defined as

$$k_{ij} = \frac{1}{\sqrt{|\vec{x}_i - \vec{x}_j|}} \quad (3.18)$$

At equilibrium, the net force on a node due to all the springs connected to the node must be zero. This condition results in an iterative equation such that

$$\Delta\vec{x}_i^{m+1} = \frac{\sum_j^{n_i} k_{ij} \Delta\vec{x}_j^m}{\sum_j^{n_i} k_{ij}} \quad (3.19)$$

Since displacements are known at the boundaries (after boundary node positions have been updated), equation (3.19) is solved using a Jacobi sweep on all interior nodes. At convergence, the positions are updated such that

$$\vec{x}_i^{n+1} = \vec{x}_i^n + \Delta\vec{x}_i^{m,converged} \quad (3.20)$$

where $n+1$ and n are used to denote the positions at the next time step and the current time step, respectively.

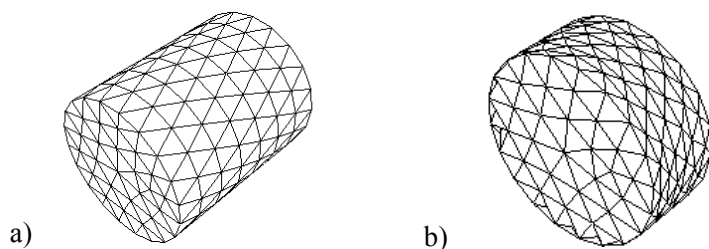


Figure 3.9: Spring-based smoothing on interior nodes. a) Start. b) End. Adapted from ANSYS FLUENT's Theory Guide

The spring constant factor (defined in FLUENT) can be adjusted between 0 and 1. A value of 0 indicates that there is no damping on the springs, and boundary node displacements have more influence on the motion of the interior of nodes. A value of 1 imposes the default level of damping on the interior node displacements as determined by solving related equation. In our particular case the spring constant that appears in equation (3.17) is taken as $k_{ij} = 1$.

The effect of the spring-based smoothing method is illustrated in Figure 3.9.

As our model contains deforming boundary zone, we use the boundary node relaxation to control how the node positions on the deforming boundaries are updated. On deforming boundaries, the node positions are updated such that

$$\vec{x}_i^{n+1} = \vec{x}_i^n + \beta \Delta \vec{x}_{spring}^{m,converged} \quad (3.21)$$

where β is the boundary node relaxation. A value of 0 prevents deforming boundary nodes from moving (equivalent to turning off smoothing on deforming boundary zones) and a value of 1 indicates no under-relaxation. We have set its value to 0.75.

The solution of equation (3.19) can be controlled using the values of Convergence Tolerance and Number of Iterations. ANSYS FLUENT solves equation (3.19) iteratively during each time step until one of the following criteria is met:

- The specified number of iterations has been performed
- The solution is converged for that time step:

$$\left(\frac{\Delta \vec{x}_{rms}^m}{\Delta \vec{x}_{rms}^1} \right) < \text{convergence tolerance} \quad (3.22)$$

where $\Delta \vec{x}_{rms}^1$ ¹ is the interior and deforming nodes RMS displacement at the first iteration.

In the present work the convergence tolerance has been taken as 0.001 and the number of iterations have been set to 150.

When the boundary displacement is large compared to the local cell sizes, the cell quality can deteriorate or the cells can become degenerate. This will invalidate the mesh and consequently will lead to convergence problems when the solution is updated the next time step.

To circumvent this problem, ANSYS FLUENT agglomerates cells that violate the skewness or size criteria and locally remeshes the agglomerated cells or faces. If the new cells or faces satisfy the skewness criterion, the mesh is locally updated with the new cells (with the solution interpolated from the old cells). Otherwise, the new cells are discarded.

ANSYS FLUENT includes several remeshing methods that include local remeshing, local face remeshing, face region remeshing, and 2.5D surface remeshing. Using the local remeshing method, ANSYS FLUENT marks cells based on cell skewness and minimum and maximum length scales as well as an optional sizing function. From the available remeshing methods, it has been chosen the 2.5D Surface Remeshing Method, as it is the one that fits with the 2.5D technique that has been used. Faces on a deforming boundary are marked for remeshing based on face skewness (set to 0.6), minimum and maximum length scale (set to 0.0001 and 0.0008, respectively) and an optional sizing function. If the faces are expanding, they are allowed to expand until the maximum length scale is reached. Otherwise, if the faces are contracting, they are allowed to contract until the minimum length scale is reached.

An example of mesh deformation and local remeshing is shown in Figure 3.10, for the gearing zone, using spring-based deformation algorithm and the 2.5D surface remeshing method. It can be seen the evolution between two consecutive time steps.

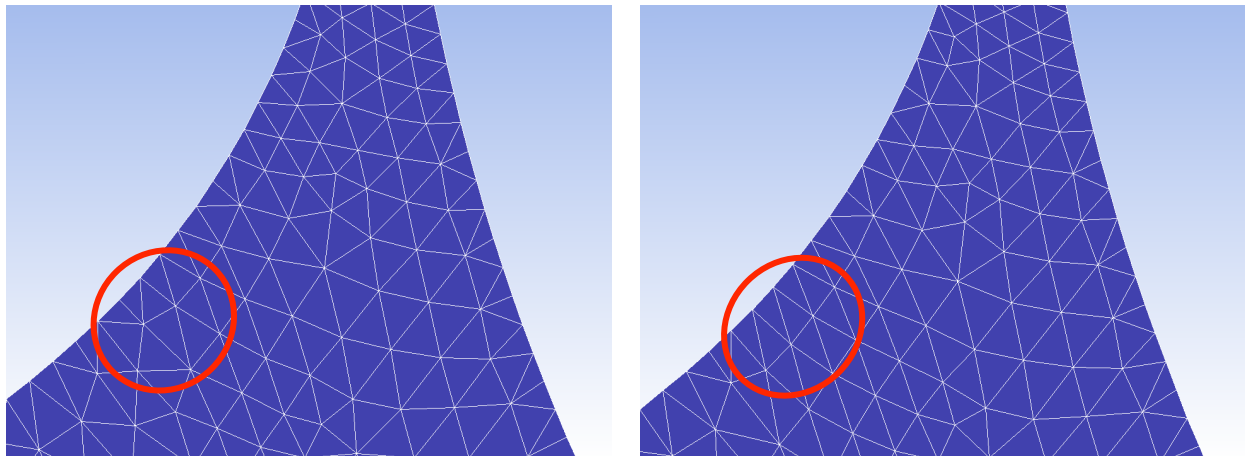


Figure 3.10: Mesh deformation and local remeshing for gearing mesh zone, between 2 time steps.

3.6.3 Mesh quality analysis and grid independence study

The deformation of the mesh is qualitatively defined with the equivolume skewness of a cell, defined as:

$$Sk = \frac{S_e - S_c}{S_e} \quad (3.23)$$

where S_c is the cell surface and S_e is the surface of an equilateral triangle with the same circumradius. In all the numerical simulations of the present work, the maximum value of the area-averaged equivolume skewness Sk is below 0.89 for both the inter-profile surfaces, which is less than the value of 1 defined as a limit for a good mesh quality deformation.

Number of mesh cells ($\times 10^6$)	Mean normalized flow for the following viscous models	
	Laminar	Turbulent
0.6	0.9958	0.9962
1.2	0.9975	0.9974

Table 3.1: Results of the grid independence study

A grid independence study has been carried out to obtain the mesh convergence which details are provided in Table 3.1 where it is shown that the error in the mean normalized flow is 0.17% for the laminar model and 0.12% for the turbulent model.

Considering this minimum error and the performance of the central processing unit, the simulations presented in this work have been performed with a mesh of about 600,000 cells and where the Courant number (the dimensionless number based on the time step, velocity and average cell size) is always less than 0.5.

3.7 Influence of simulating the contact points

In order to model the manufacturing tolerance between the inner and outer gears, the internal diameter of the outer gear is increased and, as a consequence, the two trochoidal profiles do not share any contact point. In principle, teeth contact cannot be neglected, attending to the high working pressures at which this type of pump operates (in the order of MPa): leakage is an important phenomenon to be considered, and flow rate fluctuations are also affected by the effect of the contact points. In order to achieve the more realistic simulation model of the pump, two different possibilities of simulating the contact points have been studied: no contact points and all contact points.

First, the Gearing Contact Point strategy is tested with an analytical approach establishing new boundary conditions of contact for all teeth. Results are shown normalized with the gearing period (T_g) for time and the theoretical volumetric flow rate (Q_g) for the flow rate. They present a very good agreement with the analytical model, being the simulations results about 0.2% higher than the analytical values, due mainly to the scaling of the outer gear. The irregularity index is 2.8% in the analytical model and 2.5% in the all-contact-points simulation. This difference can be understood considering that the analytical model does not take into account the effects of the compressibility of the fluid. Note that Figure 3.11 presents a point of mathematical stiffness that can be seen approximately at the normalized values of time of 1.5, 2.5 and 3.5.

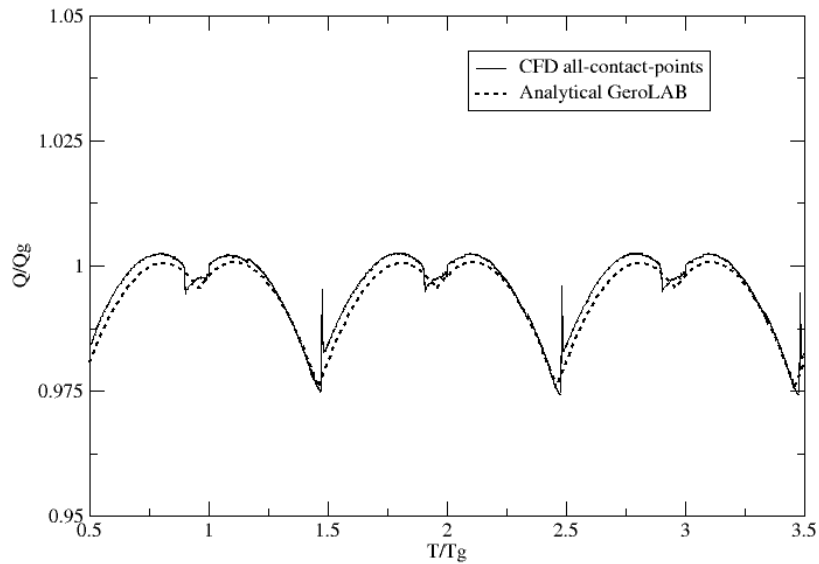


Figure 3.11: GeroLAB analytical and laminar CFD results of the instantaneous flow at the outlet port (0 MPa and 7.5 rpm)

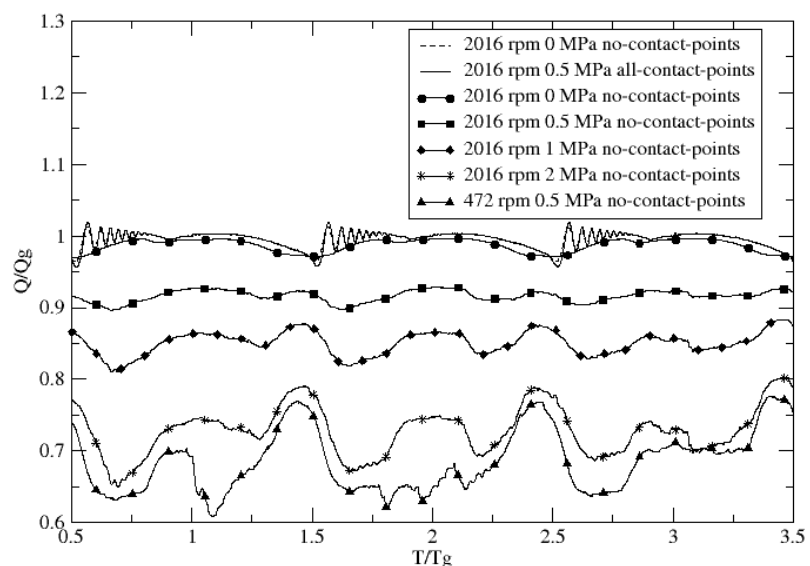


Figure 3.12: Instantaneous flow at the outlet port, 472 and 2016 rpm inner gear. Laminar CFD results by simulating no contact points and Z contact points with a pressure of 0, 0.5, 1 and 2 MPa

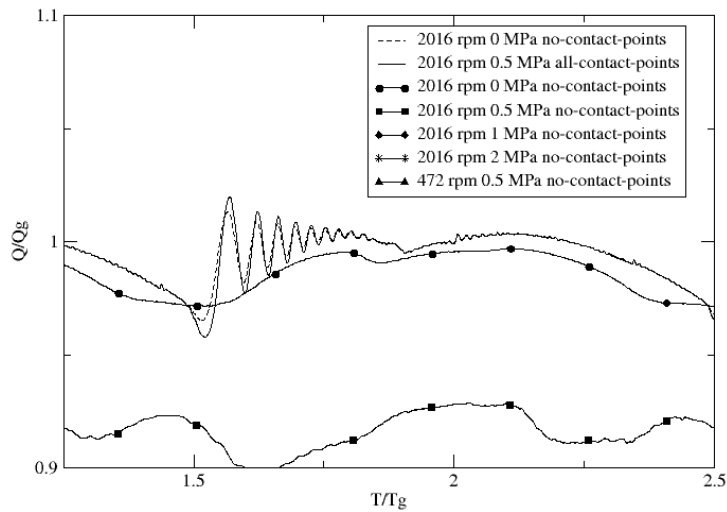


Figure 3.13: Detail of instantaneous flow at the outlet port, 472 and 2016 rpm inner gear. Laminar CFD results by simulating no contact points and Z contact points with a pressure of 0, 0.5, 1 and 2 MPa

Figure 3.12 shows the influence of the teeth contact with respect to the working pressure and the rotary velocity of the pump. A comparison is done for the two possibilities of simulating the contact points, showing that at 0 and 0.5 MPa the no-contact-points simulation results in a reduction of the flow rate of 1% and 8%, respectively, compared to the all-contact-points simulation. Besides, it can be seen that the 0 MPa no-contact-points contour of the instantaneous flow is clearly distorted. The influences of no-contact-point points and all-contact-points at 0 MPa are manifested in the reduction of almost 2% in the peak values, which can be justified by the compressibility effects when all contact points are simulated.

At low rotational velocities (472 rpm) and 0.5 MPa, when no contact points are simulated, the instantaneous flow and hence the volumetric efficiency are reduced by approximately 30% compared with those for the all-contact-points simulation. The effect of the working pressure is also clearly shown by the no-contact-points simulation results because the volumetric efficiency is strongly reduced, falling for instance to 83% in the 2016 rpm and 1 MPa simulation. As a consequence, the influence of the teeth contact proves to be significant and it is proved that the *Gearing Contact Point* strategy establishes a more realistic leakage flow model in the interteeth clearances.

The BondGraph simulated instantaneous flow results for ideal flow (no leakage) and leakage through the trochoidal profiles (Q_f,pt). The influence of the leakage is indicated by the reduction of the main peak. This phenomenon has the same explanation as before. A high-pressure volume of oil from the outlet zone comes into the chamber through the interteeth clearance passage-way and the leakage

phenomenon appears. The volume of the chamber is now less compressed and this effect is translated as flow ripple fluctuations because of the fluid compressibility. The same argument can be used with the minimum value when the chamber reaches the inlet zone.

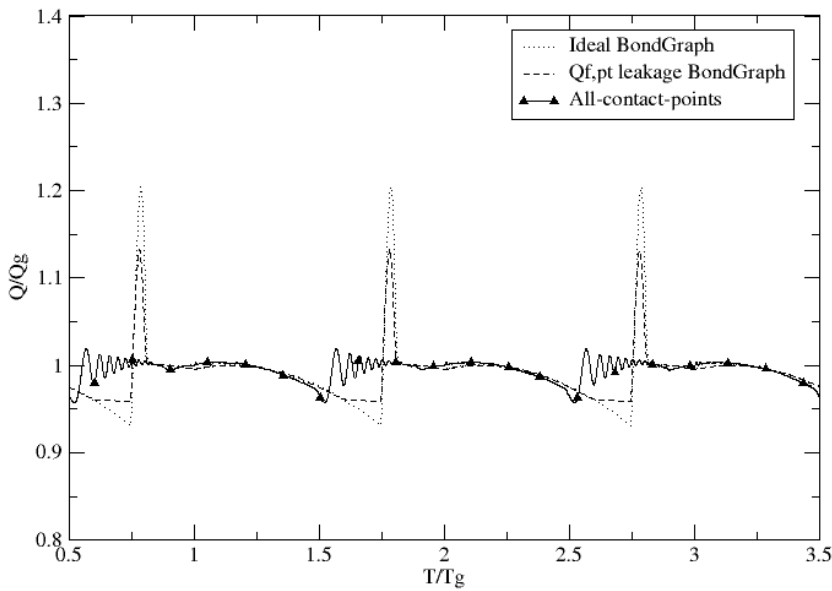


Figure 3.14: BondGraph ideal and with leakage (Q_f,pt), and laminar CFD results of the instantaneous flow at the outlet port (0.5 MPa and 2016 rpm)

3.8 Numerical Simulation conditions

Although the methodology described in this chapter can be used in order to perform turbulent simulations, the following results correspond to laminar turbulence model. This selection meets the requirements of the experimental testing: owing to the reason that the maximum experimental possible rotational speed of the gerotor pump is 250rpm, the flow is laminar and there is no need for a turbulent simulation (see section Operating conditions for the demonstration of this maximum rotational speed). Nevertheless, here it is presented one turbulent simulation of the problem, to check that there are no differences between the turbulent and laminar cases. The rest of results correspond to laminar simulations.

The comparative between the computations of a same case by means of a laminar or turbulent model is shown in Figure 3.15, for a complete rotation of the gearing mechanism. The instantaneous flow ripple in the outlet pipe is represented, for both computations, performed for a rotational velocity of the inner gear of 250 rpm and gauge pressure of inlet and outlet pipes of 0bar. The maximum relative deviation between cases is of 0.86%, with respect to the simulated instantaneous flow rate.

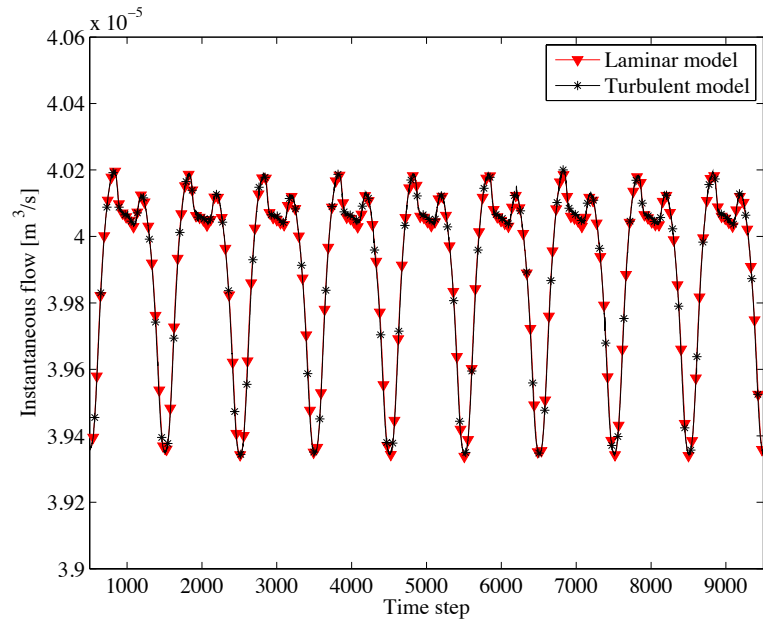


Figure 3.15: Comparative between results obtained through laminar and turbulent models

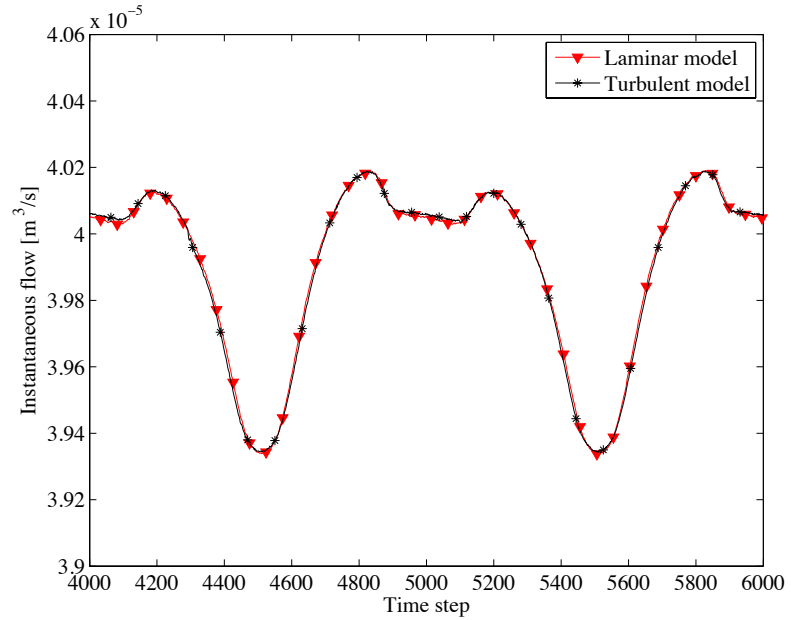


Figure 3.16: Detail of the comparative between laminar and turbulent models

The geometry of the simulated gerotor pump and the properties of the fluid are shown in Table 3.2.

<i>Geometry and operation conditions of the simulated gerotor pump</i>	
Eccentricity	2.85 mm
External diameter through the tips of the teeth of the inner gear	65.45 mm
Radius of the circle to complete the outer gear	35.8 mm
Gear thickness	9.25 mm
Arc radius of the outer gear tooth	10.85 mm
Number of outer teeth	9
Number of inner teeth	8
Inlet gauge pressure	0 bar
Outlet gauge pressure	0.54 bar
Inner gear rotational velocity	250 rev/min
Volumetric capacity	9.8 cm ³ /rev
<i>Properties of the mineral oil used in the simulation</i>	
Density	885 kg/m ³
Viscosity	$2.8 \cdot 10^{-2}$ Pa·s
Compressibility coefficient	1.5×10^{-9} Pa

Table 3.2: Geometry, operation conditions and fluid properties of the CFD simulations

3.9 Numerical Simulation Results and Conclusions

First, Figure 3.17 show the result of the instantaneous flow rate in the outlet pipe, for a complete rotation of the gearing, while Figure 3.18 presents the result of the simulated flow pulsation in the maximum area chamber.

Next, some examples of the numerical simulation are presented, to see the potential of the CFD tool. We are not evaluating this particular results (corresponding to time step number 500). They are shown in order to see the possibilities that offer the developed CFD tool.

Figure 3.19 shows the volume streamtraces of the whole fluid domain. Also, it contains the pressure contours. Figure 3.20 shows a detail of the streamtraces near the outlet and inlet zones.

Figure 3.22 show the surface stramtraces between trochoidal profiles, together with the velocity contours.

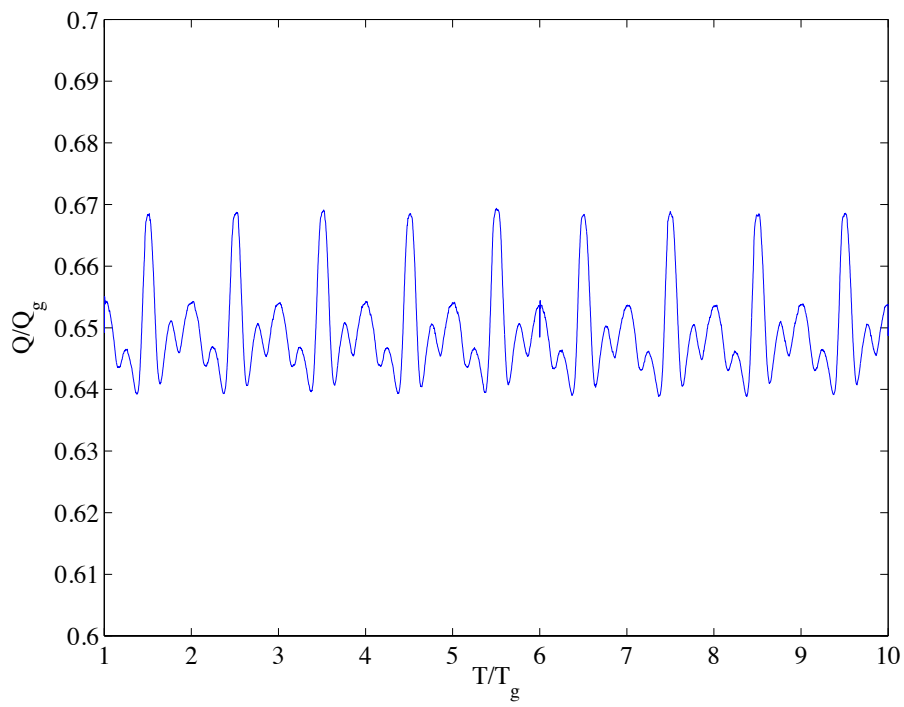


Figure 3.17: Instantaneous flow rate in the outlet pipe.

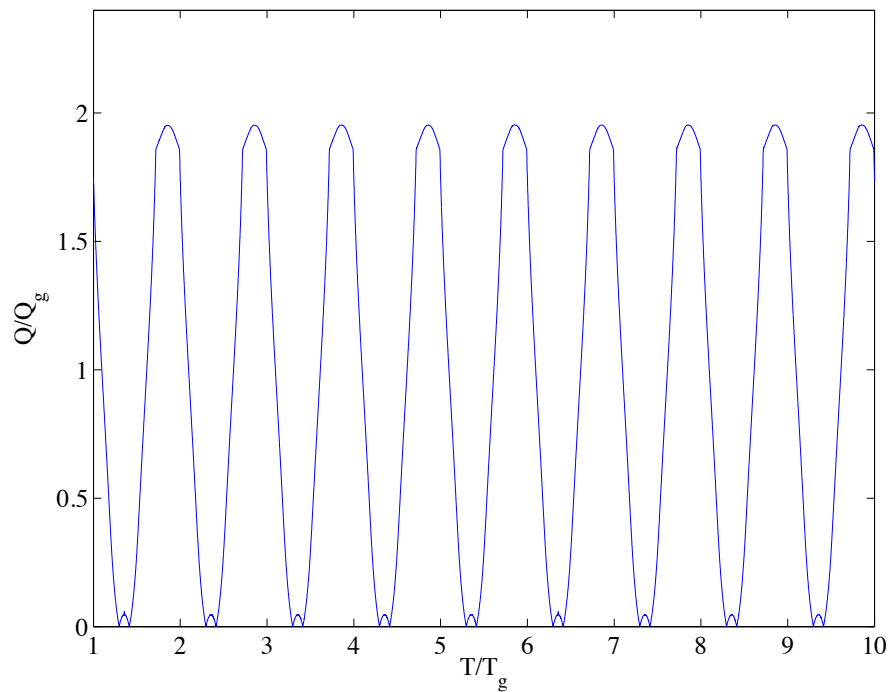


Figure 3.18: Flow pulsation in maximum area chamber

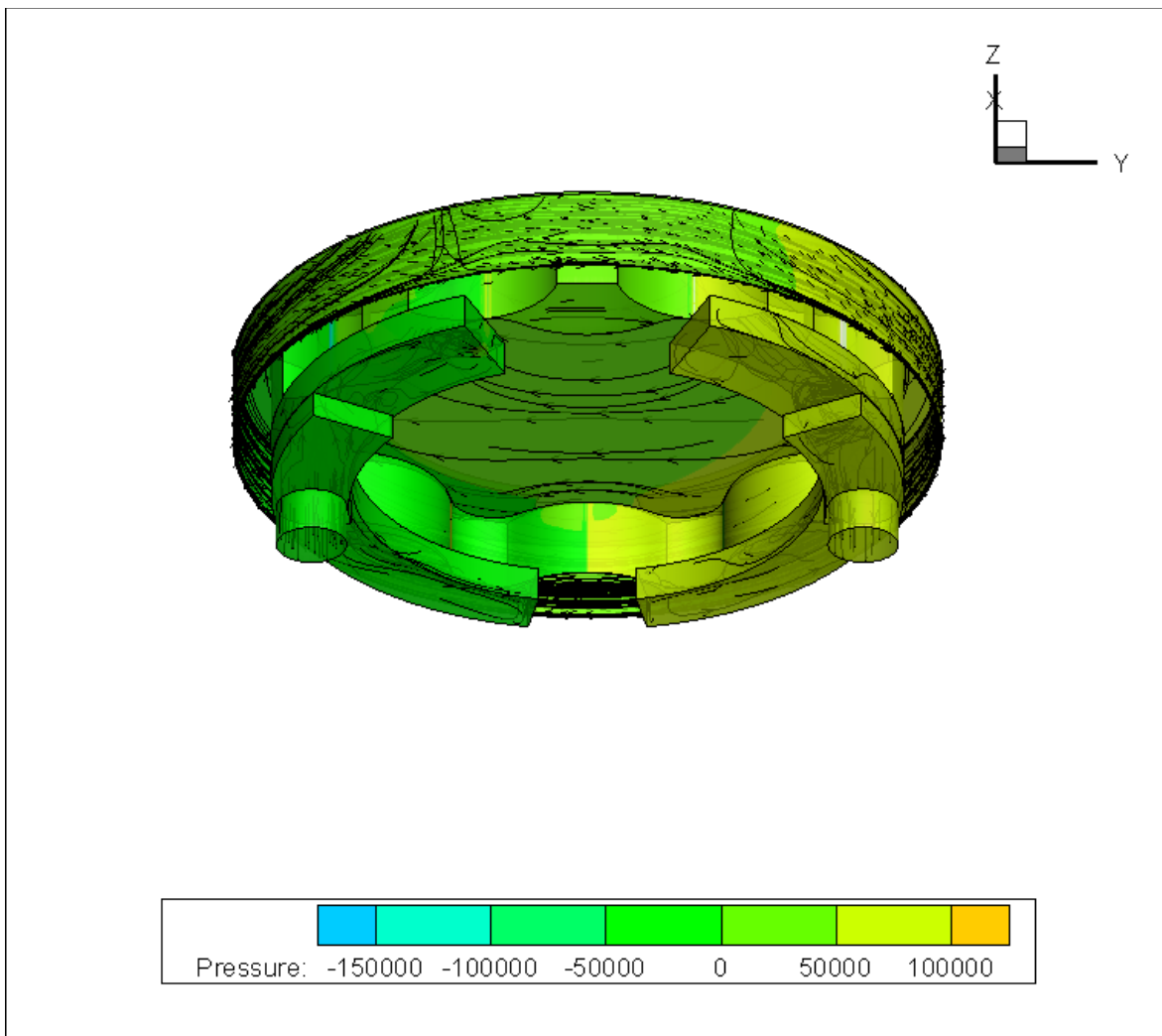


Figure 3.19: Volume streamtraces

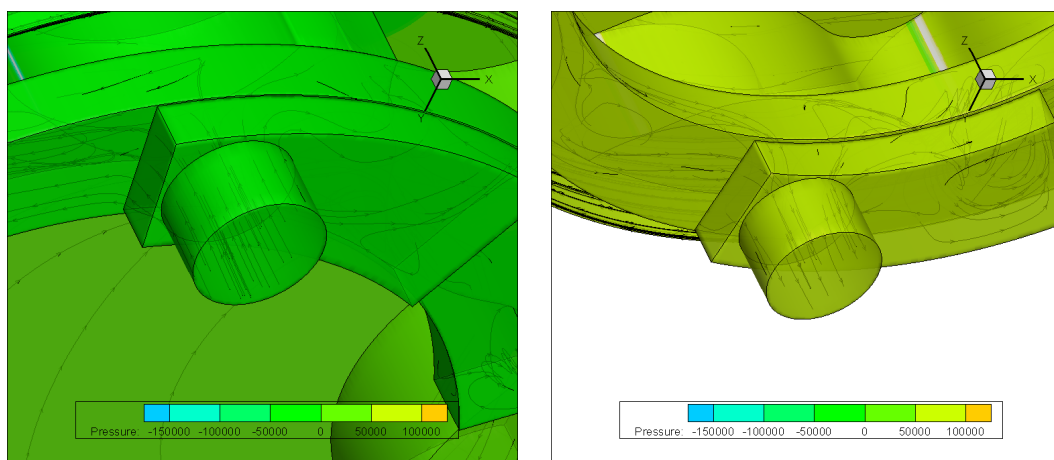


Figure 3.20: Volume streamtraces in suction (left) and discharge (right) pipes

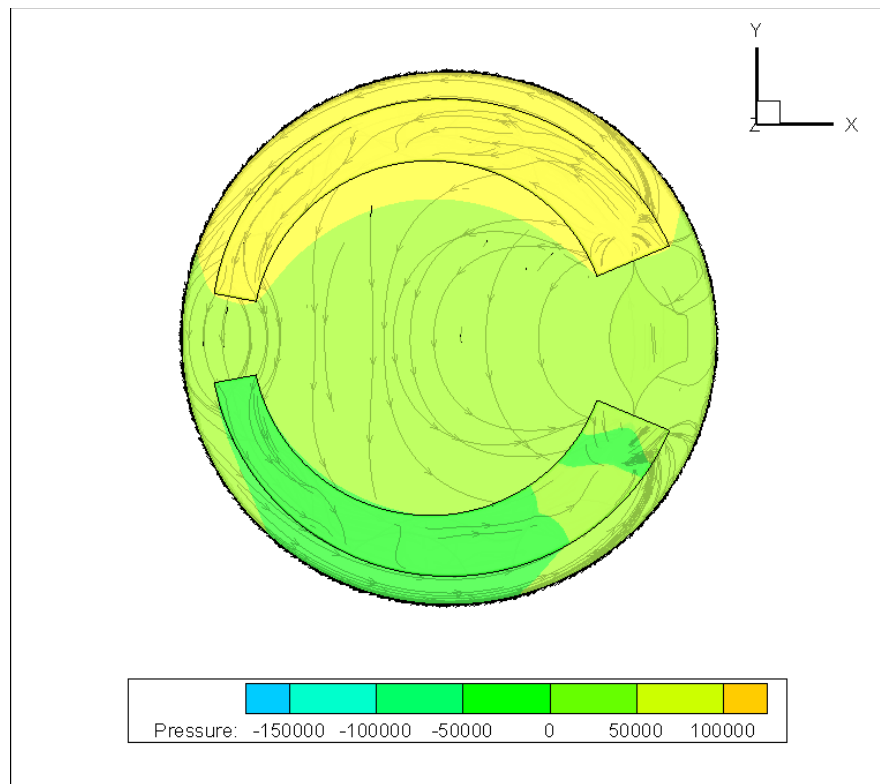


Figure 3.21: Volume streamtraces, XY view

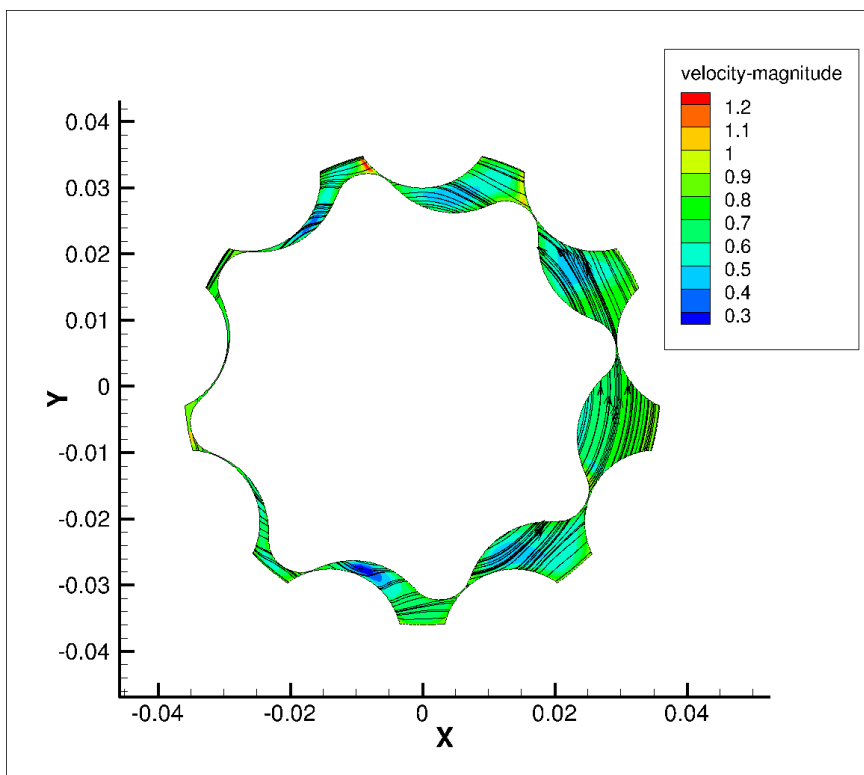


Figure 3.22: Surface streamtraces and contours of velocity between trochoidal profiles

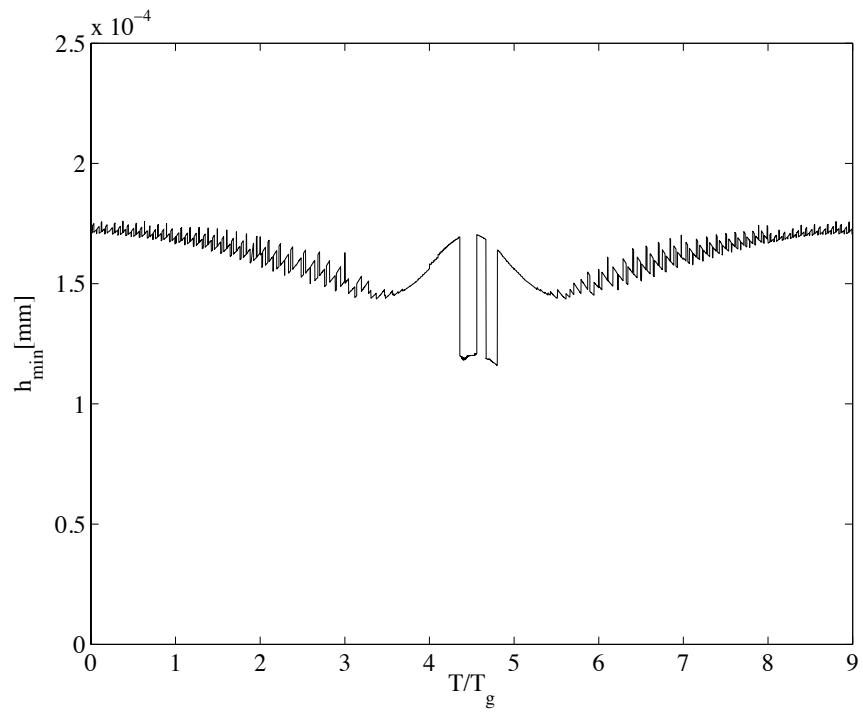


Figure 3.23: Minimum radial clearance for a complete rotation of the gearing (tooth 1)

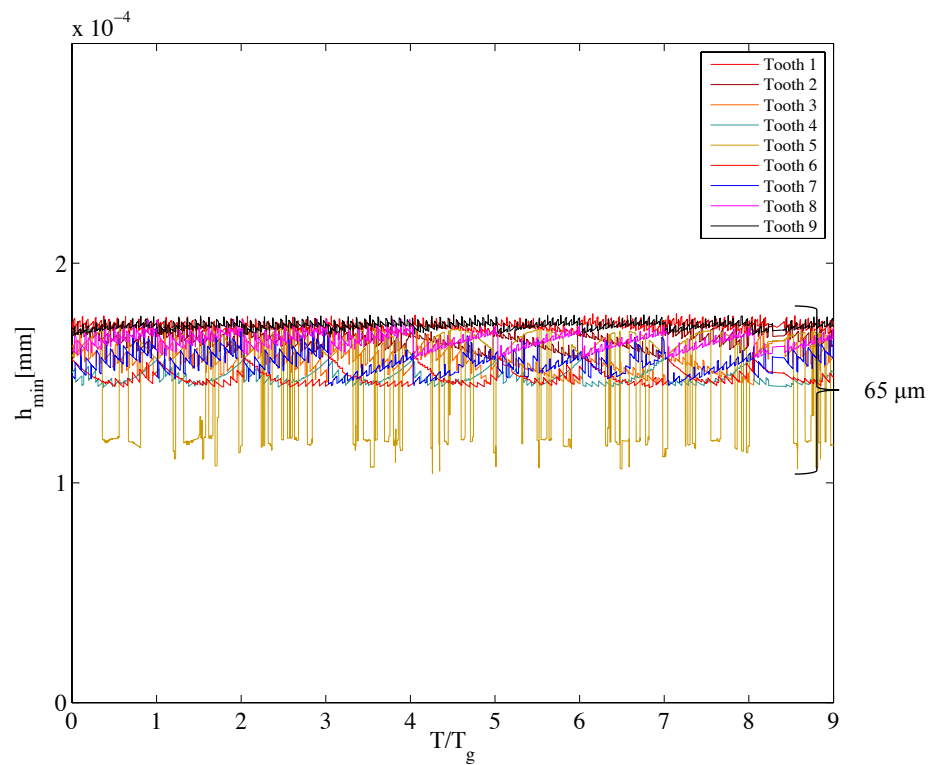


Figure 3.24: Minimum radial clearance for a complete rotation of the gearing (all teeth)

The minimum radial clearance between trochoidal profiles is obtained thanks to the *Gearing Contact Point* user-defined function. Figure 3.23 shows this minimum clearance for a complete cycle of rotation of one tooth (tooth 1 is represented), while Figure 3.24 shows the information concerning to all teeth. It can be seen that the variation of the minimum radial clearance is limited between a range of 65 μm .

On the one hand, thanks to the CFD model presented in this thesis, we are able to learn the intricate aspects of the flow behaviour inside the pump. We have more certainty about the operation of the pump and about the tools that have been used until the present for the study of its performance.

On the other hand, this CFD model will be used as a tool to complement the BondGraph model in the future work, as it allows the acquirement of fluid-dynamic parameters in the whole fluid domain. Once the CFD simulation is finished, we have the information about the complete velocity and pressure fields inside the pump. These results can be used in order to characterize any desired flow passage, and that would represent an advance in the dynamical simulation, as it would become a more realistic approach. One example of this type of parameters would be the discharge coefficient that characterizes the leakage flow between trochoidal profiles.

4 Experimental Study of a Gerotor Pump by Time-Resolved Particle Image Velocimetry

4.1 Introduction to the Experimental Study

As seen in *Chapter 1*, it is virtually impossible to measure accurately and directly the flow ripple generated by the pump, and indirect measures are used in order to characterize its instantaneous flow. That is measurements of pressure pulses, and estimate the flow ripple with the help of an algorithm.

The only method to validate a new design of trochoidal gear pump is to perform a test in normal operating conditions of the real pump. According to the documented work, there is not an existing procedure to obtain the flow ripple generated by the pump in a directly and accurate measure.

Regarding the flow visualization techniques applied to gerotor pumps, only one reference has been found (in Japanese). Itoh (Itoh et al., 2005) carries out a study of the flow structure and the volumetric efficiency using light-reflecting tracer particles in a transparent model of the pump of external dimensions of 76.8mm and a maximum rotating velocity of 31 rpm. And, particularly about Particle Image Velocimetry, there is not documented work of this procedure applied to trochoidal gear pumps.

The experimental work presented in this thesis is aimed to the improvement of the Time-Resolved Particle Image Velocimetry (TRPIV) applied to positive displacement pumps, and specifically to trochoidal gear pumps. The effort made in this field is focused in order to make progress in this experimental technique, knowing its limitations as a new technique in development with respect to trochoidal gear pumps. It should not be interpreted as the validation of the theoretical models, as the use of TRPIV in trochoidal gear pumps is not fully developed and the limitations of its use must be taken into account.

The results obtained through TRPIV help the understanding of the real behaviour of the pump, as it is possible to obtain a whole velocity field in a particular section of the pump. Even the three-dimensional velocity field could be analysed, which would be very useful in order to study the influence of the geometry of the port areas in a real pump.

4.2 Principles of TRPIV

PIV is a non-intrusive measurement technique that needs a recording medium, an illuminating light source and a computer for image processing. Small tracer particles are introduced in a region of the fluid and are illuminated by two consecutive short duration light pulses produced by a laser. The image of the particles during two consecutive laser pulses is recorded by a CMOS camera, where each exposure is isolated on his own frame. Processing these consecutive images by means of cross-correlation methods allows the obtaining of the velocity vectors associated with the fluid flow. In the case of TRPIV, each pair of images between two pulses is used to evaluate the instantaneous velocity field.

To apply the PIV technique it is necessary to seed the fluid of interest with some kind of tracer particles. It is assumed that the motion of the tracer particles follows faithfully the movement of the fluid. Thus, the motion of the fluid can be determined by measuring the particle displacements through evaluation of the PIV recordings. The recorded images are divided into small interrogation areas and analyzed by means of a correlation method. With the aid of PIV technique quantitative two-dimensional information of the fluid velocity is obtained. Comprehensive descriptions and explanation on the principle of the PIV technique have been provided by Adrian (Adrian et al., 2011).

4.3 Tracer particles

Flow seeding is a significant part in the experimental PIV set-up. This is achieved by adding small tracer particles into the flow. As explained before, it is assumed that the fluid and particles move as one. The obtained images of the particles where the region of interest is illuminated at least twice by a laser, allow computing the velocity of the flow field. The light scattered by the particles can be recorded on a single frame or on a sequence of frames (in the present study each image is recorded in a single frame). The displacement of the particle images between the light pulses is then determined through evaluation of the PIV recordings.

The principle of PIV is based on the direct determination of the two fundamental dimensions of the velocity as length and time. The technique measures the particle velocity which is determined instead of fluid velocity. Therefore, properties of the particles have to be checked in order to avoid significant

discrepancies between fluid and particle motion. The selection of the particles comprises a basis of the velocity measurements in PIV. These particles should be as small as possible in order to ensure good tracking of the fluid motion. On the other hand, they may not be too small, since they will not scatter enough light. If tracer particles scatter light weakly, then more powerful lasers or more sensitive cameras that increase the costs and safety issues should be used. It is better to search ideal tracer particles that follow the flow faithfully and scatter enough light for the flow system in order to obtain accurate velocity field of the flow, as indicated in Raffel (Raffel et al., 2007).

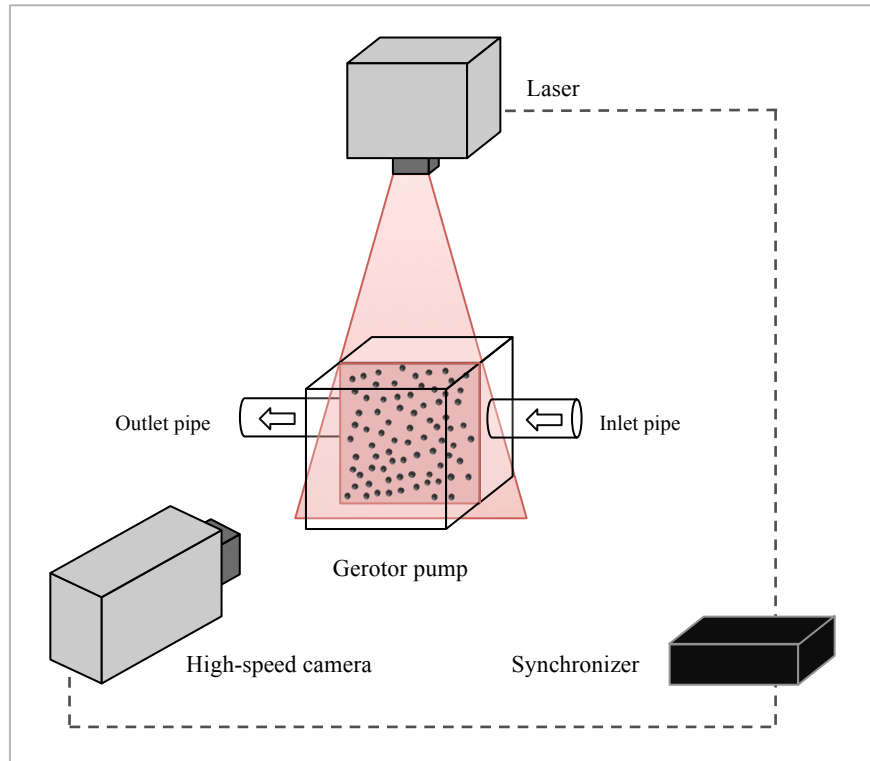


Figure 4.1: Typical experimental assembly for a PIV study in a Gerotor pump.

Tracer particles should follow the fluid flow without changing its pattern. Therefore, particle density (ρ_p) should closely match the density of the fluid (ρ_f). In addition, at zero-velocity condition, tracer particles should stay suspended in the fluid without sinking or floating up due to gravitational effects and buoyancy. Therefore, fluid mechanical properties of the particles have to be examined in order to avoid significant discrepancies between fluid and particle motion.

4.3.1 Fluid mechanical properties

A primary source of error is the influence of gravitational forces if the densities of the fluid ρ_f and the tracer particles ρ_p do not match. If we assume spherical particles in a viscous fluid at a very low

Reynolds number, the Stokes' law defines the frictional force \vec{F}_d (known as Stokes' drag) acting on the interface between the fluid and a particle:

$$\vec{F}_d = 3\pi\mu d_p \vec{u} \quad (4.1)$$

where μ is the dynamic viscosity, d_p is the diameter of the particle, and \vec{u} is the particle's velocity.

For the previous assumptions, Stokes' drag law also defines the particle's gravitationally induced velocity as:

$$v_g = d_p^2 \frac{(\rho_p - \rho_f)}{18\mu} g \quad (4.2)$$

where g is the acceleration due to gravity, μ the dynamic viscosity of the fluid, d_p is the diameter of the particle and, ρ_p and ρ_f are the density of the particle and the fluid respectively.

We can also derive and estimate for the velocity lag of a particle in a continuously accelerating fluid:

$$\vec{u}_s = \vec{u}_p - \vec{u} = d_p^2 \frac{(\rho_p - \rho_f)}{18\mu} \vec{a} \quad (4.3)$$

where \vec{u}_p is the particle velocity. The step response of \vec{u}_p typically follows an exponential law if the density of the particle is much greater than the fluid density:

$$\vec{u}_p(t) = \vec{u} \left[1 - \exp \left(-\frac{t}{\tau_s} \right) \right] \quad (4.4)$$

where the relaxation time τ_s is given by:

$$\tau_s = d_p^2 \frac{\rho_p}{18\mu} \quad (4.5)$$

If the fluid acceleration is not constant or Stokes drag does not apply (e.g. at higher flow velocities) the equations of the particle motion become more difficult to solve, and the solution is no longer a simple exponential decay of the velocity. Nevertheless, τ_s remains a convenient measure for the tendency of particles to attain velocity equilibrium with the fluid.

When applying PIV to liquid flows the problems of identifying particles with matching densities are usually not severe, and solid particles with adequate fluid mechanical properties can often be found.

4.3.2 Light scattering behaviour

Since the obtained particle image intensity and therefore the contrast of the PIV recordings is directly proportional to the scattered light power, it is often more effective and economical to increase the

image intensity by properly choosing the tracer particles than by increasing the laser power. In general it can be said that the light scattered by small particles is a function of the refractive index of the particles to that of the surrounding medium, the particle's size, their shape and orientation. Furthermore, the light scattering also depends on polarization and observation angle. For spherical particles with diameters, d_p , larger than the wavelength of the incident light λ , Mie's scattering theory can be applied. The Mie's scattering can be characterized by the normalized diameter, q , defined by:

$$q = \frac{\pi d_p}{\lambda} \quad (4.6)$$

If q is larger than unity, approximately q local maxima appear in the angular distribution over the range from 0° to 180° . For increasing q the ratio of forward and backward intensity will increase rapidly. Hence, it would be advantageous to record in forward scatter but, due to the limited depth of field, recording at 90° is most often used.

There is a clear tendency for the scattered light intensity to increase with increasing particle diameter. In Figure 4.2 the normalized scattered intensity of different diameter glass particles in water according to the Mie's theory is shown at $\lambda=532$ nm.

It can be seen from all Mie scattering diagrams, that the light is not blocked by the small particles but spread in all directions. Therefore, for a large number of particles inside the light sheet massive multiscattering occurs. Then the light, which is imaged by the recording lens, is not due to direct illumination but also due to fractions of light, which have been scattered by more than one particle. In the case of heavily seeded flows this considerably increases the intensity of individual particle images, because the intensity of directly recorded light - at 90° to the incident illumination - is orders of magnitude smaller than that scattered in the forward scatter range.

One interesting implication is that not only larger particles can be used to increase the scattering efficiency but also a larger number density of the particles. However, two problems limit this effect from being intensively used. First, the background noise and therefore the noise on the recordings will increase significantly as well. Second, if – as is usually the case – polydisperse particles (i.e. particles of different sizes) are used, it is finally not certain whether the number of visible particles has been increased by simply increasing the number of very large particles. Since images of larger particles clearly dominate the results of PIV evaluation, it would be difficult to give reliable estimates on the effective particle size and the corresponding velocity lag.

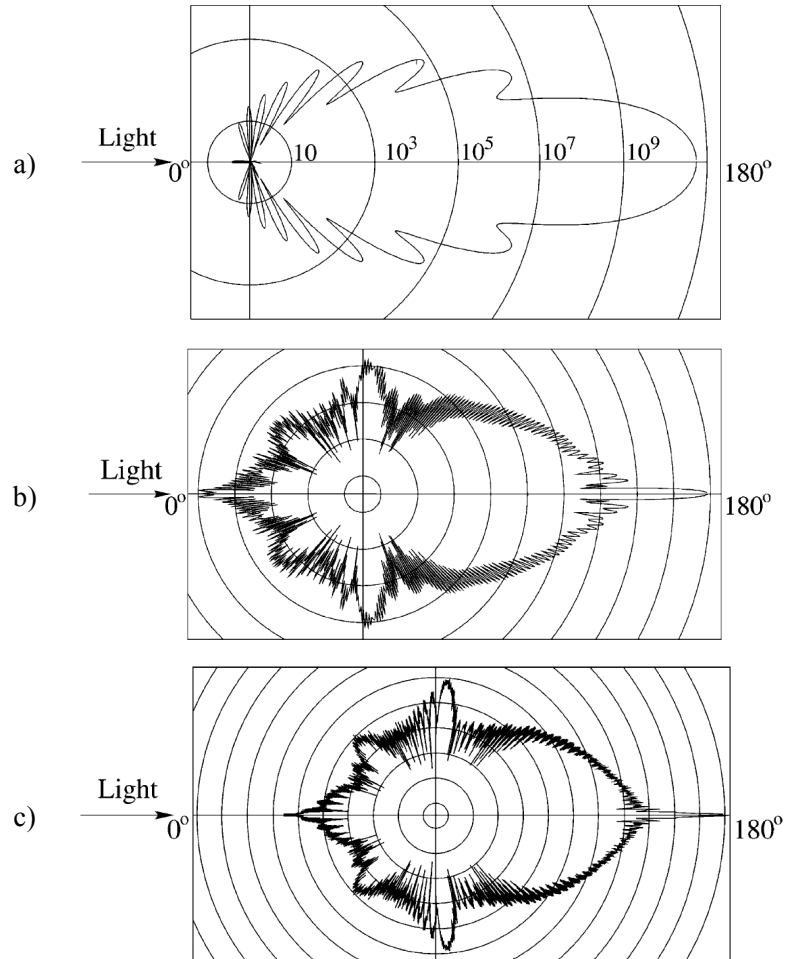


Figure 4.2: Light scattering by a glass particle of diameter D_p in water with a) $D_p=1 \mu\text{m}$, b) $D_p=10 \mu\text{m}$ and c) $D_p=30 \mu\text{m}$. Adapted from Raffel et al.; Error! No se encuentra el origen de la referencia.

4.3.3 Selected tracer particles

A new kind of alginate tracer particles has been designed and produced at the Rovira i Virgili University of Tarragona by Ertürk (Ertürk, 2012). Alginate particles present excellent flow seeding and light scattering abilities. They ensure good tracking of the fluid motion in both liquid and gas measurements. When they are used in liquid, there is not much difference in the density between the fluid and the particles thanks to their porous structure that easily absorb the analysing fluid. Also, alginate particles have soft, jelly like structure, and do not cause any damage to the inner contact surface if the machines. More details are given in further work (Ertürk et al., 2013), where it is demonstrated that alginate particles are very appropriated for turbo-machinery application in PIV.

4.4 Camera

In order to acquire high frequency time series of images in the TRPIV, a high velocity camera is needed. To capture the details of the flow in gearing pumps, it is necessary to obtain this high image acquisition, to subsequently resolve the velocity field by means of TRPIV.

The high velocity digital camera that is used in the experiments is the Photron Ultima APX-RS. Its main characteristics are shown in Table 2.1.

Photron Ultima APX-RS	
Sensor	10-bit single CMOS sensor with 17µm pixel
Frame rate at full resolution	3000 frames per second
Resolution	1024x1024 pixel
Buffer memory	2 GB
Record time	0.7 seconds 2048 frames
Exposure duration	16.7ms to 2µs global electronic shutter independent of frame rate and overexposure protection
Lens	Sigma 105mm f/2.8 EX DG macro

Table 4.1: Specifications of the high velocity digital camera

4.5 Laser

The chosen laser for the presented experiments was the Monocrom LU80250-FSAC. It is a 800 nm (infrared) laser which main features are given in Table 4.2. It is a diode laser, meaning that the active medium is a semiconductor similar to that found in a light-emitting diode that is powered by injected electric current. Laser diodes are arranged in a bar, making possible the production of the necessary laser sheet with optical elements that are encapsulated in the laser box. Therefore, the laser box is directly placed in front of the gear pump without the need for additional optical elements between laser and pump.

The fact of being infrared requires us to be extremely careful when performing the experiments, as the laser beam cannot be seen but it can produce serious damage if reflected towards the eyes. Apart from wearing IR protection glasses, the whole bench is surrounded by black walls and a black curtain that is closed before turning on the laser.

Monocrom LU80250-FSAC	
Center wavelength	805 ± 5nm
Maximum output peak power	250 W
Maximum operation current	280 A
Pulse length	10-100 µs
Maximum pulse energy	2.5 mJ at 10 µs
	25mJ at 100 µs
Maximum frequency	5 kHz
Laser beam dimensions	12 x 0.7 mm at output

Table 4.2: Specifications of Monocrom LU80250-FSAC

4.6 Synchronization between camera and laser

Laser pulses have to be synchronized with the camera trigger using a synchronizer. In the case of TRPIV, the camera must be continuously triggered in order to generate each pair of frames to temporally resolve the flow. The Function Generator TG2000 20MHz DDS has been used as the synchronizer mechanism between camera and laser. It can operate with standard waveforms of sine, square, triangle, DC, positive pulse and negative pulse. The available operating modes are continuous, gated, sweep, external amplitude modulation, frequency shift keying and tone. In the present study, the square waveform at continuous mode has been chosen, and its mains characteristics are shown in Table 4.3.

TG2000 20MHz DDS (square waveform, continuous mode)	
Range	1mHz to 20MHz
Resolution	1mHz or 6 digits
Symmetry control	20% to 80% (1% resolution) 1mHz to 10MHz
Accuracy	10ppm for 1 year
Output level	2.5mV to 10Vp-p into 50Ω
Rise and fall times	<22ns
Aberrations	<5% + 2mV

Table 4.3: Specifications of TG2000 20MHz DDS function generator (square waveform)

4.7 Mathematical background of statistical PIV Evaluation

The main objective of the evaluation of PIV recordings is to determine the displacement of the particles between two recorded frames. This results in the most probable displacement vector for that particular particle pattern. The process is repeated for all the interrogation areas of the two frames resulting in a complete vector diagram of the studied flow field. Finally, the results of velocity can be validated by properly correcting the erroneous vectors.

The first step consists in dividing the total area of the frame in the interrogation areas of NxN pixels size. As indicated in Adrian (Adrian et al., 2011), typically high-image density PIV experiments in gases and liquids have densities between 5 and 15 particles in an interrogation area, in order to have a high probability of good analysis results. This information has been taken into account to correctly select the size of the interrogation areas, which for this work has been taken as 32x32 pixels.

As already mentioned before, PIV recordings are most often evaluated by locally cross-correlating two frames of single exposures of the tracer ensemble. Assuming a constant displacement of all particles inside the interrogation area, the particles locations during the second exposure at time $t' = t + \Delta t$ will be given by:

$$\mathbf{X}'_i = \mathbf{X}_i + \mathbf{D} = \begin{pmatrix} X_i + D_X \\ Y_i + D_Y \\ Z_i + D_Z \end{pmatrix} \quad (4.7)$$

Additionally, assuming a simplification of the perspective projection that is valid only for particles located in the vicinity of the optical axis, the particles image displacements are given by (4.8), where M is the magnification factor.

$$\mathbf{d} = \begin{pmatrix} MD_X \\ MD_Y \end{pmatrix} \quad (4.8)$$

Figure 4.3 illustrates the image intensity field in an interrogation area at two consecutive recorded frames. As explained before, the size of the interrogation area has to be properly chosen in order to have enough particles inside the interrogation area in the two frames, as particles that leave the interrogation area will not contribute to the cross-correlation analysis.

The image intensity field is defined as:

$$I_g(\mathbf{x}, \boldsymbol{\Gamma}) = \sum_{i=1}^N V_0(\mathbf{X}_i) \tau(\mathbf{x} - \mathbf{x}_i) \quad (4.9)$$

where $V_0(\mathbf{X}_i)$ is the interrogation volume of a particle i (describes the shape, extension and location of the actual interrogation volume) and $\tau(\mathbf{x} - \mathbf{x}_i)$ is the point spread function of imaging lens.

The mean value of an image for a particular interrogation area (IA), in a time t , is determined by cross-correlating the image intensities of that IA at times t and t' . The cross-correlation is defined as:

$$R_{II}(x, y) = \sum_{j=-K}^K \sum_{i=-M}^L I_g(i, j) I'_g(i + x, j + y) \quad (4.10)$$

where I_g and I'_g are the image intensity fields in the first and second image respectively. Essentially the template I_g is linearly *shifted* around the sample I'_g without extending over edges of I'_g . For each choice of sample shift (x, y) , the sum of the products of all overlapping pixels intensities produces one cross-correlation value $R_{II}(x, y)$. By applying this operation for the range of shifts, a correlation plane of size $(2M+1) \times (2N+1)$ is formed. Basically the cross-correlation function statistically measures the degree of match between the two samples for a given shift. The highest value in the correlation plane is used to estimate the particle image displacement.

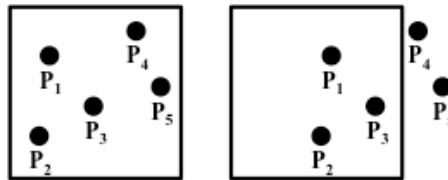


Figure 4.3: Image intensity field in an interrogation area, at two consecutive recorded frames

An example of the formation of a correlation plane is shown in Figure 4.4, where a 4x4 pixel template is correlated with a larger 8x8 pixel sample to produce a 5x5 correlation plane.

The correlation signal is strongly affected by variations in image intensity, as the correlation peak is dominated by brighter particles images with weaker particle images having a reduced influence. Also the non-uniform illumination of particle image intensity, due to light-sheet non-uniformities, in addition to the irregular particle image shape, out-of-plane motion, etc. introduce noise in the correlation plane. Consequently, image enhancement before the processing is usually advantageous. The main goal of the image pre-processing is to enhance particle image contrast and to bring particle image intensities to a similar signal level such that all particle images have a similar contribution in the correlation function.

The image pre-processing has been performed using the ImageJ software (Rasband, 1997). ImageJ is an open source code written in Java, which can be run on Linux, Mac OS X and Windows. It has an extended community of users, and it supports a wide range of image file formats, allowing the user to work with image sequences, so it is possible to process all the images obtained in a PIV as a package.

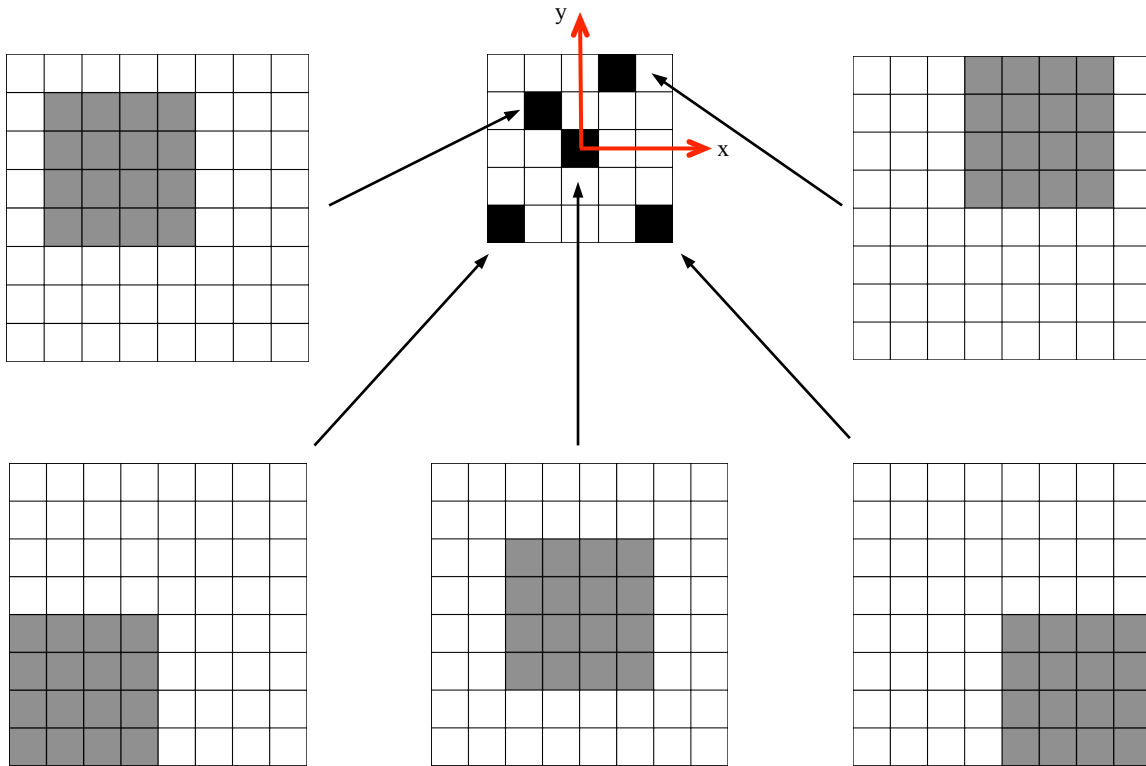


Figure 4.4: Example of the formation of a cross-correlation plane by direct cross-correlation

Among the available image treatments, the *subtract background* option has been chosen. It reduces the effects of the laser flare and other stationary image features. The resulting image after the filtering through the background subtracting is shown in Figure 4.5, where the filter is applied in a frame corresponding to the maximum area chamber of the pump.

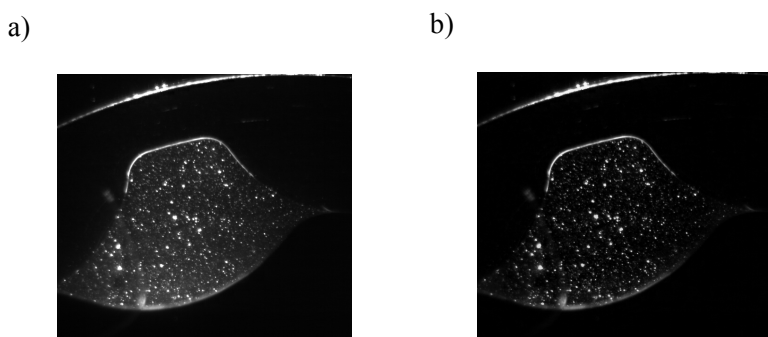


Figure 4.5: Image pre-processing. a) Original image. b) Subtract background treatment

4.8 Software

Table 4.4 summarizes the software in the process of experimental study by means of PIV.

Data acquisition	Camera's own control software: Photron FASTCAM Viewer
Image pre-processing	ImageJ (open source)
Image interrogation	GPIV and Scilab (both open source)
Post processing	Scilab (open source)
Graphical representation	Matlab

Table 4.4: Software used in the experimental study

4.9 Experimental arrangement

4.9.1 Test bench

The pump has been experimentally studied with Time-resolved PIV (TRPIV) in a test bench. In this section, the experimental setup and the main characteristics of each of its parts will be explained.

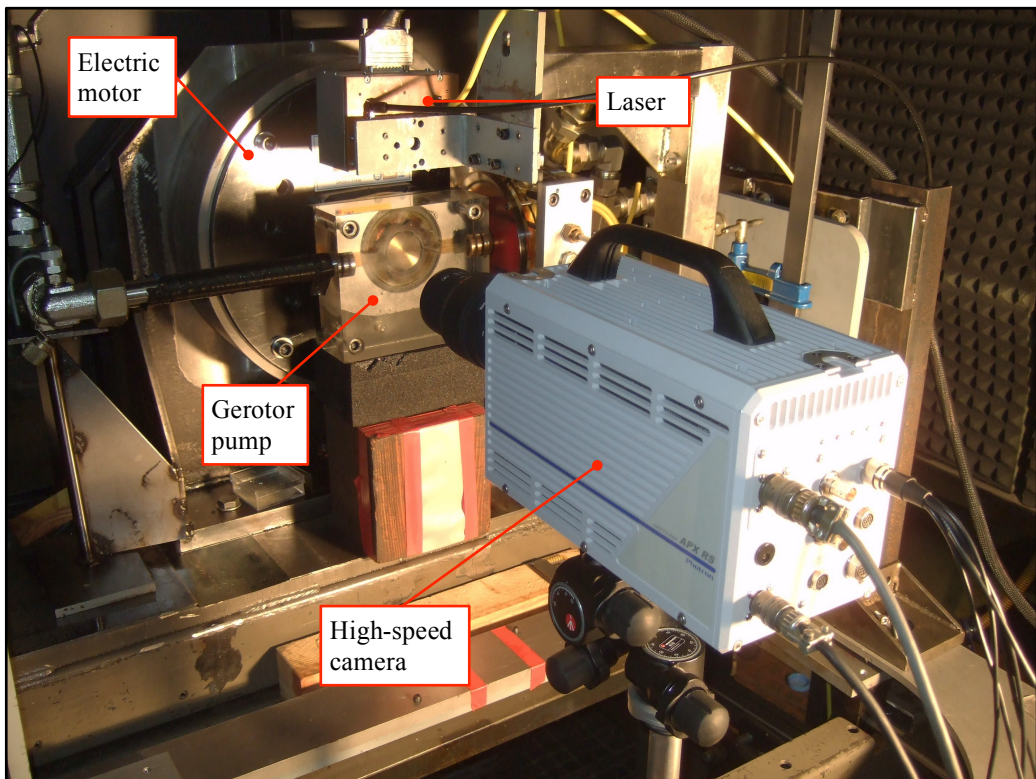


Figure 4.6: Installation of the pump in the test bench

Due to the chosen experimental technique, it has been necessary to modify the casing of the pump and the outer gear wheel, in order to allow light to cross the chambers where the flow has to be filmed. These two parts were substituted by new ones made in methacrylate (see Figure 4.8), which were made by Carlos Río, from the Mechanical Department (Universitat de Politècnica de Catalunya, Campus Terrassa). The installation of the pump in the test bench is shown in Figure 4.6. A detailed view of the experimental Gerotor pump is given in Figure 4.7.

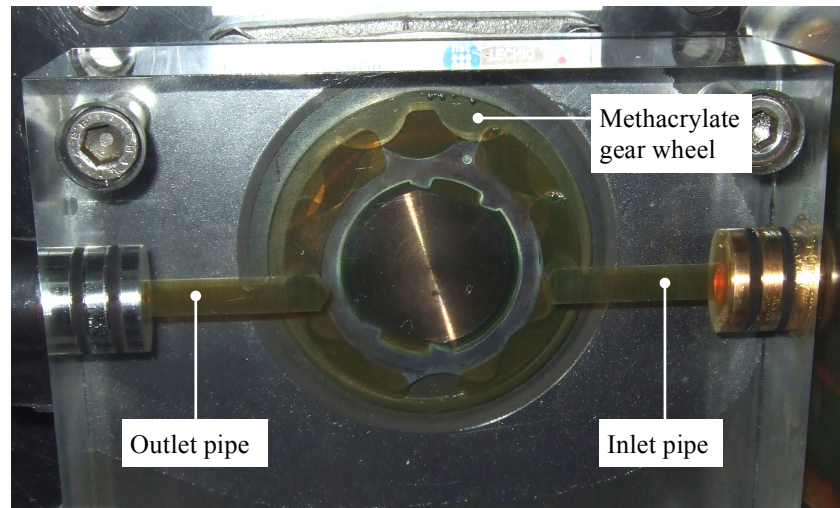


Figure 4.7: Detailed view of the Gerotor pump in the test bench

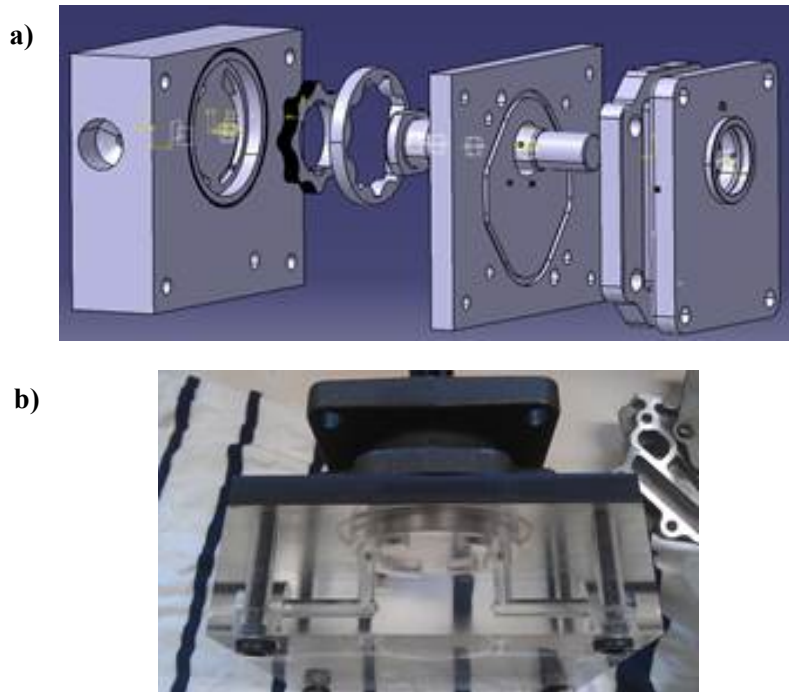


Figure 4.8: Methacrylate chasing. a) 3d CAD. b) Image of the assembly.

About the refractive indexes of the fluid and of the methacrylate pieces, they have not been determined in the present study. This will be done in future work, as it is not a priority in the present study. As it is not checked that the two refractive indices are matched, we cannot guarantee that there is no distortion in the particle image.

The pump has been tested following the assembly shown in Figure 4.9. In addition to the pump and the oil tank, a pressure-limiting valve is added in the discharge of the pump. The tank is situated 1 m above the pump, and no additional pressure is imposed in the discharge of the pump. The estimated pressures in the suction and discharge connections are 0.1 and 0.2 bar (gauge), respectively. These data have been taken into account in order to adapt the pressure of the boundary conditions in the CFD simulations.

4.9.2 Operating conditions

In order to establish the rotary velocity during testing, some previous considerations about the temporal and spatial resolutions have to be defined. The following justifies the selection of these resolutions, and derives the maximum rotary velocity to perform the experimental study.

The high-speed digital camera allows recording up to 250000 fps, but at very low spatial resolution (128x16 pixel). The selection of the temporal resolution of the experimental testing has been done selecting the maximum available frame rate at full resolution. The Photron Ultima APX-RS has a maximum spatial resolution is 1024x1024 pixel, and for this resolution the maximum available frame rate is 3000 fps. For these conditions the buffer memory of the camera allows to record up to 2048 images.

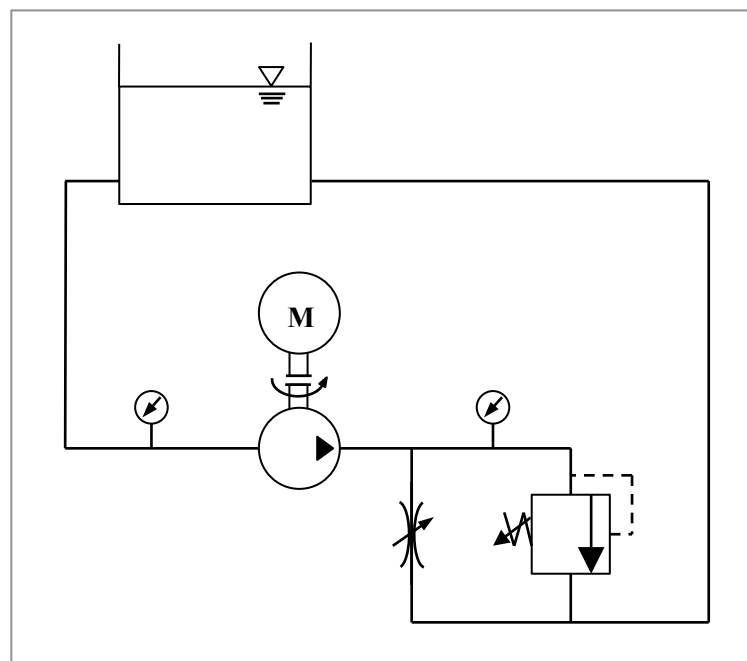


Figure 4.9: Experimental hydraulic circuit

High velocity camera	
Frame rate	3000 fps
Spatial resolution	1024x1024 pixel
Record time	0.7 s / 2048 frames
Laser	
Pulse length	50 µs
Beam dimensions	12 x 0.7 mm at output
Synchronizer	
Waveform	Square
Mode	Continuous
Frequency	3kHz
Symmetry control	50%
Output level	5Vp-p
DC offset	0.0V
Operating conditions of the pump	
Rotatory velocity of the pump (inner wheel)	250 rpm
Suction/ discharge pressure	0.1/0.2bar
Properties of the mineral oil	
Viscosity	$2.8 \cdot 10^{-2}$ Pa·s
Density	885 kg/m ³
Tracer particles concentration	0.375g/L

Table 4.5: Characteristics of the experimental testing

The size of the interrogation areas during evaluation must be small enough for the velocity gradients not to have significant influence on the results. Furthermore, it determines the number of independent velocity vectors and therefore the maximum spatial resolution of the velocity map, which can be obtained at a given spatial resolution of the sensor, employed for recording. According to the PIV bibliography and the recommendations in the software's user guide, the size of the interrogation area has been defined as 32x32 pixel.

The maximum rotary velocity (inner gear wheel, expressed in rpm), is defined in equation (4.11):

$$\omega_{i,max}[\text{rpm}] = \frac{20 \cdot IA \cdot SC[m] \cdot TS[\text{fps}]}{D_{ei}[m]\pi} \quad (4.11)$$

where IA is the size of the interrogation area (32x32 pixel), SC is the spatial scale (0.035 mm), TS is the time scale (3000 fps) and D_{ei} is the external diameter through the tips of the teeth of the inner gear (65.45 mm). Equation (4.11) leads to a maximum internal rotary velocity of approximately 327 rpm. Considering this maximum value, and defining the operating rotary velocity as the 75% of this maximum value, the selected value corresponds to 250 rpm.

4.10 Experimental Results

The TRPIV has been used in order to obtain the velocity field in two sections of the pump: the outlet pipe and the maximum area chamber. The evaluation of the experimental data by means of GPIV provides the two components of velocity for each of the coordinates contained inside the validation area. GPIV is a Graphic User Interface program for the interrogation, validation and post-process of the PIV data. It is an open source code created by Van der Graaf (Van der Graaf, 2004).

The flow ripple in the outlet pipe can be obtained integrating the velocity vectors that cross a plane perpendicular to the axis of the outlet tube. This is done in Scilab, and the result is shown in Figure 4.10, for the complete set of recorded frames. This same procedure is used in the maximum area chamber vector field, for a vertical plane centred in the width of the chamber. The resulting flow pulsation can be seen in Figure 4.11.

Figure 4.15 depicts the location of the interrogation area established for the evaluation of the experimental recorded frames. Note that in the case of the maximum area chamber frame, this particular position corresponds with a rotation of the outer angle of 270 degrees.

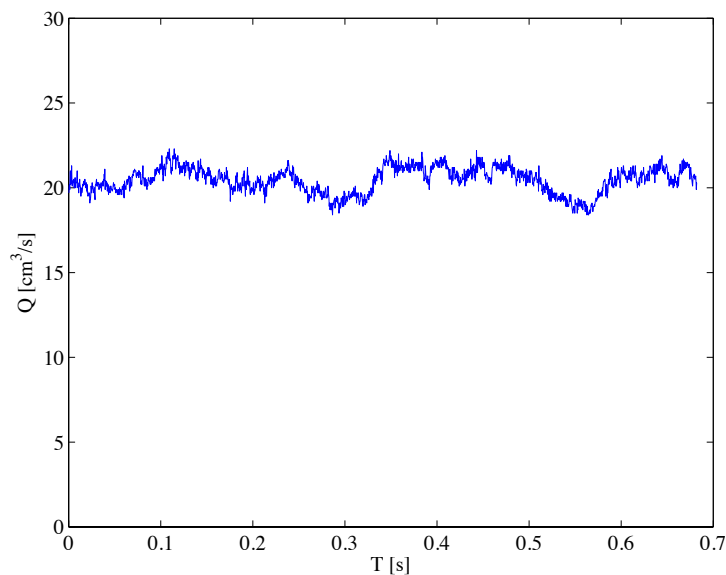


Figure 4.10: Experimental instantaneous flow in the outlet pipe.

The experimental results have been graphically represented in order to ease the understanding of the fluid behaviour inside the pump. In the present work, this graphical representation is done in Matlab R2013b, as it incorporates the functions to represent velocity contours and vector field.

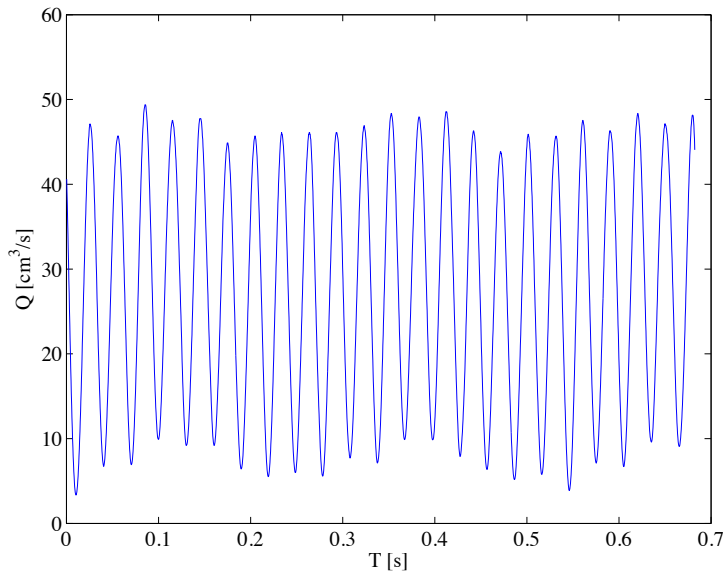


Figure 4.11: Experimental flow pulsation in the maximum area chamber

The velocity vector field is depicted in Figure 4.12. As it was expected, the resulting velocity profile is symmetric and the maximum values of velocity are located in the surroundings of the axis of the pipe. The contours of velocity are displayed in Figure 4.13 in connection with the velocity vector field.

Figure 4.14 shows the velocity vectors in three particular planes in the outlet pipe. It can be seen that the velocity profile is parabolic, as it was expected due to the low rotary velocity (250rpm) and the value of the Reynolds number of 183, showing a laminar flow.

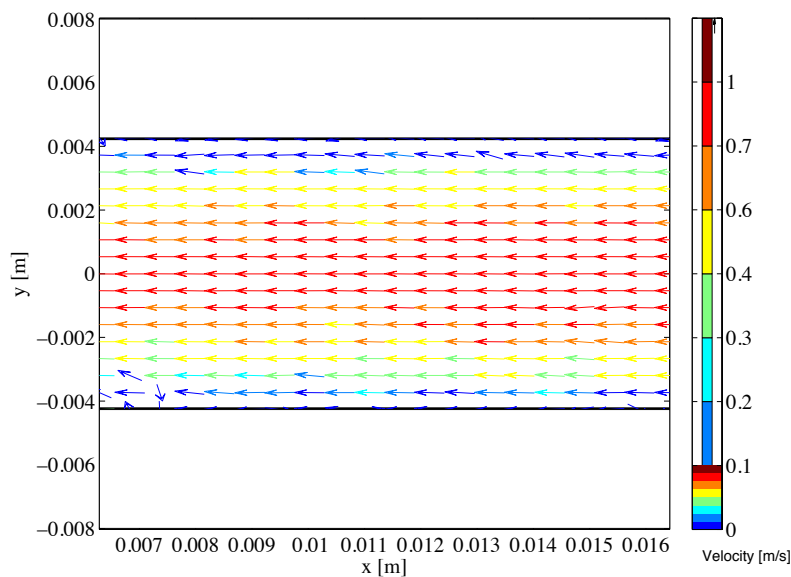


Figure 4.12: Experimental velocity vector field in the outlet pipe

Figure 4.16 presents the graphically depiction of the experimental results, belonging to the maximum area chamber, for a rotation angle of the outer gear of 90° , with respect to its reference position. It contains the velocity vector field representation, as well as the contours of velocity in connection with the velocity field. Finally, the vector velocity field obtained through PIV measurements is compared with the one calculated by means of the CFD simulation. Figure 4.17 and Figure 4.18 represent the experimental results of the maximum area chamber for a rotation angle of the outer gear of 180° and 270° , respectively.

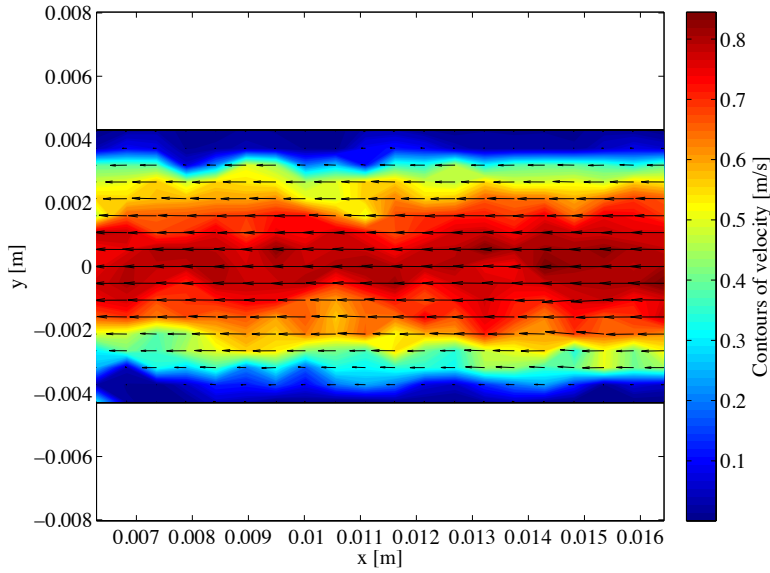


Figure 4.13: Experimental velocity contours and vector field in the outlet pipe.

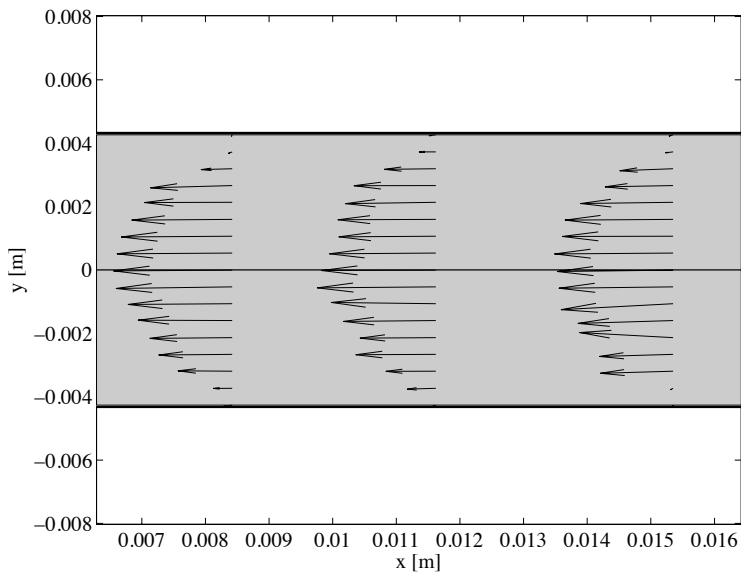


Figure 4.14: Example of experimental velocity vectors in the outlet pipe.

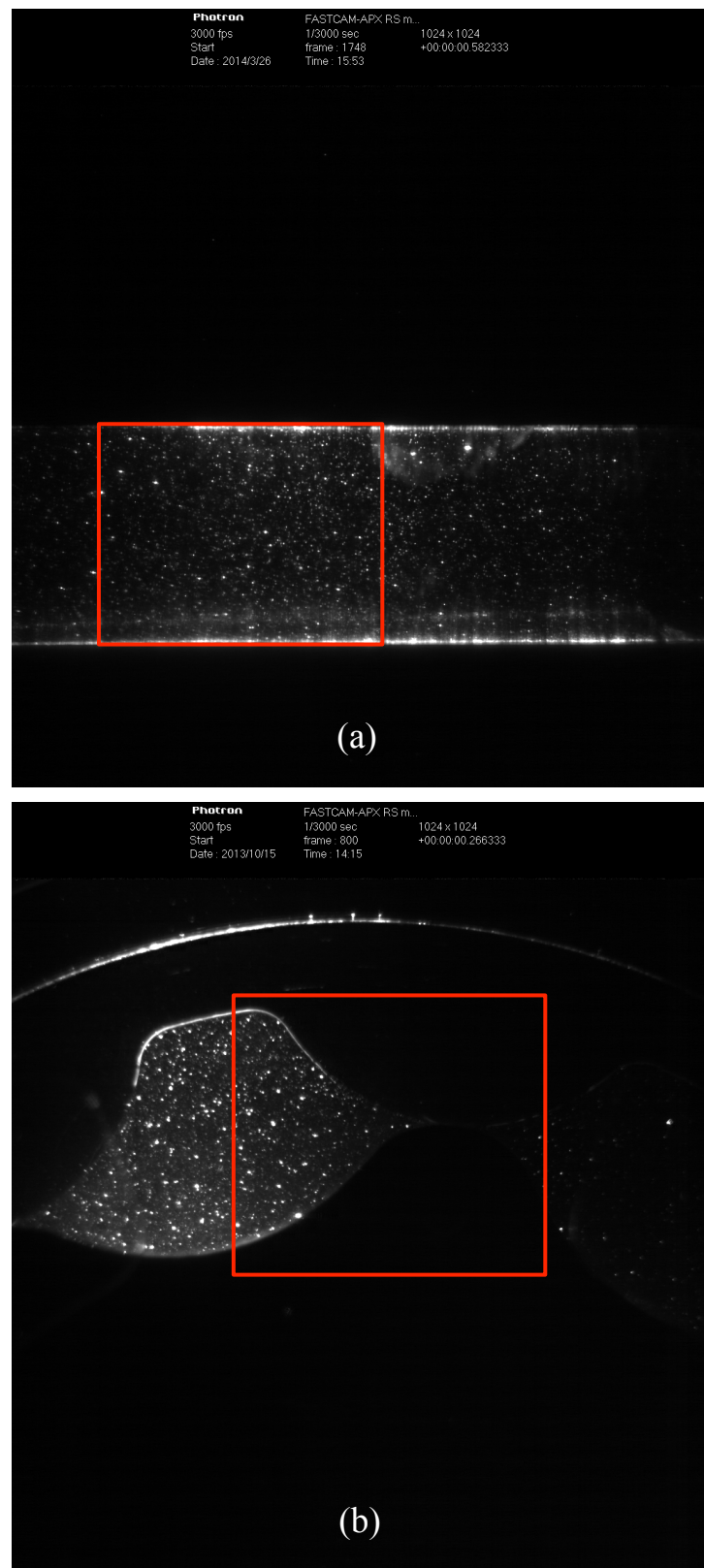


Figure 4.15: Location of the interrogation area: a) Outlet tube and b) Maximum area chamber ($\omega_e=270^\circ$)

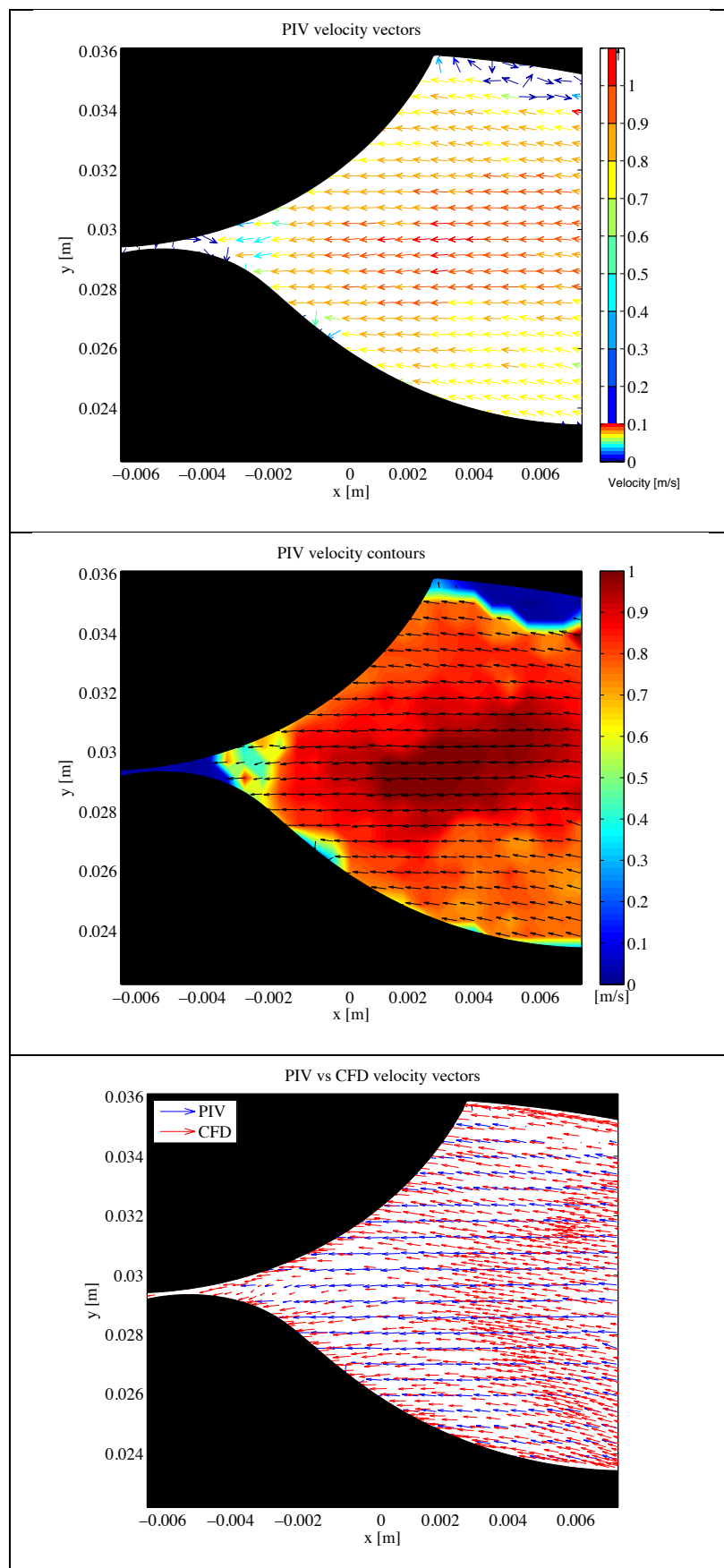
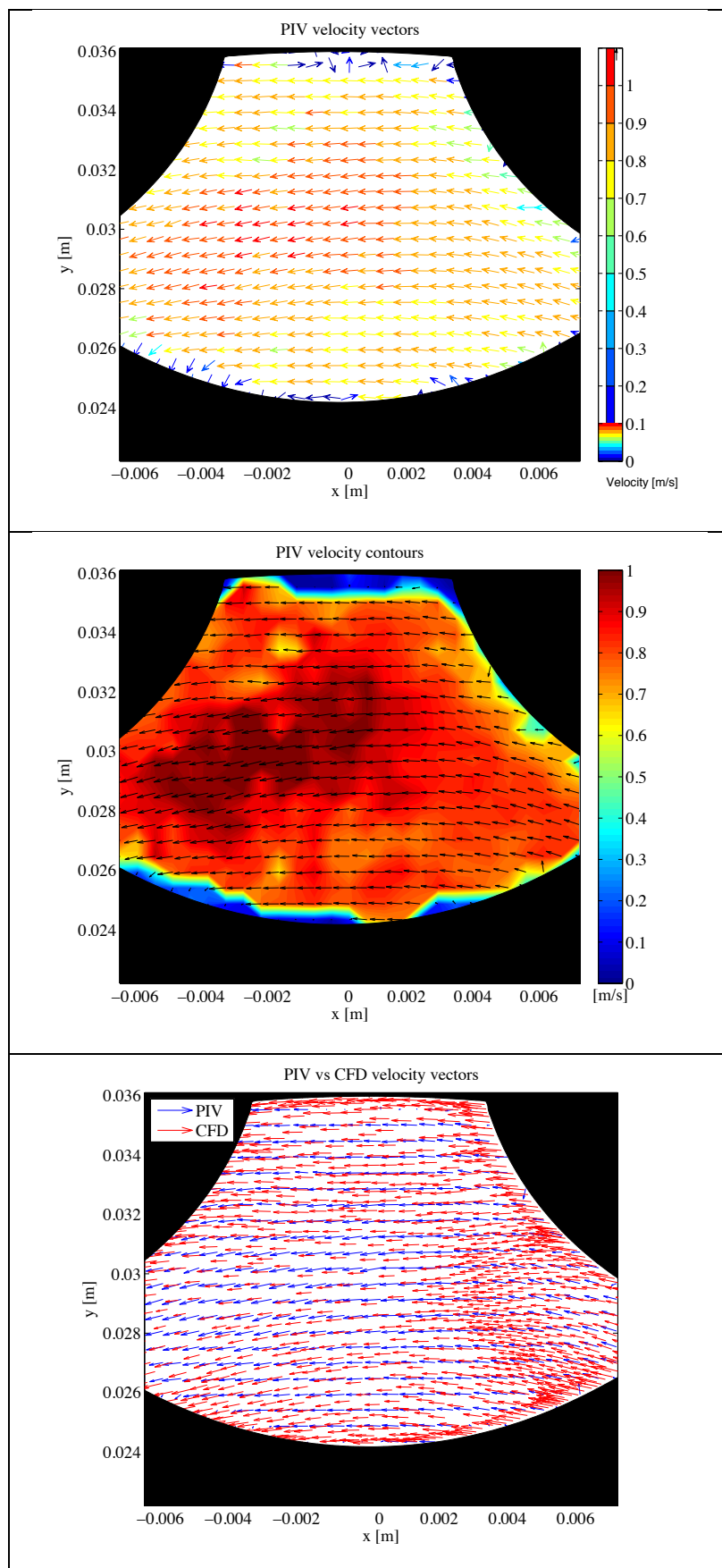


Figure 4.16: PIV experimental results for $\omega_e=90^\circ$

Figure 4.17: PIV experimental results for $\omega_e=180^\circ$

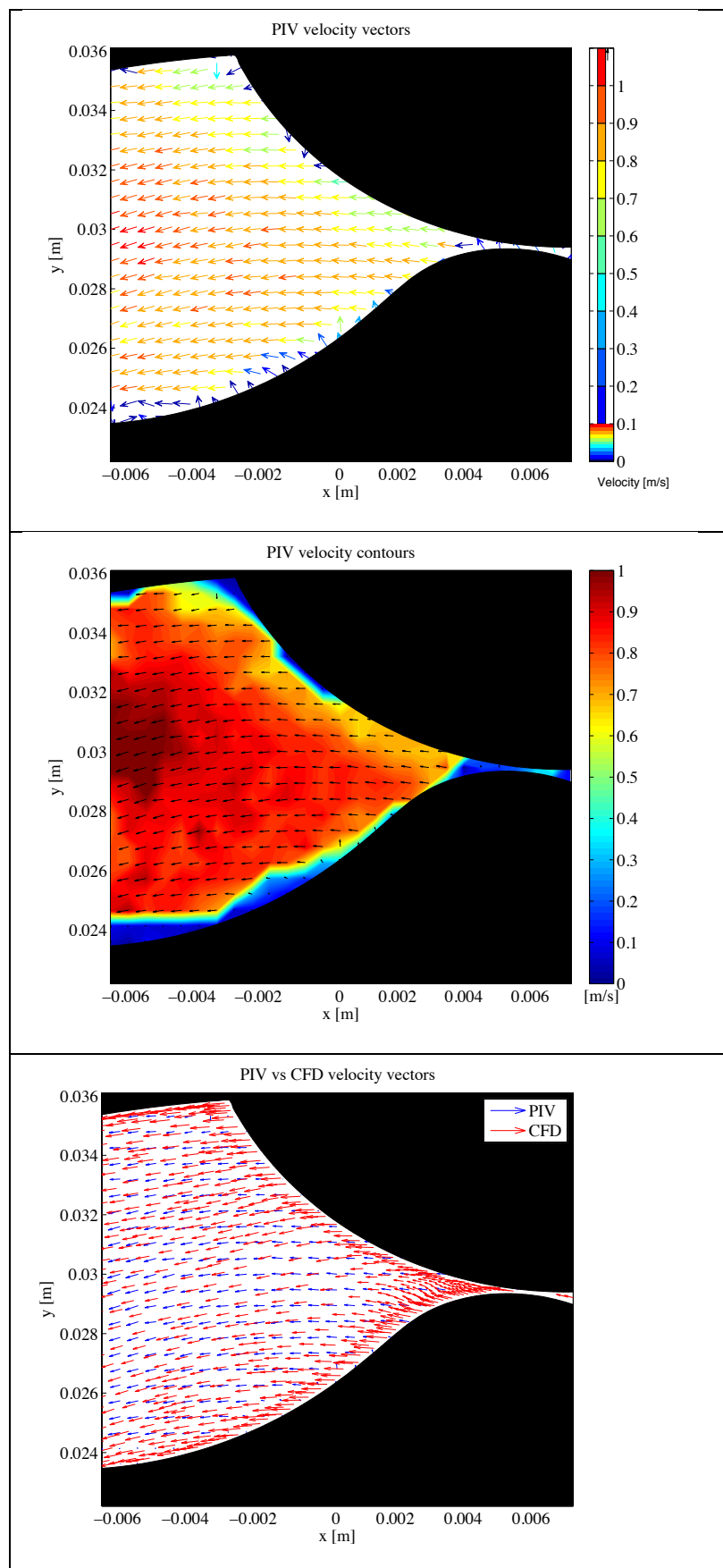


Figure 4.18: PIV experimental results for $\omega_e=270^\circ$

4.11 Evaluation of Experimental Results

With respect to the understanding of the comparative between experimental and simulation results, it must be taken into account that the experimental study has been performed in a gerotor pump made of methacrylate. In addition, the diameter of the chasing has been increased with respect to the original pump, in order to reduce wear of the outer gear wheel.

On the one hand, as studied by Biernacki (Biernacki et al., 2009), from the viewpoint of hydraulics, during the pumping action the condition of deformations is more important than the condition of stresses. This is so because, by keeping the stresses lower than the acceptable, it is at the same time possible to achieve deformations and clearances greater than the extreme, which causes flaws in the pumping process, as well as lowering of the working pressure and pump efficiency. On the other hand, the increase in the clearance between outer gear and chasing results in a higher leakage flow.

As a consequence, the results of the numerical simulation and experimental results cannot be compared directly, as there is more leakage in the tested pump, due to increased clearance and deformation in the methacrylate parts. In order to be able to compare the results, the discharge pressure imposed in the CFD simulation has been increased, to force the case to increase leakage flow, thus equalling the flow in the outlet pipe between experimental and simulation results.

In order to characterise the type of flow in the present study, a Reynolds number is defined as:

$$Re = \frac{\rho v d_o}{\mu} = \frac{4\rho Q}{\mu \pi d_o} \quad (4.12)$$

where ρ and μ are the density and dynamical viscosity of the fluid

v and Q are the average velocity and the flow rate at the outlet pipe

d_o is the diameter of the outlet port pipe

In the present case, for the rotational velocity of 250 rpm, and considering the theoretical flow, the Reynolds number is $Re \approx 183$ that is value showing a laminar flow condition.

The results of the numerical simulations show the instantaneous flow of the gerotor pump related to time. These results are presented in the figures by using the normalized values of flow Q/Q_g and time T/T_g . The instantaneous flow Q is normalized with the theoretical instantaneous flow Q_g , and it can be calculated as:

$$Q_g = \omega_i \cdot c_v \quad (4.13)$$

where ω_i is the rotational velocity of the shaft connected to the inner gear and c_v is the theoretical volumetric capacity. Replacing the two variables with their values (Table 3.2) in equation (4.13), the resulting theoretical instantaneous flow is $4.08 \cdot 10^5 \text{ m}^3/\text{s}$.

The time has been normalized with the gearing period T_g , which is the time that is needed for the tooth meshing to be repeated. CFD results have been obtained by simulating complete rotations of the gear set to reach flow stabilization.

$$T_g = \frac{1}{\omega_i \cdot (Z - 1)} \quad (4.14)$$

where ω_i is the rotational velocity of the shaft connected to the inner gear and Z is the number of inner teeth. Replacing its values (from Table 3.2) in equation (4.14), T_g takes a value of $4.78 \cdot 10^{-3} \text{ s}$.

The present section contains the results of the simulations and experimental study performed in the gerotor pump. These results are focused in the evaluation of the two main performance indexes, the volumetric efficiency and the flow irregularity.

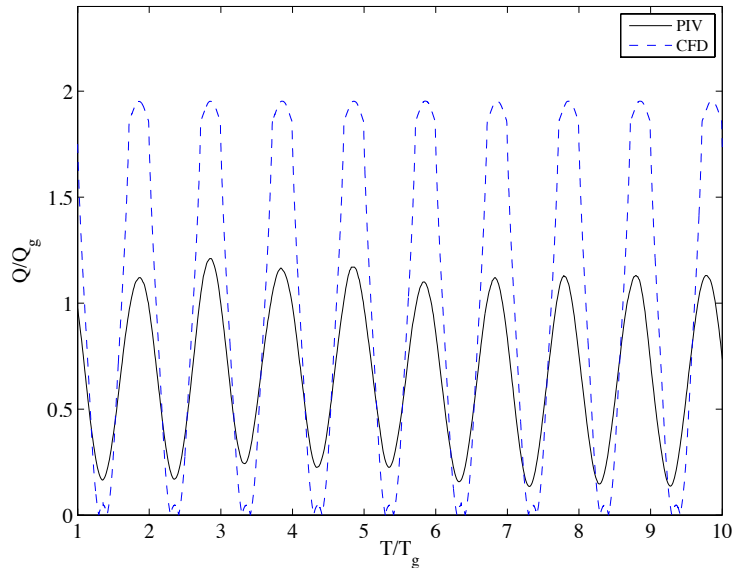


Figure 4.19: Comparative of the flow in the maximum area chamber.

The analytical calculation of the volumetric capacity index is obtained by means of the *Volumetric Characteristics Module* of GeroLAB Package. The geometrical parameters of the studied pump are used as inputs for this module and the resulting value of the volumetric capacity is $9.80 \text{ cm}^3/\text{rev}$. This theoretical volumetric capacity is used in the calculation of the theoretical instantaneous flow.

The volumetric capacity is obtained through the BondGraph dynamical simulation, by means of the variation of the chambers volume for a complete rotation of the pump, and it does not include the leakage flow, resulting in a value $9.53 \text{ cm}^3/\text{rev}$.

Figure 4.19 shows the evolution of the flow in the maximum area chamber for the experimental study and the numerical simulation. By integrating the total amount of fluid flow in the maximum area chamber the results are, for the experimental and numerical curves, respectively, 7.3 and $10.6 \text{ cm}^3/\text{rev}$. In the case of the experimental value, the volumetric capacity is reduced due to the leakage between trochoidal profiles and the leakage flow between the gears and the chasing of the pump. Note that the volumetric capacity resulting of the numerical simulation is higher than the theoretical one, which would be physically impossible. The reason is that the flow evaluated contains the leakage effects. What is really interesting of observing Figure 4.19 is that there is a clear correspondence between the experimental and the numerical results, as the two flow responses have the same tendency, both having the same order of magnitude.

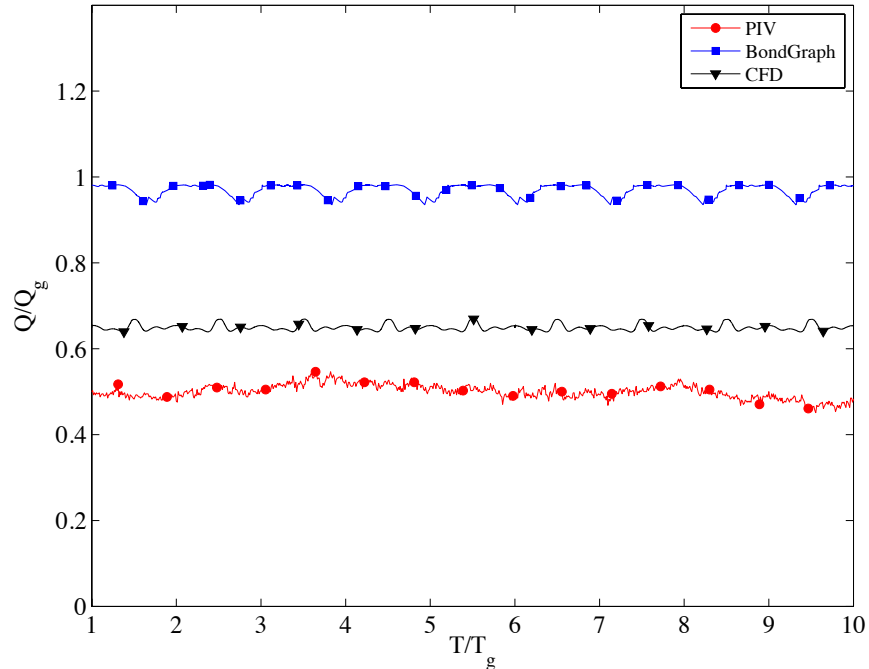


Figure 4.20: Comparative of the flow in the discharge tube.

The instantaneous flow in the outlet pipe has been simulated by means of the BondGraph dynamical model and the numerical simulation of CFD. In addition, it has been experimentally studied through the TRPIV technique. Figure 4.20 shows its results, for a rotating velocity of 250 rpm and with inlet and outlet pressures of 0.1 and 0.2 bar, respectively, for the dynamical simulation and the experimental study. As explained before in this chapter, the discharge pressure has been adapted in the

numerical simulation, increasing its value in order to adjust the leakage in the simulation to the real tested pump. As it was expected, the BondGraph results are near the theoretical average flow rate, and have an irregularity index of 4.80%.

About the correspondence between the numerical simulation and the experimental results, it can be stated that the CFD model describes properly the fluid-dynamic response of the pump. The flow irregularity is of 4.7% for the numerical simulation and 19.07% for the experimental measurements. Despite this discrepancy, it must be highlighted that the two curves have the same order of magnitude, and this difference could be probably explained by the effects of testing with a gearing mechanism made of methacrylate, as previously exposed.

To finish the present chapter, we can conclude that experimental study of the gerotor pump by means of Time-Resolved Particle Image Velocimetry has been proved as a new useful tool of estimation of the fluid-dynamic behaviour of the pump. In the present thesis qualitative evaluation of the experimental results has been carried out, while its quantitative evaluation is left to future work. In order to check the quantitative agreement of TRPIV with the theoretical models, it will be necessary a further development of this technique applied to the gerotor pump.

5 Final Conclusions and Future Work

5.1 Introduction to final conclusions

The present chapter reviews the main topics and procedures presented in this thesis. First, the limitations of the present work and the achieved progress are presented. Second, the final conclusions obtained in this work are exposed. Finally, suggestions about future work are given.

Chapter 1 presents the main objective of this thesis: to develop a set of design tools applied to trochoidal gear pumps, from the viewpoint of the fluid dynamical performance of the pump. Besides, it contains a brief introduction to Gerotor pumps and the state of the art.

In Chapter 2 the analytical study of the problem focused in the use of GeroLAB package is explained. It shows the two new modules created for GeroLAB, *Minimum Clearance Module* and *Effective Port Areas*. Finally, its applicability is exemplified in the dynamical simulation through the BondGraph technique, studying the influence of the port areas geometry.

Chapter 3 gives details about the numerical simulation of the problem, performed with the commercial code ANSYS FLUENT TM 12.0.16, based on the finite-volume method. First, it presents and justifies the selected numerical schemes and turbulence model: details are given about the spatial discretization and the time derivatives selected in the numerical simulation, and its convergence criteria. Additionally, the mesh properties are specified: the zones of the computational domain and the mesh deformation algorithm are defined. Also, the mesh quality analysis and grid independence study are exposed. Special attention is dedicated to the simulation of the solid contact between the gears: the new strategy called *Gearing Contact Point* that includes the calculation of the theoretical contact point is detailed, and its advantages are exposed. The structure of the code integrated in the commercial algorithm and the condition imposed in the contact point zone are explained.

Chapter 4 exposes the experimental study by means of Time-Resolved Particle Image Velocimetry (TRPIV), containing the principles of this non-intrusive technique and details about the selection of its main parts. First, the criteria taken into account for the selection of the tracer particles are discussed, and

the main characteristics of the used camera, laser and synchronizer are given. Later, the basis of the mathematical background of statistical PIV evaluation is explained, and the test bench and the operating condition of the experimental arrangement are described. It also includes the main experimental results and its evaluation. All results are presented by using the normalized values of the flow and time, in order to make easier its interpretation.

5.2 Limitations of the present work

The experimental study has been performed in a Gerotor pump made of methacrylate, as it was required in order to be able to film the flow inside the pump. Besides, the tolerance between the outer gear and the chasing of the pump has been increased, in order to reduce wear between these two moving parts. Consequently, the working pressure of the experimental pump is quite far from being in the normal operation pressure range of this type of pump, and internal leakage of the pump is strongly increased.

In order to adapt the numerical simulation to the experimental conditions, the discharge pressure has been adjusted, to equalize the simulated and experimental flow in the outlet pipe of the pump. Also, as a consequence of the limited velocity of rotation of the experimental arrangement, the numerical simulation model has been validated only for the laminar case.

Another simplification of the numerical simulations is that the centres of the gears have been considered as fixed during the simulation. Its relative movement has been neglected, in order to simplify the simulation and because of the minor displacement that this effect could produce.

The BondGraph dynamical simulation contains simplifications regarding some leakage submodels and consequently it gives more idealized results compared with the numerical simulation or the experimental results.

5.3 Progress achieved

The main progresses achieved in the work presented in this thesis are the following:

- Development of a 3D CFD model, containing leakage phenomena. It allows the prediction of the fluid-dynamical behaviour of the fluid in the insights of the pump. It includes the creation of the *Gearing Contact Point* strategy, to simulate the solid contact point between trochoidal profiles, and the study of the influence of simulating the contact points is also developed. The calculation of the volumetric efficiency can be obtained by integration of the simulated flow in

the maximum area chamber, while the irregularity index can be determined through the velocity field in the outlet pipe.

- Two new modules of GeroLAB Package: *Minimum Clearance Module* and *Effective Port Areas Module*. The first one allows the calculation of the minimum distance between the trochoidal profiles taking into account the manufacturing tolerances and the second one provides the area to which a chamber is exposed in the suction or discharge zones, considering the restriction imposed by the geometry of the port areas.
- BondGraph dynamical simulation model: the integration of the results provided by the two new GeroLAB modules constitute and advance in the dynamical approach of the problem, as they suppose a more realistic approach in the BondGraph dynamical simulation.
- Experimental procedure to study Gerotor pump: the selection of particles and its concentration, devices for the data acquisition and PIV tools to perform the data treatment. In addition, the creation of a procedure of results interpretation and optimization is done. Also, the volumetric efficiency can be evaluated through the velocity field obtained in the maximum area chamber. The instantaneous flow has been determined by means of the measured velocity field in the outlet pipe and the maximum area chamber. First one is useful for the calculation of the irregularity index while the second one serves for the obtaining of the volumetric efficiency of the pump.

5.4 Final Conclusions

Final conclusions of the present thesis are separated in the main strategies to which they belong: simulation, analytical or experimental study.

From the viewpoint of the numerical simulation:

- A 3D numerical model considering leakage and manufacturing tolerance has been created. It has been used for the qualitatively evaluation of the TRPIV experimental data obtained at a rotary velocity of the pump of 250 rpm. This velocity is the maximum possible to have reliable results with the available experimental resources. The comparison shows a good agreement, as both the simulation and experimental results have the same tendency in the flow behaviour, and they are of the same order of magnitude. The existing differences can be explained by the effects of testing with a gearing mechanism made of methacrylate.
- The *gearing contact point* strategy represents a reduction of the 40% of the calculation time, with respect to the previous strategy named *viscous wall-cell*. This has been possible thanks to the incorporation of the theoretical calculation of the contact point in the user-defined function

(UDF) that defines the solid contact points between trochoidal gears. Besides, this new UDF gives the value of the minimum radial clearance between teeth.

- The mesh quality analysis results in a maximum value of the area-averaged equivolume skewness of 0.89 for both the inter-profile surfaces, being less than the value of 1 defined for a good mesh quality deformation. Besides, the grid independence study, performed in simulations with a mesh of about $0.6 \cdot 10^6$ and $1.2 \cdot 10^6$ cells, shows a maximum error between them of a 0.17%, regarding the mean normalized flow.
- Numerical simulations have been performed as laminar, due to the experimental limitations, performed at low rotational speed (250rpm) having a low Reynolds number ($Re \approx 183$). Nevertheless, a comparative between the computations of the same case by means of laminar and turbulent model evidences that is not necessary to use a turbulent model (computationally more costly than the laminar model), as the maximum relative deviation is of 0.86% between the results obtained through the two models, respect to the instantaneous flow in the outlet pipe.
- The study of the influence of the teeth contact has shown this approach to be significant and it is proved that the *Gearing Contact Point* strategy establishes a more realistic leakage flow model in the interteeth clearances.

From the viewpoint of the analytical and dynamical simulation tools:

- The *Effective Port Areas Module* results have been included in the BondGraph dynamical simulation, making it more realistic. For the studied geometries, it has been seen that some of them produce a significant quantitative reduction of the irregularity flow index that can be almost about 12%. Thanks to these results, it is possible to establish constructive relations between the differences in design and the response provided by the pump flow.
- The *Minimum Clearance Module* is the first of the modules included in the GeroLAB package that takes into account real effects of the manufacturing tolerance. The progression of the minimum distance between the outer and inner teeth from the reference position of the gear is obtained.

From the viewpoint of the experimental study:

- The experimental study by means of Time-Resolved Particle Image Velocimetry has established a methodology for the accurate determination of velocity fields inside the pump, as seen thanks to the comparison with the numerical simulation.
- The experimental pump has been appropriately adapted to the experimental technique requirements: the casing and the gear have been made of methacrylate and tolerances between

the moving pieces have been increased, in order to be able to film the tracer particles and to reduce wear, respectively.

- Tracer particles have been properly selected: alginate particles present excellent flow seeding and light scattering abilities. They ensure good tracking of the fluid motion, thanks to their porous structure that easily absorb the analysing fluid. Also, they do not cause any damage to the inner contact surface of the pump.
- The volumetric behaviour of the pump has been evaluated through the measured flow in the maximum area chamber. Results show a clear correspondence between the experimental and the simulation behaviour, as they both have the same tendency and they are of the same order of magnitude.
- The flow ripple has been experimentally determined and compared with the numerical simulation: a good agreement between the two curves has been found, as they show the same tendency and both have the same order of magnitude.
- The flow irregularity has been experimentally determined in the outlet pipe, showing a good agreement with the numerical simulation. The CFD model describes properly the fluid-dynamic response of the pump, as the deviation in the average flow is between both strategies is about 4%. The flow irregularity is of 4.7% for the numerical simulation and 19.07% for the experimental measurements. Despite this discrepancy, the two curves have the same order of magnitude, and this difference could be probably a consequence of the modification in the material and dimensions of the pump, which have produced deformations in the gear and higher leakage flow.

As a final remark, the highlights of the research presented in this thesis are discussed in the following compared with the main authors that cover each of the main topics. They involve a considerable advance in the study and characterization of gerotor pump, compared to the documented work related to internal gear pumps up to date.

The most widely used methodology to measure the flow ripple of positive displacement pumps was first described by researchers at University of Bath (Edge and Johnston, 1990). Named Secondary Source Method, this test method for measuring the source flow ripple and source impedance is based on the analysis of the wave propagation characteristics in a circuit which includes the pump under test and an additional source of fluid-borne noise. Its main disadvantages are the complexity required for its implementation and the inaccuracies in the calculation of the flow ripple, as it is not measured directly but calculated with an algorithm thanks to the measurement of the pressure pulses.

The experimental procedure presented in this thesis meets the need of a methodology to directly measure the flow ripple generated by the pump, with a non-intrusive technique. It constitutes an alternative to the Secondary Source Method, and it is the first approach of Time-Resolved Particle Image Velocimetry (TRPIV) applied to a trochoidal gear pump, according to the author's knowledge.

TRPIV is also subject to inaccuracies in its development stage, as its results deeply depend in the correct choice of its characteristics parameters like the tracer particles, the material of the casing of the pump or the statistical determination of the particles' velocity through the cross-correlation analysis. The experimental work performed in this thesis is aimed to evaluate the possibility of establishing TRPIV as a tool for directly measure the flow generated by the pump, in a non-intrusive way, without adding any other components that modify its normal operation. Considering the results from the present work, TRPIV is proved to be a feasible alternative to obtain the instantaneous flow of the pump in a direct mode and without altering its behavior.

From the point of view of the numerical simulation, many authors have applied this technique to trochoidal gear pumps. Biernacki (Biernacki and Strycek, 2009) analyses the mechanism of induction of stresses and deformations in plastic cycloidal gears used in gerotor pumps by means of the finite element method and the commercial program ABAQUS. In this work no attention is focused to the manufacturing tolerances.

Suresh Kumar (Suresh Kumar and Manonmani, 2010) performed a three-dimensional transient simulation to optimize the design of the intake channel in a gerotor pump. The selected code is Cfdesign commercial software, a design-oriented CFD modelling code with a moving dynamic meshing capability. The paper details do not exhibit any evidence of simulating the teeth contact as a boundary condition.

Vacca and his team, from the Maha Fluid Power Research Center (Purdue University), use a CFD model as a part of the simulation tool HYGESim for the evaluation of leakage flow in the lubricating gap at gears' lateral sides and calculation of thrust forces.

Numerical simulation models that are found in the documented work do not integrate a complete leakage model that properly describes the real behavior of the pump. The CFD model presented in this thesis is planned to accomplish the objective of clarifying how leakage flow affects the response of the pump. Consequently, it includes manufacturing tolerances, thus allowing the study of their influence in the overall performance of the pump.

The boundary condition for simulating the contact points is established as a fluid-dynamic condition, while other authors that have focused their study in this phenomenon have addressed the problem exclusively in terms of the contract stress approach.

From the viewpoint of dynamics Professor Nervegna and his team, at Politecnico di Torino, carry out the most complete studies. They develop several 1D simulation models of positive displacement pumps in the LMS AMESim environment. In particular, very detailed studies have been carried out on gerotor pumps. All significant geometric quantities are calculated analytically as function of the shaft angular position and the current pump displacement. They include, among others, gears profiles and their line of contacts, chamber volume and its derivative, chamber inflow and outflow flow areas, kinematic (ideal) flow ripple.

Vacca and his team, from the Maha Fluid Power Research Center (Purdue University) created the simulation tool HYGESim. It is presented, with verification and design purposes, to perform the entire simulation of external gear machines considering main physical phenomena. It is a multi-domain simulation methodology, including the numerical evaluation of leakage flow in the lubricating gap at gears' lateral sides and the calculation of thrust forces. The simulation tool consists of different modules: a lumped parameter fluid dynamic model, a mechanical model for evaluation of the gears motion and a geometrical model.

Mucchi et al. (Mucchi et al., 2010) present a non-linear lumped kineto-elastodynamic model for the prediction of the dynamic behaviour of external gear pumps. They consider two main sources of noise and vibration: pressure and gear meshing. The model can be used in order to analyse the pump dynamic behaviour and to identify the effects of modifications in design and operation parameters, in terms of vibration and dynamic forces. They consider the pressure distribution on gears as time-varying and they state that it depends on the gear eccentricity. The gear eccentricity is calculated in the steady-state condition as a result of the balancing between mean pressure loads, mean meshing force and bearing reactions.

GeroLAB Package (used and improved in the present thesis), compared with the existing work, constitutes a useful tool to help the designer to improve performance indexes in a gerotor pump project. Nevertheless, it can be improved by adding more realistic approaches like adding the leakage phenomena.

The dynamical simulation by means of a BondGraph model, used in this thesis, is an alternative to the existing software. The main advantage of this type of modelization is that complexity can be added progressively to the system. Previous works have proved this model to be acceptable to properly describe the overall performance of the pump (Gamez-Montero and Codina, 2007). In the present thesis, the model has been improved by adding the information of the effective port areas, thus making it more realistic. Obviously, in this proposed model there are many open areas that have to be improved. For instance, the idea presented by Mucchi could be integrated to this model.

5.5 Future Work

The work presented in this thesis establishes a basis that provides the opportunity to simulate many variations of the geometry of the pump and its working conditions. These possibilities could lead to the following work:

- Use of the minimum radial clearance to assign the contact point at every time of the simulation, to achieve a more realistic approach.
- Study of the influence of manufacturing tolerances in the instantaneous flow and the leakage flow generated by the pump.
- Study the influence of the port areas geometry in the main performance indices of the pump. It has been observed that little variations in the port areas produce important differences in the flow ripple of the pump. It would be advantageous to focus on the parameters that produce reductions in the irregularity of the flow, in order to achieve the optimum geometry for the port areas.

About the limitations of the present work, the following could be some suggestions for improvement:

- Determine the discharge coefficient that characterizes leakage between trochoidal profiles (setting the suction and discharge pressure values, and without rotation of the pump): this information would be used to improve the BondGraph dynamical simulation, making the leakage modelling more realistic.
- Simulate the system not considering that the centres of the gears as fixed. This would show the effect of this relative movement, in the overall performance of the pump.
- Improvement of the TRPIV technique applied to gerotor pumps, in order to achieve its quantitative validation.

References

- Adrian, R.J. and Westerweel, J. *Particle Image Velocimetry*. Cambridge University Press, 2011. ISBN: 978-0-521-44008-0
- Ansdale, R.F.; Lockley, D.J. (1968). *The Wankel RC Engine Design and Performance*. London Iliffe Books LTD, pp 155.
- ANSYS Fluent 12.0 Theory Guide, 2009.
- ANSYS Fluent 12.0 UDF Manual, 2009.
- ANSYS Fluent 12.0 User's Guide, 2009.
- Beard J.E.; Yannitell D.W.; Pennock G.R. (1992). *The effects of the generating pin size and placement on the curvature and displacement of epitrochoidal gerotors*. Mechanism and Machine Theory, 1992; 27: 373-389.
- Biernacki, K.; Stryczek, J. (2009). *Analysis of stress and deformation in plastic gears used in gerotor pumps*. Journal of Strain Analysis for Engineering Design Vol.45 465-479.
- Bonandrini, G.; Mimmi, G.; Rottenbacher, C. (2011). *Design and simulation of meshing of a particular internal rotary pump*. Mechanism and Machine Theory 49 (2012) 104-116.
- Choi, T. H., Kim, M. S., Lee, G. S., Jung, S. Y., Bae, J. H., and Kim, C., (2012). *Design of Rotor for Internal Gear Pump Using Cycloid and Circular-Arc Curves*. Trans. ASME J. Mech. Des., 134(1), p. 011005
- Codina, E.; Khamastha, M.; Gutes, M.; Millanes, M. (1996). *Diseño de una Bomba de Engranajes Internos tipo Gerotor*. Journal of Mechanical Design ASME Transactions, pp 7.
- Colbourne, J.R. (1974). *The Geometry of Trochoid Envelopes and Their Application in Rotary Pumps*. Mechanism Machine Theory, Vol. 9, pp 14.
- Colbourne, J.R. (1975). *Gear Shape and Theoretical Flow Rate in Internal Gear Pumps*. Transactions of the Canadian Society for Mechanical Engineers, Vol. 3, Num. 4, pp 215-223.
- Colbourne, J.R. (1976). *Reduction of the Contact Stress in Internal Gear Pumps*. ASME Transactions, pp 5.
- Dasgupta, K.; Mukherjee, A.; Maiti, R. (1996). *Modeling and Dynamics of Epitrochoid Generated Orbital Rotary Piston LSHT Hydraulic Motor: a BondGraph Approach*. Journal of Manufacturing Science and Engineering, Transactions of the ASME, Vol. 118, pp 6.
- Dasgupta, K.; Mukherjee, A.; Maiti, R. (1996). *Theoretical and Experimental Studies of the Steady State Performance of an Orbital Rotor Low-Speed High-Torque Hydraulic Motor*. Proceedings of the Institution of

- Mechanical Engineers, Part A: Journal of Power and Energy, Vol. 210, pp 6.
- Devendran, R.S. and Vacca, A. (2013). *Optimal design of gear pumps for exhaust gas aftertreatment applications*. Simulation Modelling Practice and Theory 38 (2013) 1–19
- Ding H, Visser F C, Jiang Y and Furmanczyk M 2011 J. Fluids Eng. – Trans ASME 133(1) 011101
- Ding, H; Lu, X J; Jiang, B. (2012). A CFD model for orbital gerotor motor. 26th IAHR Symposium on Hydraulic Machinery and Systems
- Edge, K.A.; Johnston, D.N. (1990). *The 'Secondary Source' Method for the Measurement of Pump Pressure Ripple Characteristics. Part 2: Experimental Results*. Proc Institution of Mechanical Engineers Journal of Power and Energy, Vol. 204, pp 6.
- Edge, K.A. (1980). *The Theoretical Prediction of the Impedance of Positive Displacement Pumps*. Seminar on Quieter Oil Hydraulics, Institution of Mechanical Engineers, pp 95-103.
- Edge, K.A. (1983). *The Use of Plane Wave Theory in the Modelling of Pressure Ripples in Hydraulic Systems*. School of Engineering, University of Bath Trans Inst M C, pp 8.
- Edge, K.A.; Johnston, D.N. (1986). *A New Method for Evaluating the Fluid Borne Noise Characteristics of Positive Displacement Pumps*. Seventh International Symposium on Fluid Power, Bath, pp 253-260.
- Edge, K.A.; Johnston, D.N. (1990). *The 'Secondary Source' Method for the Measurement of Pump Pressure Ripple Characteristics. Part 1: Description of Method*. Proc Institution of Mechanical Engineers Journal of Power and Energy, Vol. 204, pp 8.
- Ertürk Düzgün, Nihal. *Particle image velocimetry applications in complex flow systems*. Doctoral thesis. Universitat Rovira i Virgili, Departament d'Enginyeria Mecànica. 2012.
- Ertürk, N.; Düzgun, A.; Ferrè, J.; Vareal, S. and Vernet, A. (2013). *Alginate flow seeding microparticles for use in Particle Image Velocimetry (PIV)*. 10th International Symposium on Particle Image Velocimetry – PIV13. Delft, The Netherlands, July 1-3, 2013
- Fabiani, M.; Mancò, S.; Nervegna, N.; Rundo, M. (1999). *Modelling and Simulation of Gerotor Gearing in Lubricating Oil Pumps*. Society of Automotive Engineers. International Congress and Exposition, pp 15.
- Gamez-Montero, P. J., and Codina, E. (2003). *Contact Stress in a Gerotor Pump*, ASME International Mechanical Engineering Congress and Exposition, November 15–21, Washington, DC, pp. 65–71.
- Gamez-Montero, P. J., Garcia-Vilchez, M., Raush, G., Freire, J., and Codina, E., 2012, *Teeth Clearance and Relief Grooves Effects in a Trochoidal-Gear Pump Using New Modules of GeroLAB*, Trans. ASME J. Mech. Des., 134(5), p. 054502.
- Gamez-Montero, PJ. and Codina, E (2007), *Flow Characteristics of a Trochoidal-Gear Pump Using Bond Graphs and Experimental Measurement—Part 1*, Proc. Inst. Mech. Eng. Part I: J. Systems and Control Engineering, Vol. 221, pp. 331-346
- Gamez-Montero, PJ. and Codina, E (2007), *Flow Characteristics of a Trochoidal-Gear Pump Using Bond Graphs and Experimental Measurement—Part 2*, Proc. Inst. Mech. Eng. Part I: J. Systems and Control Engineering, Vol. 221, pp. 347-363
- Gamez-Montero, PJ., Castilla, R., Del Campo, D., Ertürk, N. and Codina, E. (2011). *Influence of the interteeth clearances on the flow ripple in a gerotor pump for engine lubrication*. Proc. Inst. Mech. Eng. Part D: J. of Automobile Engineering 0(0) 1-13
- Gamez-Montero, PJ., Castilla, R., Khamashta, M. and Codina, E (2006), *Contact Problems of a Trochoidal-Gear*

Pump, International Journal of Mechanical Sciences, Vol. 48, pp. 1471-1480

Gamez-Montero, PJ., Castilla, R., Mujal, R., Khamashta, M. and Codina, E. (2009), *GEROLAB Package System: Innovative Tool to Design a Trochoidal-Gear Pump*, Journal of Mechanical Design, Vol. 131, pp. 074502-1-074502-6

Gi-Woo Kim, Jae-In Park and Jae-Duk Jang (2000). *Performance Development for Hydraulic Elements of Hyundai Automotive Automatic Transmission*. Seoul 2000 FISITA World Automotive Congress , June 12-15, F2000A077.

Heisler A, Moskwa J and Fronczak F 2009 The Design of Low-Inertia, High-Speed External Gear Pump/Motors for Hydrostatic Dynamometer Systems SAE Technical Paper 2009-01- 1117.

Hsieh, Chiu-Fan (2009). *Influence of gerotor performance in varied geometrical design parameters*. Journal of Mechanical Design Vol. 131, MD-09-1037

Hsieh, Chiu-Fan (2011). *Fluid and Dynamics Analyses of a Gerotor Pump Using Various Span Angle Designs*. Journal of Mechanical Design Vol. 134

Hwang, Yii-Wen; Hsieh, Chiu-Fan (2006). *Geometric Design Using Hypotrochoid and Nonundercutting Conditions for an Internal Cycloidal Gear*. Journal of Mechanical Design Vol. 129 (2006), 413-420.

Itoh, T., Murai, Y., Ueno, Y., Oiwa, H., Miyagi, N. and Yamamoto, F. (2005). *Visualization of Internal Flow in an Inscribed Trochoid Gear Pump*. Journal of the Visualization Society of Japan; ISSN:0916-4731; VOL.25; PAGE.303-304; (2005)

Iudicello, F. (2002). *CFD modeling and design optimization of a gerotor pump*. Bath International Workshop on Power Transmission and Motion Control.

Iudicello, F. and Mitchell, D. (2002). CFD modeling of the flow in a gerotor pump. Bath International Workshop on Power Transmission and Motion Control.

Ivanovic, L; JOSIFOVIC, D.; Ilic, A. and Stojanovic, B. (2013). *Analytical model of the pressure variation in the gerotor pump chambers*. Technics Technologies Education Management. Vol.8 Num.1

Ivanovic, L., Devedzic, G., Miric, N. and Cukovic, S. (2010). *Analysis of forces and moments in the gerotor pumps*. Proceedings of the Institution of Mechanical Engineers, Part C, Journal of Mechanical Engineering Science, Volume 224, Number 10 / 2010.

Jiang Y and Perng C 1997 An Efficient 3D Transient Computational Model for Vane Oil Pump and Gerotor Oil Pump Simulations SAE Technical Paper 970841

Jiang Y, Furmanczyk M, Lowry S and Zhang D et al. 2008 A Three-Dimensional Design Tool for Crescent Oil Pumps SAE Technical Paper 2008-01-0003

Johnston, D.N.; Edge, K.A. (1991) *A Test Method for Measurement of Pump Fluid-Borne Noise Characteristics*. SAE 911761, pp. 10.

Johnston, D.N.; Edge, K.A. (1991) *In-situ Measurement of the Wavespeed and Bulk Modulus in Hydraulic Lines*. Institution of Mechanical Engineers, pp. 12.

Johnston, D.N.; Edge, K.A. (1996). *Measurement of Positive Displacement Pump Flow Ripple and Impedance*. Institution of Mechanical Engineers, pp. 9.

Karamooy Ravari, M.R. (2011). *Elliptical lobe shape gerotor pump design to minimize wear*. Front. Mech. Eng. 2011, 6(4): 429–434. DOI 10.1007/s11465-011-0247-6

- Karamooz Ravari, M.R. Forouzan, M.R. and Moosavi, H. (2010). *Flow irregularity and wear optimization in epitrochoidal gerotor pumps*. Meccanica (2012) 47:917-928.
- Kim J. H., Kim C., Chang Y. J. *Optimum design on lobe shapes of gerotor oil pump*. Journal of Mechanical Science and Technology, 2006; 20, 5 : p. 1390-1398.
- Kini S, Mapara N, Thoms R and Chang P 2005 Numerical Simulation of Cover Plate Deflection in the Gerotor Pump SAE Technical Paper 2005-01-1917
- Kojima, E. (1) *A New Method for Experimental Determination of Pumps Fluid Borne Noise Characteristics*. Circuit, Component and System Design. Edited by Burrows&Edge. Fifth Bath Int. Fluid Power Workshop. ISBN 0-96380-139-0.
- Launder B E and Spalding D B 1974 Comput. Methods Appl. Mech. Eng. 3 269-289
- Litvin, F. (1994) *Gear Geometry and Applied Theory*. Prentice may, Inc.
- Maiti R. (1993). *Distributor valve port sequences in epitrochoid rotary piston machines type hydrostatic units*. Archive of Applied Mechanics, 1992; p. 223-229.
- Maiti R., Sinha G.L. (1998). *Kinematics of active contact in modified epitrochoid generated rotary piston machines*. Mechanism and Machine Theory, 1988; 23: 39-45.
- Maiti, R. (1993) *Active Contact Problems in Epitrochoid Generated 'Floating Axis' Orbital Rotary Piston Machines*. Journal of Engineering for Industry, Transactions of the ASME, Vol. 115, pp 337-340.
- Maiti, R. (1993). *Torque Characteristics of Epitrochoid Generated Orbital Rotary Piston Type Hydraulic Motors*. Mechanism Machine Theory, Vol. 28, pp 225-231.
- Maiti, R., SinhaG.L. (1990). *Limits on modification of epitrochoid used in rotary piston machines and the effects of modification on geometric volume displacement and ripple*. Ingenieur-Archiv, 1990; 60: 183-194.
- Mancò, G.; Mancò, S.; Rundo, M.; Nervegna, N. (2000). *Computerized Generation of Novel Gearings for Internal Combustion Engines Lubricating Pumps*. International Journal of Fluid Power, pp 10.
- Mancò, G.; Nervegna, N.; Rundo, M. (2002). *A Contribution of the Design of Hydraulic Lobe Pumps*. International Journal of Fluid Power, pp 10.
- Mancò, S.; Nervegna, N.; Rundo, M.; Armenio, G. (1998). *Gerotor Lubricating Oil Pump for IC Engines*. SAE Technical Paper Series International Fall Fuels and Lubricants Meeting and Exposition. 1998. pp 20.
- Meincke O and Rahmfeld R 2008 6th Int. Fluid Power Conf. (Dresden, 1-2 April 2008) 485-99
- Mimmi G.; Pennacchi P. (2000). *Non-undercutting conditions in internal gears*. Mechanism and Machine Theory, 2000; 35: 477-490.
- Mimmi, G.; Pennacchi, P. (1997). *Rotor Design and Optimization in Internal Lobe Pumps*. Applied Mechanics Reviews, pp 9.
- Mimmi, G.; Pennacchi, P.; Savi, C. (1996). *Internal Lobe Pump Design*. Proc. Mechanics in Design CSME Forum 1996, pp 9.
- Mucchi, E; Dalpiazza, G. and Fernandez del Rincon, A. (2010). *Elastodynamic analysis of a gear pump. Part I: Pressure distribution and gear eccentricity*. Mechanical Systems and Signal Processing 24 (2010) 2160–2179
- Natchimuthu K, Sureshkumar J and Ganesan V 2010 CFD Analysis of Flow through a Gerotor Oil Pump SAE Technical Paper 2010-01-1111

- Paffoni B. Pressure and film thickness in a trochoidal hydrostatic gear pump, Proc. IMechE Part G: Proceedings of the Institution of Mechanical Engineers - Part G: Journal of Aerospace Engineering, 2003; 217(4): 179-187.
- Raffel, M.; Willert, C; Wereley, S and Kompenhans, J. *Particle Image Velocimetry_A Practical Guide*. Springer, 2007. ISBN 978-3-540-72307-3
- Rasband, W.S., ImageJ, U. S. National Institutes of Health, Bethesda, Maryland, USA, <http://imagej.nih.gov/ij/>, 1997-2012.
- Robinson, F.J.; Lyon, J.R. (1976). *An Analysis of Epitrochoidal Profiles with Constant Difference Modification Suitable for Rotary Expanders and Pumps*. Journal of Engineering for Industry ASME Transactions, pp 5.
- Ruvalcaba, M.A. and Hu, X. (2011). *Gerotor fuel pump performance and leakage study*. Proceeding of the ASME 2011 International Mechanical Engineering Congress & Exposition IMECE2011-62226.
- Saegusa, Y.; Urashima, K. (1984). *Development of Oil-Pumps Rotors with a Trochoidal Tooth Shape*. Sumitomo Electric Technical Review, pp 5.
- Sang-Yeol Kim, Yung-Joo Nam and Myeong-Kwan Park (2006). *Design of port plate in gerotor pump for reduction of pressure pulsation*. Journal of Mechanical Science and Technology (KSME Int. J.). Vol. 20, No. 10, pp. 1626-1637, 2006.
- Scilab Enterprises (2012). Scilab: Free and Open Source software for numerical computation (OS, Version 5.4.1) [Software]. Available from: <http://www.scilab.org>
- Shung, J.B.; Pennock, G.R. (1994). *Geometry for Trochoidal Type Machines with Conjugate Envelopes*. Mechanism Machine Theory, Vol. 29, pp 17.
- Singhal A K, Athavale M M, Li H Y and Jiang Y 2002 J. Fluids Eng. – Trans ASME 124(3) 617-624.
- Stryczek, J. (1990). *Cycloidal Gears in Design of Gear Pumps and Motors*. Archiwum Budowy Maszyn, 36, pp 30.
- Stryczek, J. (1990). *Principles of the Design for Cycloidal Gears in Hydraulic Machinery*. Archiwum Budowy Maszyn, 37, pp 19.
- Stryczek, J. (1996). *Hydraulic Machines with Cycloidal Gearing*. Archiwum Budowy Maszyn, 43, pp 43.
- Suresh Kumar, M. and Manonmani, K. (2010). *Computational fluid dynamics integrated development of gerotor pump inlet components for engine lubrication 2010*. Proc. IMech.E Vol. 224 Part D: J. Automobile Engineering, pp. 1555-1567
- Van der Graaf, G. (2004). *Gpiv: An open Source project for PIV*. Presentation at PIVNET/ERCOFTAC workshop, July 2004, Lisbon, Portugal.
- Vecchiato D., Demenego A., Argyris J., Litvin F.L. *Geometry of a cycloidal pump, Computer methods in applied mechanics and engineering*, 2001; 190 : 2309-2330.
- Versteeg, H.K. and Malalasekera, W. *An Introduction to Computational Fluid Dynamics. The Finite Volume Method*. 2nd Edition. Pearson Education Limited, 2007. ISBN: 978-0-13-127498-3
- Wang D, Ding H, Jiang Y and Xiang X (2012). *Numerical Modeling of Vane Oil Pump with Variable Displacement*. SAE Technical Paper 2012-01-0637.

Yan, J., Yang, D.C.H. and Tong, S.H. (2009). *A New Gerotor Design Method With Switch Angle Assignability*. Journal of Mechanical Design. Vol. 131. DOI: 10.1115/1.3013442

Yang, D.C.H., Yan, J. and Tong, S.H. (2010). *Flowrate Formulation of Deviation Function Based Gerotor Pumps*. Journal of Mechanical Design. Vol. 132. DOI: 10.1115/1.4001595

Ye, Z. (2005). *Simple explicit formulae for calculating limit dimensions to avoid undercutting in the rotor of a cycloid rotor pump*. Mechanism and machine theory, ISSN 0094-114X, Vol. 41, Nº 4, 2006 , pp. 405-414

Zhang D, Perng C and Laverty M (2006). *Gerotor Oil Pump Performance and Flow/Pressure Ripple Study*. SAE Technical Paper 2006-01-0359